

## Abstract

### Electrons on the Move in Proteins: Microbial Cytochrome Nanowires in Extracellular Electron Transfer and as Functional Materials

Catharine Shippy

2022

Proteins are commonly known to transfer electrons over distances limited to a few nanometers. However, many biological processes require electron transport over far longer distances. For example, some soil and sediment bacteria transport electrons over hundreds of micrometers to even centimeters. In particular, *Geobacter sulfurreducens* uses extracellular electron transfer (EET) to move respiratory electrons from the cytoplasm to external electron acceptors such as minerals or external electrodes in biofilm growth. These terminal acceptors are mere microns to as far as thousands of times the length of a cell away in biofilms. The exact mechanisms for the EET pathway and the long-range charge transport remain unclear. Cytochromes OmcS and OmcZ have been found to be of critical importance to *G. sulfurreducens* respiration over the years. It is known that OmcS is important for growth on minerals, and that OmcZ is critical for high current production during growth on electrodes. Recently, the discovery that both proteins form micrometer long nanowires *in vivo* has prompted an investigation into how each nanowire contributes to cellular metabolic processes, in contrast to previous studies focused on monomers. Understanding the electrochemical and electronic properties of microbial nanowires will help to elucidate their role in EET. Furthermore, light-induced microbial electron transfer has potential for efficient production of value-added chemicals, biofuels, and biodegradable materials owing to diversified metabolic

pathways. Thus, both nanowires and biofilms should be investigated as biocompatible photoconductive materials for efficient electronic interface between microbes and electrodes.

To achieve better understanding of long-range charge transport in proteins I used individual amyloid protein crystals with atomic-resolution structures as a model system. I perform contact-free measurements of intrinsic electronic conductivity using a 4-electrode approach. I find hole transport through micrometer-long stacked tyrosines at physiologically relevant potentials. Notably, the transport rate through tyrosines ( $10^5 \text{ s}^{-1}$ ) is comparable to cytochromes. Combined experimental and computational studies reveal that proton-coupled electron transfer confers conductivity through energetics of the proton acceptor, a neighboring glutamine.

To understand the role of both nanowires in EET by *G. sulfurreducens* I used electrochemical studies to remeasure their redox potentials as nanowires. I find through spectroelectrochemistry that the macroscopic midpoint potential of the OmcS nanowire is physiologically relevant at  $-0.130 \text{ V}$  vs SHE, and it has a wide active redox range. The resulting redox landscape across a subunit of the nanowire follows an overall nearly thermoneutral pattern, consistent with the need to conserve energy for micrometer long electron transport. These results help to revise OmcS's role in EET as a protein that can favorably accept electrons from the periplasm and transport them to minerals in the soils.

I find that OmcZ nanowires have three redox peaks that range from  $-70$  to  $-281 \text{ mV}$  which indicates unique heme grouping in OmcZ. I investigate how differential expression of nanowires over time affects biofilm conductivity and redox potential in strains of wild type,  $\Delta omcS$ , and  $\Delta omcZ$ . I find that OmcZ abundance is correlated with an increase in

metabolic current and conductance of biofilms. I find that electrochemical gating of wild type and  $\Delta omcS$  matches the gating of OmcZ nanowires very well and find that OmcZ has greater than 400-fold gate effect compared to OmcS. Finally, I show that living biofilms of *Geobacter sulfurreducens* use nanowires of cytochrome OmcS as intrinsic photoconductors. Photoconductive atomic force microscopy shows >10-fold increase in photocurrent in purified individual nanowires. Photocurrents respond rapidly (<100 ms) to the excitation and persist reversibly for hours. Femtosecond transient absorption spectroscopy and quantum dynamics simulations reveal ultrafast (~200 fs) electron transfer between nanowire hemes upon photoexcitation, enhancing carrier density and mobility. Our work reveals a new class of natural photoconductors for whole-cell catalysis.

Electrons on the Move in Proteins: Microbial Cytochrome Nanowires in Extracellular  
Electron Transfer and as Functional Materials

A Dissertation  
Presented to the Faculty of the Graduate School  
Of  
Yale University  
In Candidacy for the Degree of  
Doctor of Philosophy

By  
Catharine Shipps

Dissertation Director: Nikhil S. Malvankar

December 2022

Copyright © 2022 by Catharine Shipps

All rights reserved.

# Table of Contents

|   |             |
|---|-------------|
| <b>ABSTRACT</b> .....   | <b>I</b>    |
| <b>TABLE OF CONTENTS</b> .....  | <b>IV</b>   |
| <b>ACKNOWLEDGEMENTS</b> .....   | <b>VII</b>  |
| <b>ABBREVIATIONS</b> .....  | <b>VIII</b> |
| <b>FIGURES AND TABLES</b> .....   | <b>X</b>    |
| MAIN FIGURES .....  | X           |
| SUPPLEMENTAL FIGURES .....  | X           |
| MAIN TABLES .....   | XI          |
| SUPPLEMENTAL TABLES .....   | XI          |
| <b>1. INTRODUCTION</b> .....  | <b>1</b>    |
| 1.1 OVERVIEW .....  | 5           |
| <b>2. USING PEPTIDE CRYSTALS WITH STACKED TYROSINES AS MODEL SYSTEM</b> .....   | <b>6</b>    |
| 2.1 AUTHOR CONTRIBUTIONS .....  | 6           |
| 2.2 SUMMARY .....   | 6           |
| 2.3 SIGNIFICANCE STATEMENT .....  | 7           |
| 2.4 INTRODUCTION .....  | 8           |
| 2.5 RESULTS .....   | 11          |
| 2.5.1 <i>STRATEGY TO MEASURE CONTACT-FREE ELECTRON TRANSPORT IN PROTEINS TO DETERMINE INTRINSIC CONDUCTIVITY</i> .....                      | 11          |
| 2.5.2 <i>MICROMETER-LONG CHAINS OF STACKED TYROSINES CONFER CONDUCTIVITY TO AMYLOIDS</i> .....  | 13          |
| 2.5.3 <i>INCREASED STRUCTURAL RIGIDITY OF AMYLOIDS DUE TO METAL IONS ENHANCES CONDUCTIVITY</i> .....  | 17          |
| 2.5.4 <i>DFT SUGGESTS HOLE CONDUCTIVITY DUE TO PROTON ROCKING AND THE ENERGETICS OF PROTON ACCEPTOR DETERMINES THE TRANSPORT RATE</i> ..... | 20          |
| 2.5.5 <i>STACKING SUBSTANTIALLY LOWERS THE REDOX POTENTIAL OF TYROSINE</i> .....  | 22          |
| 2.5.6 <i>RESISTANCE INCREASES LINEARLY WITH PROTEIN LENGTH SUGGESTING A HOPPING MECHANISM</i> .....   | 23          |
| 2.5.7 <i>HIGHER AVAILABILITY OF THE PROTON ACCEPTOR LEADS TO A 200-FOLD INCREASE IN AMYLOID CONDUCTIVITY</i> .....                          | 24          |
| 2.6 DISCUSSION .....  | 28          |
| 2.7 MATERIALS AND METHODS .....   | 30          |
| 2.7.1 <i>PREPARATION OF PEPTIDE MICROCRYSTALS</i> .....   | 30          |
| 2.7.2 <i>SAMPLE PREPARATION FOR CONDUCTIVITY MEASUREMENTS</i> .....   | 30          |
| 2.7.3 <i>DIRECT CURRENT (DC) CONDUCTIVITY MEASUREMENTS</i> .....  | 31          |
| 2.7.4 <i>IMPEDANCE SPECTROSCOPY (IS)</i> .....  | 32          |
| 2.7.5 <i>TEMPERATURE DEPENDENT DC CONDUCTIVITY MEASUREMENTS</i> .....   | 32          |
| 2.7.6 <i>CONDUCTIVITY CALCULATIONS</i> .....  | 32          |
| 2.7.7 <i>ACKNOWLEDGMENTS</i> .....  | 33          |
| 2.8 SUPPLEMENTARY INFORMATION .....   | 34          |
| <b>3. OMCS AS A PHYSIOLOGICAL NANOWIRE</b> .....  | <b>35</b>   |

|           |  |           |
|-----------|--|-----------|
| 3.1       | AUTHOR CONTRIBUTIONS.....  | 35        |
| 3.2       | SUMMARY.....   | 35        |
| 3.3       | INTRODUCTION .....   | 36        |
| 3.4       | RESULTS .....  | 39        |
| 3.4.1.    | <i>REDOX CHARACTERIZATION OF OMCS NANOWIRES REVEALS MORE POSITIVE MIDPOINT POTENTIAL .....</i> | 39        |
| 3.4.2.    | <i>MACROSCOPIC REDUCTION POTENTIALS .....</i>  | 40        |
| 3.4.3.    | <i>SURFACE POTENTIALS OF OMCS AND PPCA ARE COMPATIBLE .....</i>                                | 43        |
| 3.5       | DISCUSSION .....   | 43        |
| 3.5.1.    | <i>PROPOSED MODEL FOR PERIPLASMIC ELECTRON TRANSFER TO OMCS .....</i>                          | 43        |
| 3.6       | MATERIALS & METHODS.....   | 44        |
| 3.6.1.    | <i>PURIFICATION OF OMCS.....</i>   | 44        |
| 3.6.2.    | <i>TEM IMAGING .....</i>   | 44        |
| 3.6.3.    | <i>ELECTROSTATIC POTENTIAL VISUALIZATION .....</i>   | 45        |
| 3.6.4.    | <i>ELECTROCHEMISTRY.....</i>   | 45        |
| 3.6.5.    | <i>SPECTROELECTROCHEMISTRY.....</i>  | 46        |
| 3.7       | SUPPLEMENT .....   | 48        |
| <b>4.</b> | <b>NANOWIRES IN MUTANT BIOFILMS: A LOOK AT WHAT OMCS AND OMCZ DO FOR EET .....</b>             | <b>49</b> |
| 4.1       | AUTHOR CONTRIBUTIONS.....  | 49        |
| 4.2       | SUMMARY.....   | 49        |
| 4.3       | INTRODUCTION .....   | 50        |
| 4.4       | RESULTS .....  | 51        |
| 4.4.1.    | <i>EXTRACELLULAR OMCZ NANOWIRES STIMULATE BIOFILM METABOLIC CURRENT AND CONDUCTIVITY .....</i> | 53        |
| 4.4.2.    | <i>OMCZ SHOWS BROAD REDOX RANGE SIMILAR TO <math>\Delta</math>OMCS BIOFILMS .....</i>          | 56        |
| 4.4.3.    | <i>ELECTROCHEMICAL GATING ON BIOFILMS SHOWS OVERLAP WITH OMCZ.....</i>                         | 57        |
| 4.5       | DISCUSSION .....   | 59        |
| 4.6       | METHODS .....  | 62        |
| 4.6.1.    | <i>DEVICE FABRICATION AND PREPARATION.....</i>   | 62        |
| 4.6.2.    | <i>BACTERIAL STRAINS AND GROWTH CONDITIONS .....</i>   | 62        |
| 4.6.3.    | <i>BIOFILM GROWTH.....</i>   | 63        |
| 4.6.4.    | <i>FILAMENT PREPARATIONS.....</i>  | 64        |
| 4.6.5.    | <i>PROTEIN NORMALIZATION &amp; GELS.....</i>   | 64        |
| 4.6.6.    | <i>ELECTROCHEMISTRY.....</i>   | 65        |
| 4.6.7.    | <i>CONDUCTANCE MEASUREMENTS.....</i>   | 66        |
| 4.6.8.    | <i>DATA ANALYSIS.....</i>  | 66        |
| 4.6.9.    | <i>ELECTROSTATIC POTENTIAL VISUALIZATION .....</i>   | 66        |
| 4.7       | SUPPLEMENT .....   | 66        |
| <b>5.</b> | <b>LIVING PHOTOCONDUCTORS .....</b>  | <b>68</b> |
| 5.1       | AUTHOR CONTRIBUTIONS.....  | 68        |
| 5.2       | SUMMARY.....   | 68        |
| 5.3       | INTRODUCTION .....   | 69        |

|           |  |            |
|-----------|--|------------|
| 5.4       | RESULTS .....  | 73         |
| 5.4.1.    | <i>PHOTOCONDUCTIVITY IN LIVING BIOFILMS MADE UP OF OMCS NANOWIRE NETWORK</i> ..... | 73         |
| 5.4.2.    | <i>RAPID PHOTOCONDUCTIVITY IN PURIFIED NANOWIRES REVERSIBLE FOR HOURS</i> .....    | 73         |
| 5.4.3.    | <i>INDIVIDUAL NANOWIRES SHOW UP TO 100-FOLD PHOTOCONDUCTIVITY INCREASE</i> .....   | 75         |
| 5.4.4.    | <i>FS-TA REVELS SUB-PICOSECOND CHARGE SEPARATION IN NANOWIRE</i> .....             | 76         |
| 5.4.5.    | <i>COMPUTATIONS SUGGEST EXCITED STATE ELECTRON TRANSFER BETWEEN HEMES</i> .....    | 79         |
| 5.5       | DISCUSSION .....   | 80         |
| 5.5.1.    | <i>HEMES ARE LIKELY ELECTRON SOURCE FOR OBSERVED PHOTOREDUCTION</i> .....          | 80         |
| 5.5.2.    | <i>PROPOSED MECHANISM FOR ULTRAFAST PHOTOCONDUCTIVITY IN OMCS NANOWIRE</i> .....   | 83         |
| 5.6       | METHODS .....  | 86         |
| 5.6.1.    | <i>BACTERIAL BIOFILM GROWTH AND OMCS NANOWIRE PURIFICATION</i> .....               | 86         |
| 5.6.2.    | <i>UV-VIS SPECTROSCOPY</i> .....   | 87         |
| 5.6.3.    | <i>ELECTRODE FABRICATION</i> .....   | 88         |
| 5.6.4.    | <i>DC CONDUCTANCE OF BIOFILMS AND NANOWIRES</i> .....                              | 89         |
| 5.6.5.    | <i>TRANSIENT ABSORPTION (TA) DATA COLLECTION</i> .....                             | 90         |
| 5.6.6.    | <i>TRANSIENT ABSORPTION (TA) DATA PROCESSING</i> .....                             | 91         |
| 5.6.7.    | <i>PHOTOCONDUCTIVE AFM (PC-AFM)</i> .....  | 93         |
| 5.6.8.    | <i>LASER CHARACTERIZATION</i> .....  | 95         |
| 5.6.9.    | <i>COMPUTATIONAL METHODS</i> .....   | 96         |
| 5.7       | SUPPLEMENT .....   | 99         |
| <b>6.</b> | <b>CONCLUSIONS AND FUTURE DIRECTIONS .....</b>                                     | <b>106</b> |
|           | <b>REFERENCES .....</b>  | <b>108</b> |

## **Acknowledgements**

I would like to thank my advisor Nikhil Malvankar for his support and academic insight while we tackled challenging, novel problems in the field. Additionally, I extend great thanks to my thesis committee members Jonathon (Joe) Howard, Gary Brudvig, and Victor Batista for their invaluable feedback on each new research direction. This work could not have been completed without the generous support from the National Defense Science and Engineering Graduate Fellowship program which funded my research.

I am grateful for my lab mates who made this challenging, extremely collaborative work not only possible but enjoyable. I learned a great deal from each of them and developed some great friendships along the way. Thanks should also go to my cohort for their consistent moral support and camaraderie.

Lastly, I want to thank my family especially my parents, siblings, and my partner. They have all had unwavering support for me through this journey and inspire me to take on new challenges with high spirits and fierce dedication.

## Abbreviations

|                |   |
|----------------|---|
| <b>AFM</b>     | atomic force microscopy                           |
| <b>Cryo-EM</b> | cryo-electron microscopy                          |
| <b>CV</b>      | cyclic voltammetry                                |
| <b>DPV</b>     | differential pulse voltammetry                    |
| <b>EET</b>     | extracellular electron transfer                   |
| <b>ET</b>      | electron transfer                                 |
| <b>ETp</b>     | electron transport                                |
| <b>fs-TA</b>   | ultrafast transient absorption spectroscopy       |
| <b>FTO</b>     | fluorine doped tin oxide                          |
| <b>G.s.</b>    | <i>Geobacter sulfurreducens</i> strain unspecific |
| <b>I-V</b>     | current voltage                                   |
| <b>NMR</b>     | nuclear magnetic resonance                        |
| <b>pc-AFM</b>  | photoconductive atomic force microscopy           |
| <b>QM/MD</b>   | quantum mechanical molecular dynamics             |
| <b>SEC</b>     | spectroelectrochemistry                           |
| <b>SHE</b>     | standard hydrogen electrode                       |
| <b>TEM</b>     | transmission electron microscopy                  |
| <b>UV-Vis</b>  | ultraviolet visible spectroscopy                  |
| <b>WT</b>      | wild type   |
| <b>X1</b>      | Zn <sup>2+</sup> NNQQNY peptide crystal           |
| <b>X2</b>      | GNNQQNY peptide crystal                           |
| <b>X3</b>      | Zn <sup>2+</sup> GGVLVN peptide crystal           |

**X4** KVQIINKKL peptide crystal  
**PCET** proton coupled electron transfer

# Figures and Tables

## Main Figures

|  |    |
|--|----|
| FIGURE 1.1: STRUCTURAL DIFFERENCES IN IMPORTANT MICROBIAL NANOWIRES REVEALED BY CRYO-EM.....   | 2  |
| FIGURE 2.1: STRATEGY TO EVALUATE PROTEIN CONDUCTIVITY MECHANISM USING SHORT PEPTIDES AS BUILDING BLOCKS FOR MODEL SYSTEMS. ....                              | 10 |
| FIGURE 2.2: INTRINSIC CONDUCTIVITY MEASUREMENTS OF AMYLOIDS REVEAL MICROMETER-LONG CHARGE TRANSPORT THROUGH STACKED TYROSINES. ....                          | 12 |
| FIGURE 2.3: IMPEDANCE SPECTROSCOPY CONFIRMS PURELY ELECTRONIC CONDUCTIVITY IN AMYLOIDS. ....   | 17 |
| FIGURE 2.4: TYROSINE STACKING AND PROTON ACCEPTOR AVAILABILITY GOVERN CONDUCTIVITY. ....   | 19 |
| FIGURE 2.5: DFT CALCULATIONS CONFIRM PROTON TRANSFER IN OXIDIZED XI. ....  | 20 |
| FIGURE 2.6: RESISTANCE INCREASES LINEARLY WITH CRYSTAL LENGTH, CONSISTENT WITH A HOPPING MECHANISM.....  | 23 |
| FIGURE 2.7: EXPONENTIALLY-INCREASING CRYSTAL CONDUCTIVITY UPON COOLING NEAR PHYSIOLOGICAL TEMPERATURES DUE TO INCREASED AVAILABILITY OF PROTON ACCEPTOR..... | 25 |
| FIGURE 3.1: STRATEGY TO DETERMINE ROLE OF OMCs IN EET .....  | 38 |
| FIGURE 3.2: OMCs HAS MORE POSITIVE REDOX POTENTIALS THAN PREVIOUSLY REPORTED. ....   | 40 |
| FIGURE 3.3: COMPUTATIONAL CALCULATIONS OF HEME REDOX POTENTIAL AGREE WITH EXPERIMENTAL MICROSCOPIC POTENTIALS. ....  | 41 |
| FIGURE 3.4:REVISED MODEL OF EXTRACELLULAR ELECTRON TRANSFER WITH OMCs.....   | 42 |
| FIGURE 4.1: STRATEGY TO INVESTIGATE NANOWIRE EXPRESSION AND CONDUCTIVITY, REDOX PROFILE SIMULTANEOUSLY. ....   | 52 |
| FIGURE 4.2: NANOWIRE-DEFICIENT MUTANTS HAVE MORE PROTEIN IN FILAMENT PREPARATIONS OVER TIME. ....  | 53 |
| FIGURE 4.3: CONDUCTANCE INCREASES WITH OMCz PRODUCTION IN BIOFILMS. ....   | 55 |
| FIGURE 4.4: OMCz NANOWIRES SHOW MULTIPLE REDOX CENTERS THAT OVERLAP WITH BIOFILM SIGNATURES. ....  | 56 |
| FIGURE 4.5: ELECTROCHEMICAL GATING SHOWS OVERLAP BETWEEN BIOFILM AND OMCz RESPONSE. ....   | 58 |
| FIGURE 4.6: ELECTROSTATIC POTENTIALS FAVOR INTERACTION BETWEEN PpCA AND OMCz. ....   | 60 |
| FIGURE 5.1: LIVING PHOTOCONDUCTORS. ....   | 73 |
| FIGURE 5.2: HIGH PHOTOCONDUCTIVITY IN PURIFIED PROTEIN NANOWIRES. ....   | 74 |
| FIGURE 5.3: ULTRAFAST (<100 FS) CHARGE TRANSFER BETWEEN HEMES IN NANOWIRES REVEALED BY FEMTOSECOND TRANSIENT ABSORPTION SPECTROSCOPY (FS-TA). ....           | 77 |
| FIGURE 5.4: MODEL FOR ORIGIN OF PHOTOCONDUCTIVITY IN PROTEIN NANOWIRES. ....   | 81 |

## Supplemental Figures

|  |     |
|--|-----|
| SI FIGURE 3.1: OMCs AND MEDIATOR INTERFERENCE IS CONCENTRATION DEPENDENT. ....   | 48  |
| SI FIGURE 4.1: ATYPICAL GROWTH ON $\Delta$ OMCS FINAL TIMEPOINT.....   | 66  |
| SI FIGURE 4.2: ADDITIONAL GEL IMAGES ON FILAMENT PREPARATIONS. ....  | 67  |
| SI FIGURE 5.1: NANOWIRES ARE OXIDIZED IN AIR AND CHEMICALLY REDUCED NANOWIRES DO NOT SHOW SIGNIFICANT PHOTOCONDUCTIVITY. ....              | 99  |
| SI FIGURE 5.2: NANOWIRES SHOW PHOTOCONDUCTIVITY IRRESPECTIVE OF ELECTRODE MATERIALS. ....  | 99  |
| SI FIGURE 5.3: NANOWIRE CONDUCTANCE INCREASE UPON LASER ON/OFF INCREASES WITH LASER POWER. ....  | 100 |
| SI FIGURE 5.4: ULTRAFAST (<100 FS) CHARGE TRANSFER BETWEEN HEMES IN NANOWIRES REVEALED BY FS-TA WITH A PUMP BEAM AT $\lambda=530$ NM. .... | 100 |
| SI FIGURE 5.5: ULTRAFAST (<100 FS) CHARGE TRANSFER BETWEEN HEMES IN NANOWIRES REVEALED BY FS-TA WITH A PUMP BEAM ( $\lambda=400$ NM). .... | 101 |
| SI FIGURE 5.6: LACK OF CHARGE TRANSFER WITHOUT NANOWIRES. ....   | 101 |
| SI FIGURE 5.7: SOLID STATE AND LIQUID MEASUREMENTS GIVE SIMILAR DYNAMICS. ....   | 102 |
| SI FIGURE 5.8: TRANSIENT ABSORPTION DYNAMICS NOT DEPENDENT ON LASER POWER. ....  | 102 |

|   |     |
|---|-----|
| SI FIGURE 5.9: ELECTRON SURVIVAL PROBABILITY .....                        | 103 |
| SI FIGURE 5.10: ATOMIC SPIN POPULATIONS FOR DOUBLY OXIDIZED SPECIES. .... | 103 |
| SI FIGURE 5.11: LASER ALIGNMENT FOR PC-AFM.....                           | 105 |

**Main Tables**

|  |    |
|--|----|
| TABLE 3.1: MACROSCOPIC POTENTIAL COMPARISON BETWEEN EXPERIMENTS AND COMPUTATIONS ..... | 41 |
|--|----|

**Supplemental Tables**

|  |     |
|--|-----|
| SI TABLE 5.7.1: SPIN DENSITIES .....                     | 104 |
| SI TABLE 5.7.2: CP-AFM NANOWIRE CONDUCTANCE VALUES. .... | 104 |

## 1. Introduction

The movement of electrons through natural materials is one of the most vital processes in living systems. For example, it underpins photosynthesis, respiration, and DNA biosynthesis<sup>1,2</sup>. The most fundamental phenomenon is electron transfer (ET) or the process of an electron moving from one molecule to another due to a difference in energy, usually on the nanometer scale<sup>1,3</sup>. For example, ET between cytochrome c oxidase and oxygen helps power ATP production in cells<sup>1</sup>. Alternatively, electron transport (ETp) is when current passes through a material due to an externally applied voltage, either manual or physiological, without the presence of electrolyte<sup>4</sup>. This is easiest to think of in terms of wires that transport electricity from the power outlet to a cherished appliance, say, a toaster. But ETp can also be a physiologically important process used by some species of soil bacteria to complete cellular respiration and it can occur on the nanometer, micrometer, and even centimeter scale<sup>5</sup>. These bacteria primarily use ETp to get around barriers like mineral distribution and metabolic constraints<sup>5,6</sup>. One of these common soil bacteria, *Geobacter sulfurreducens*, is the focus of this study for its ability to perform ETp with novel machinery that has set a new precedent for understanding ETp through proteins.

Dissimilatory Fe(III) oxide reduction by microbes is one of the most important biogeochemical processes for the cycling of carbons and nutrients and bioremediation of organic and metal contaminants in the groundwater<sup>7</sup>. In many subsurface sediments with abundant Fe(III) oxide, *Geobacter* is the predominant species<sup>8,9</sup>. It was proposed that the enrichment of *Geobacter* over other metal reducing bacteria was due to its method of direct electron transfer and ability to produce appendages in response to Fe(III) oxide in

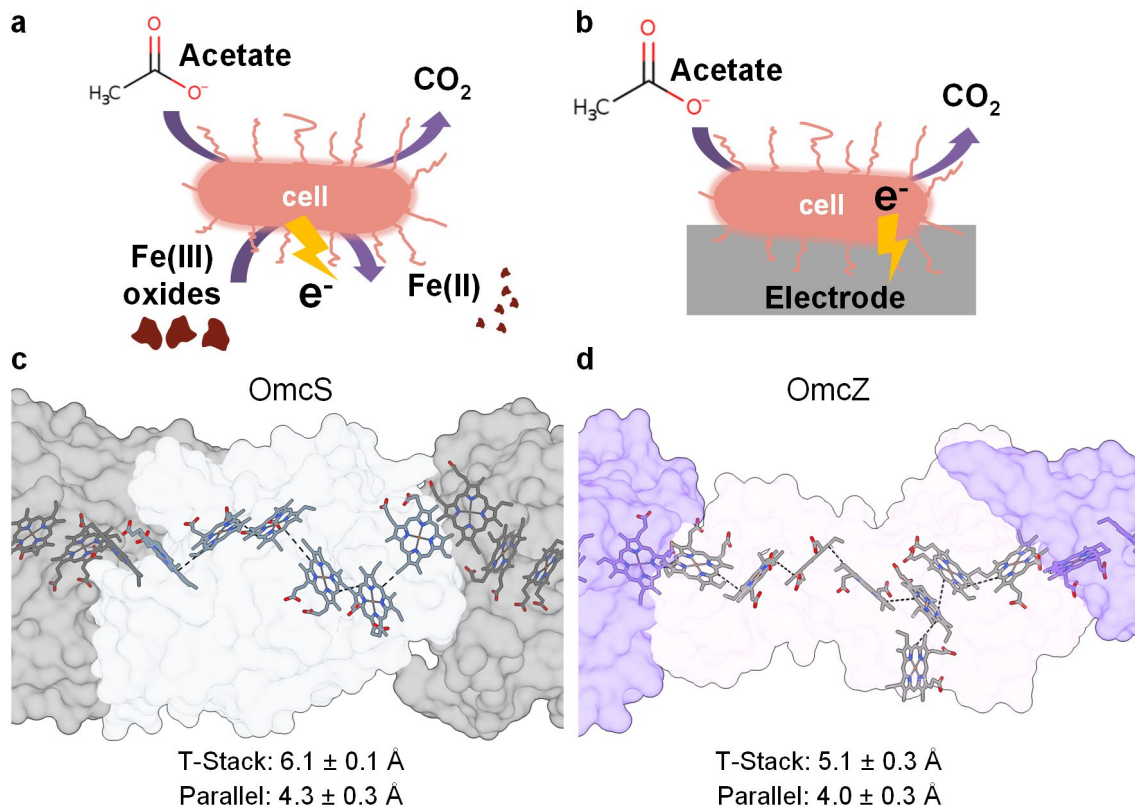


**Figure 1.1: Structural differences in important microbial nanowires revealed by cryo-EM.**

Growth of anaerobic *G.s.* on insoluble Fe(III) oxides (**a**) and an electrode (**b**) as the terminal electron acceptor **c**, OmcS nanowires showing subunits with 6 hemes and average inter-heme spacing shown as dashed lines indicated below. **d**, OmcZ nanowires showing subunits with 8 hemes and average inter-heme spacing shown as dashed lines indicated below.

its environment<sup>10</sup>. *Geobacter sulfurreducens* (*G.s.*) has been a model system of study due to its accessible genetic system and success in isolated culture growth making it possible to systematically evaluate physiological responses to mutations of key metabolic components<sup>11-13</sup>.

*Geobacter sulfurreducens* (*G.s.*) uses direct extracellular electron transfer (EET) to transport electrons generated by the TCA cycle through the inner and outer membrane to external electron acceptors including metal oxides by direct contact (Figure 1.1a)<sup>14</sup>.

Using direct EET, cells can also grow on electrodes in large cohesive communities called biofilms which can be as thick as 100  $\mu\text{m}$  (Figure 1.1b)<sup>15, 16</sup>.

It was discovered that *G.s.* produces extracellular filaments and proposed that they could aid cells in reducing external electron acceptors<sup>17</sup>. Filaments would be an efficient way for *G.s.* cells to increase their effective surface area enabling reduction of more insoluble Fe(III) oxide to maintain metabolic rates<sup>6</sup>. Studies confirmed that filaments were necessary for growth on insoluble Fe(III) oxides and that they were conductive, or able to transport electrons, cementing the term ‘microbial nanowire’<sup>17</sup>. Initial studies proposed these filaments to be only composed of modified Type IV pili, PilA-N<sup>17</sup>. However, after years of continuing research, structural and biochemical evidence revealed that *G.s.* produces a multitude of extracellular filaments. These include filaments of polymerized cytochromes OmcS and OmcZ under growth conditions that require EET in addition to pili, OmcE, and DNA filaments in mutant strains under other conditions<sup>18-22</sup>. Because OmcS and OmcZ are essential under physiologically relevant conditions such as growth on Fe(III) oxides and growth on electrodes respectively they remain the focus of this work<sup>23, 24</sup>.

Cryo-EM reveals OmcS is a hexaheme cytochrome (~45 kDa) that forms a 3.5 nm filament with seamless heme stacking along the length<sup>18</sup> (Figure 1.1c). It is apparent in wild-type (WT) cells in both fumarate-grown liquid cultures and electrode-grown biofilms<sup>18</sup>. OmcZ is an octaheme cytochrome that has a large 50 kDa form and a small 30 kDa form; OmcZ<sub>50</sub> and OmcZ<sub>30</sub>, respectively<sup>24</sup>. The OmcZ filament is 2.5 nm, formed by OmcZ<sub>30</sub>, and also exhibits seamless heme stacking along its length (Figure 1.1d). The heme geometries of OmcZ and OmcS are different, with OmcZ having closer heme stacking on average and a more solvent-exposed heme that breaks from the central chain<sup>22</sup> (Figure 1.1d). Both filaments are conductive, and thus can be termed microbial

nanowires, however OmcZ is more conductive than OmcS<sup>19</sup>. The intrinsic structural and electronic differences in the nanowires are expected to influence their physiological roles. Most of the previous work has examined the physiological importance of OmcS and OmcZ in EET under the guise that they remain monomeric extracellularly. With the knowledge that they polymerize into conductive nanowires, it is necessary to develop new models of EET using newly collected biophysical and biochemical data.

In addition to their physiological roles, microbial nanowires are good candidates for biomaterials because they are conductive, have high surface area, are biocompatible, and have potential for self-assembly<sup>3,25</sup>. One study has explored using nanowire films as a power source for small electronics<sup>26</sup>. Tunability of electronic properties is an additional crucial feature for proper material design but requires knowledge of underlying mechanisms of charge transport. Biological materials have the advantage of genetic manipulation which can be used to control functionality. Mutations can be explored computationally rather quickly for performance enhancement but must be eventually validated experimentally. Even simple mutations can result in complicated pleiotropic effects<sup>21</sup>. Another route is perturbation of the material by a non-invasive route like doping, optical excitation, or modification of active groups<sup>4</sup>. Because OmcS and OmcZ nanowires have heme groups, known to be critical in protein ETp measurements, there are many opportunities to tune nanowires by targeting the heme environment, for example replacing the heme iron<sup>4</sup>, but these avenues have yet to be investigated. Tuning nanowire properties may also change biofilms' behavior, as it has already been shown that introduction of OmcS to biofilms of photoactive cyanobacteria widely increased catalytic performance<sup>27</sup>. With increasing interest in using biofilms for light-driven

chemical synthesis and fuel production<sup>28</sup> as well as bioplastics<sup>29</sup> and wearable devices<sup>30</sup>, understanding how to tune biofilms is immediately relevant for an emerging new class of sustainable biomaterials.

## 1.1 Overview

In this thesis I will discuss four main aims related to electron conduction through biomaterials. Chapter 2 presents a model system to better understand the fundamentals of micrometer-long electron transport through proteins. Amyloid peptide crystals with atomically resolved structures are used to evaluate charge transport through the aromatic amino acid tyrosine, which is globally critical for charge transfer<sup>1</sup>. Chapter 3 discusses the physiological role of OmcS nanowires in EET by reevaluating their redox potential and interactions with periplasmic cytochromes. Chapter 4 examines the functional role of OmcS and OmcZ nanowires in microbial biofilms with a focus on wild type and knockout strains deficient in either nanowire,  $\Delta omcS$  and  $\Delta omcZ$ . Electrochemical and biochemical studies are used to find how biofilms adapt over time using extracellular nanowire expression. Finally, Chapter 5 examines microbial nanowires as tunable, optically functional biomaterials. Lasers are used to excite both living biofilms and nanowires to demonstrate intrinsic photoconductivity without the addition of external dyes or molecules.

## **2. Using peptide crystals with stacked tyrosines as model system**

*Intrinsic electronic conductivity of individual atomically-resolved amyloid crystals reveals micrometer-long hole hopping via tyrosines*

Catharine C. Shipp, H. Ray Kelly, Peter J. Dahl, Sophia M. Yi, Dennis Vu, David Boyer, Calina Glynn, Michael R. Sawaya, David Eisenberg, Victor S. Batista, and Nikhil S. Malvankar

This chapter is a modified version of a published paper<sup>31</sup>.

DOI: <https://doi.org/10.1073/pnas.2014139118>

### **2.1 Author Contributions**

C.C.S., V.B., and N.M. designed research; C.C.S. performed all experiments on protein crystals with help from S.Y. on initial design. H.R.K. and P.D. performed computations. M.S., D.B., C.G., and D.E. contributed new reagents/analytical tools; C.C.S., H.R.K., P.D., and N. M. analyzed data; and C.C.S. and N.M. wrote the paper.

### **2.2 Summary**

Proteins are commonly known to transfer electrons over distances limited to a few nanometers. However, many biological processes require electron transport over far longer distances. For example, soil and sediment bacteria transport electrons, over hundreds of micrometers to even centimeters, via putative filamentous proteins rich in aromatic residues. However, measurements of true protein conductivity have been hampered by artifacts due to large contact resistances between proteins and electrodes. Using individual amyloid protein crystals with atomic-resolution structures as a model system, I perform contact-free measurements of intrinsic electronic conductivity using a 4-electrode approach. I find hole transport through micrometer-long stacked tyrosines at

physiologically relevant potentials. Notably, the transport rate through tyrosines ( $10^5 \text{ s}^{-1}$ ) is comparable to cytochromes. Our studies therefore show that amyloid proteins can efficiently transport charges, under ordinary thermal conditions, without any need for redox-active metal cofactors, large driving force, or photosensitizers to generate a high oxidation state for charge injection. By measuring conductivity as a function of molecular length, voltage, and temperature, while eliminating the dominant contribution of contact resistances, I show that a multi-step hopping mechanism (comprised of multiple tunneling steps), not single step tunneling, explains the measured conductivity. Combined experimental and computational studies reveal that proton-coupled electron transfer confers conductivity; both the energetics of the proton acceptor, a neighboring glutamine, and its proximity to tyrosine influence the hole transport rate through a proton rocking mechanism. Surprisingly, conductivity increases 200-fold upon cooling due to higher availability of the proton acceptor by increased hydrogen-bonding.

### **2.3 Significance Statement**

The ability to understand and modulate protein conductance is central to many biological processes and for the technological applications of electronic biomaterials. However, measurements of intrinsic protein conductivity are lacking. Here, I employ a four-electrode method to measure contact-free electronic conductivity of an individual protein microcrystal that exhibits efficient hole transport over micrometers via stacked tyrosines. Combined experimental and computational studies show that both the energetics and proximity of the proton acceptor to tyrosine determine the rate of hole transport. Our mechanistic studies on model systems with atomic-resolution structures may help identify design principles to engineer electronic conductivity in proteins of

interest for a wide range of applications, including artificial photosynthesis, biocatalysis, prevention of oxidative damage, and nucleic acid biosynthesis.

## 2.4 Introduction

Many biological processes require electron transport over far longer distances than the 25 Å allowed by single-step tunneling<sup>32</sup>. The aromatic amino acids tyrosine and tryptophan, strategically placed between cofactors in proteins, can provide the critical stepping stones for multi-step hopping by acting as intermediaries along the electron transfer route as in Photosystem II and ribonucleotide reductase<sup>32, 33</sup>. In addition, chains of aromatic residues have been proposed to move hole carriers from enzyme active sites to the exterior of proteins to avoid oxidative damage caused by redox cofactors, but direct experimental evidence of charge transport beyond the nanometer scale is lacking<sup>34, 35</sup>. The ubiquity of such chains observed in proteins, and the established role of aromatic amino acids in the above biological processes, motivates mechanistic studies of how electron transport via aromatic residues can scale over mesoscopic (hundreds of nanometers) to microscopic distances<sup>32, 33</sup>.

A remarkable example of biological long-distance electron transport is by soil<sup>18, 19</sup> and sediment bacteria<sup>36, 37</sup> that carry electrons to remote acceptors hundreds of micrometers<sup>19, 38</sup> to centimeters away<sup>5, 36-38</sup>, 10,000-times the size of the cell. This long-distance transport enables bacteria to get rid of electrons derived from metabolism and survive in harsh environments that lack soluble, membrane-ingestible electron acceptors such as oxygen. Polymerized cytochromes produced by soil bacteria function as “microbial nanowires” by transporting electrons through seamlessly stacked hemes<sup>18, 19</sup>. In addition, filamentous proteins produced by both soil<sup>39</sup> and sediment bacteria<sup>37</sup> have

been shown to be conductive, even in the absence of cytochromes <sup>37</sup>. However, the underlying conductivity mechanism is unclear. Aromatic residues present in these filamentous proteins of soil <sup>39</sup> and sediment bacteria <sup>5</sup> have been proposed to carry electrons over long distances. However, this hypothesis is open to question because previous studies of DNA conductivity have shown that charge transport through aromatic bases is not possible beyond nanometer distances <sup>40, 41</sup>, even using a very large driving force ( $> 5V$ ) and synthetic bases <sup>41</sup>.

Many soluble proteins aggregate into an insoluble amyloid state to form elongated, unbranched fibrils that are associated with several fatal diseases, such as Alzheimer's, type II diabetes, and some types of cancers <sup>25</sup>. Amyloids are attractive model systems to evaluate protein conductivity mechanisms due to their unique ability to form several distinct, highly-ordered, self-replicating, and stable biomimetic structures (Figure 2.1). Short peptide-based amyloids are particularly attractive because of their computationally-guided, autonomous, and high-precision synthesis as well as their diverse chemical properties and biocompatibility.

In addition to their biomedical importance, amyloids are attractive biomaterials due to their high stability and capacity to reproduce themselves by seeding, enabling the development of self-repairing and replicating biomimetic materials <sup>25</sup>. However, two major bottlenecks remain in the use of amyloids as a model system to evaluate conduction mechanisms and for the development of protein-based multifunctional biomaterials. First, like most proteins, amyloids lack electronic or optical functionality <sup>42</sup>, <sup>43</sup>, and in prior studies of protein conductivity, high contact resistance - either between proteins or at the protein-electrode interface - has been shown to mask the intrinsic

electronic properties<sup>44</sup>. Second, in contrast to over 100,000 structures of globular proteins, only a few dozen amyloid fibril structures are available<sup>25</sup>, and conformational changes induced by experimental conditions, such as added dyes or tags, hinder the elucidation of structure-function correlations<sup>45-47</sup>.

To address both these bottlenecks, here I employ a strategy to measure intrinsic conductivity of pristine amyloid microcrystals, with atomic resolution structures<sup>48,49</sup>, aiming to correlate structure with function by avoiding modification or tagged molecules that can induce large conformational changes<sup>45-47</sup>. I use individual microcrystals with defined geometry to perform measurements of charge transport through stacked tyrosines, or along the fibril axis (Figure 2.1, Figure 2.2). Notably, I employ a four-

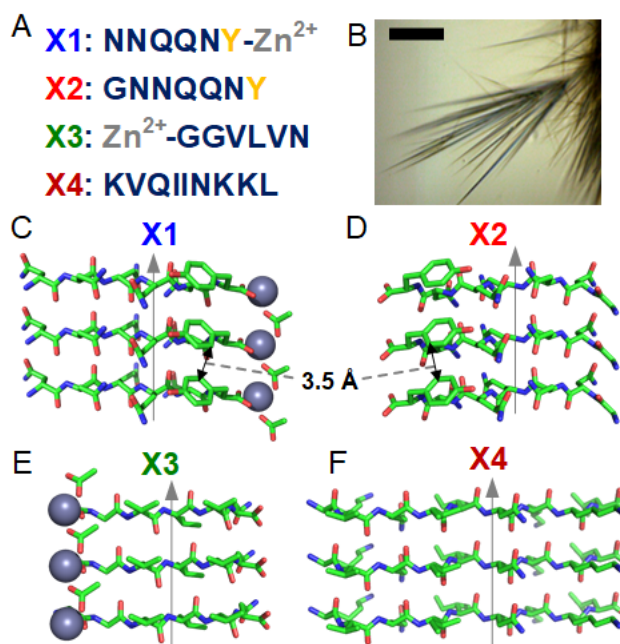


**Figure 2.1: Strategy to evaluate protein conductivity mechanism using short peptides as building blocks for model systems.**

**A**, Amino acid sequences of the short peptides used with Tyrosine (yellow) and zinc (grey) highlighted. **B**, Light microscopy image of microcrystals, scale bar 50  $\mu\text{m}$ . **C-F**, Atomic structures of microcrystals with grey arrows indicating the direction of the fibril axis. **C**, X1: Zn<sup>2+</sup>NNQQNY (PDB 5K2E) **D**, X2: GNNQQNY (PDB 5K2G) **E**, X3: Zn<sup>2+</sup>GGVLVN (PDB 3PPD). **F**, X4: KVQIINKKL (PDB 6NK4) Tyrosine edge-to-edge distances are 3.5 Å. Chemical elements are shown as green: carbon, blue: nitrogen, red: oxygen, grey: zinc.

electrode system with ionically-blocking electrodes and measure steady-state electronic current<sup>38,44</sup> to avoid artifacts due to contact resistance<sup>50,51</sup>, polarization resistance<sup>52</sup>, and ionic currents<sup>50</sup>, which are known to mask the intrinsic conductivity of the protein<sup>50,53</sup>. Our studies show that amyloid proteins can efficiently transport charges over micrometer distances under ordinary thermal conditions without any need for redox-active metal cofactors. In contrast to single-step tunneling commonly observed in proteins, I find evidence for a hopping mechanism, previously observed experimentally only in synthetic conjugated molecular wires<sup>54,55</sup>, to account for long-distance conductivity.

## **2.5 Results**

### **2.5.1. Strategy to Measure Contact-Free Electron Transport in Proteins to Determine Intrinsic Conductivity**

Although charge transfer over nanometers is well documented in several protein systems<sup>56</sup>, contact-free DC conductivity measurements of intrinsic charge transport have not been performed for any well-defined proteins, to our knowledge. During charge transfer, electrons are exchanged between donor and acceptor molecules within nanometer distances and remain localized on the protein. In contrast, conductivity measurements involve the passage of charge through a protein without charge residing on the protein<sup>57</sup>. Such conductivity measurements are extremely challenging due to contact resistances obscuring the intrinsic conductivity, as most of the applied voltage drop occurs across the contacts<sup>50,53</sup>. Even single molecule measurements have shown that protein conductance is strongly affected by the nature of contacts<sup>50,53,54</sup>. Therefore, previous measurements of single molecule protein conductance have emphasized the

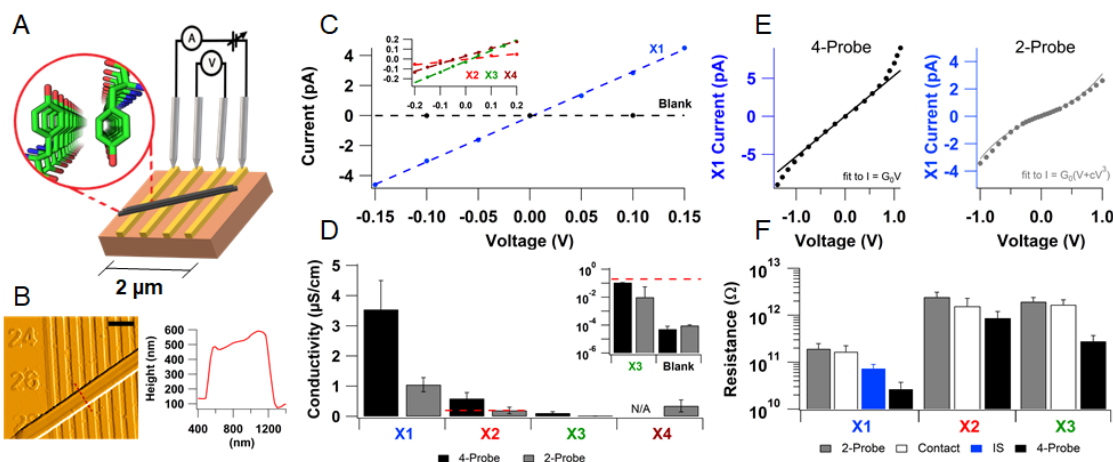


**Figure 2.2: Intrinsic conductivity measurements of amyloids reveal micrometer-long charge transport through stacked tyrosines.**

**A**, A schematic for measuring the intrinsic conductivity of a protein crystal (black) using 4-probes. Inset: Atomic structure of **X1** showing stacked tyrosines. **B**, (*left*) Atomic Force Microscopy image of **X1** crystal spanning multiple electrodes and (*right*) corresponding height profile at the red dotted line. Scale bar in **B**, 1  $\mu\text{m}$ . **C**, Representative current-voltage (I-V) curves taken by two-probe electrical measurements. The dashed lines are linear fits to the data shown. Inset: Zoomed I-V curve for low-conductive microcrystals. **D**, Comparisons of the four-probe (black) and two-probe (grey) conductivity of the microcrystals. Inset: Zoomed values (below **X2** two-probe dashed red line) on a log scale. **E**, The average two-probe, contact, AC impedance spectroscopy (IS), and four-probe resistance of applicable microcrystals. Bars represent mean + standard error of the mean (S.E.M) of multiple replicates [n (2-Probe) = 19, 8, 9, 4 and n (4-Probe) = 8, 9, 6 for **X1**, **X2**, **X3**, and **X4** respectively. n (IS) = 11]. **F**, Comparison of current-voltage profile for **X1** measured using (*left*) four- and (*right*) two-probe method.

pressing need to inject charges into the protein interior via ligands or good contacts for reliable determination of protein conductance<sup>53</sup>.

To avoid artifacts due to electrode polarization and contact resistance developed at the interface between the protein and electrode<sup>44</sup>, here I employ a 4-electrode setup in which I applied the current ( $I$ ) to the outer 2 electrodes and measured the direct current (DC) voltage ( $V$ ) across the inner 2 electrodes (Figure 2.2A). As no current can flow through the inner circuit due to the high impedance of the voltmeter, this method eliminates artifacts due to contacts and electrode polarization and enables the determination of intrinsic conductivity<sup>44</sup>. Furthermore, the carrier injection can be controlled precisely by ensuring current conservation between the outer two electrodes

and maintaining the voltage between the inner electrodes larger than thermal energy ( $k_B T$ ). This setup thus avoids any electrochemical processes or the need for photosensitizer to generate high oxidation states of aromatic residues<sup>56</sup>. By eliminating hot carrier injection, this method enables measurements of conductivity in its truest sense to evaluate whether there are free charge carriers that can move under ordinary thermal conditions<sup>58</sup>. We had previously applied the four-probe method to measure networks of microbial nanowires, which eliminates the contact resistance between the protein and electrode<sup>38</sup>. However, the inter-filament contact resistance dominated the overall response, leading to 1000-fold lower conductivity<sup>38</sup> than individual nanowires<sup>18, 19</sup>. Therefore, here I measure individual protein crystals with atomic-resolution structures using a 4-probe method to determine the intrinsic conductivity mechanism.

### **2.5.2. Micrometer-long Chains of Stacked Tyrosines Confer Conductivity to Amyloids.**

I selected for comparison four amyloid fibril-forming peptides with atomic-resolution structures to probe how charge transport is affected by periodic stacking of tyrosine and metals (non-redox-active  $Zn^{2+}$ ): 1) **X1**:  $Zn^{2+}NNQQNY$ ; 2) **X2**:  $GNNQQNY$ ; 3) **X3**:  $Zn^{2+}GGVLVN$ ; and 4) **X4**:  $KVQIINKKL$  (Figure 2.1). These fibril-forming peptides form elongated microcrystals (Figure 2.1. B) where, like natural amyloid fibrils, the peptides form extended parallel  $\beta$ -sheets whose constituent  $\beta$ -strands run perpendicular to the fibril axis, with both fibrils and microcrystals having similar diffraction patterns<sup>59</sup>. In contrast to large macromolecular systems, the minimalistic nature of this system (6-9 residue peptides and metal ion) is helpful in identifying components essential for engineering desired functionalities.

I individually placed each microcrystal on gold electrodes separated by 300 nm non-conductive gaps and located their electrode contacts using atomic force microscopy (AFM; Figure 2.2B). I performed measurements at atmospheric pressure.

All four peptide microcrystals showed conductivity with linear (Ohmic) current-voltage behavior in two-probe measurements (Figure 2.2C). I calculated the microcrystal conductivity from the measured conductance using a conformal mapping technique accounting for the microcrystal and electrode device dimensions (Equation 2.1, See Methods) <sup>38</sup>.

$$\sigma = \frac{-\pi G}{L} * \ln \left( \frac{1 + \tanh \frac{\pi a}{2g}}{4 \tanh \frac{\pi b}{2g}} \right)^{-1} \quad 2.1$$

I found that **X1** had the highest conductivity among all four microcrystals (Figure 2.2D) and even the lower conducting microcrystals had higher conductivity than a blank device ( $93.4 \pm 31.6$  pS/cm) (Figure 2.2 inset). As expected, four-probe measurements showed higher conductivity than two-probe, and the conductivity of **X1** was significantly higher ( $p \leq 0.05$ ) than the conductivity of the other peptides (Figure 2.2).

The mean four-probe conductance of a single **X1** microcrystal was  $74.8 \pm 19.9$  pS, which is the highest conductance reported for a single amyloid protein macrostructure <sup>60</sup>. Although conductance values have been reported in networks of amyloid and peptide fibrils <sup>61-64</sup>, the lack of a consistent, uniform macromolecular conformation of amyloids as well as the dependence of conductance values on electrode and sample geometries prevented direct comparisons between these measurements <sup>65</sup>. The electrical resistance of the sample measured using the two-probe method is dependent on the crystal size and the

nature of contacts whereas the four-probe conductivity is an intrinsic property of the material. The mean four-probe conductivity of the **X1** microcrystal was  $3.5 \pm 0.96 \mu\text{S/cm}$  (Figure 2.2), which is the highest conductivity for amyloids reported to date, to our knowledge. As expected, the conductivity through proteins without metal cofactors is lower than the conductivity of other conducting proteins such as the polymerized cytochrome filaments of *Geobacter sulfurreducens* that transport electrons via stacked hemes rather than tyrosines<sup>18, 19</sup>. The **X2** microcrystal that lacked metal ions, but contained stacked aromatics, showed a 6-fold lower conductivity ( $0.59 \pm 0.20 \mu\text{S/cm}$ ) than **X1**. The **X3** microcrystal that lacked tyrosines showed the lowest four-probe conductivity ( $0.11 \pm 0.045 \mu\text{S/cm}$ ) which is 32-times lower than **X1**. Our studies thus show that although other amino acids can also contribute to protein conductivity, stacked tyrosines provide a more efficient transport path for conductivity. The microcrystals of **X4** that lacked both tyrosines and metal ions were too short for four-probe measurements; they exhibited low two-probe conductivity ( $0.35 \pm 0.20 \mu\text{S/cm}$ ). Both **X3** and **X4** lack stacked tyrosines; however, the two-probe conductivity of **X4** was higher than both two- and four-probe conductivity of **X3**. This could be due to the differences in contact resistances as our results show that two-probe resistance values are comparable to the contact resistance (Figure 2.2). It could also be due to the basic residues (lysines) included in the **X4** sequence, but intrinsic conductivity is required for direct comparison<sup>66</sup>. Both **X1** and **X2** have tyrosines with a suitable arrangement for  $\pi$ -stacking interactions at  $3.56 \text{ \AA}$ <sup>67</sup>. Therefore, our measurements indicate that stacked tyrosines can transport charges over micrometer distances even in the absence of strong oxidants that are typically required to oxidize individual tyrosines for conductivity<sup>68</sup>.

The contact resistance (the difference between measured two- and four-probe resistances) for all microcrystals was substantially higher or comparable to the intrinsic (four-probe) resistance (Figure 2.2), demonstrating the large influence of contacts on conductivity measurements of proteins. For **X3** and **X1**, the contact resistance was about 6-fold higher than the intrinsic resistance whereas for **X2** it was 2-fold higher. All measurements confirm that significant contact resistance masks the true conductivity of these proteins in the two-probe setup because most of the voltage drop occurs across the contacts. Differences in measured contact resistances are likely due to differences in microcrystal shape, composition, and size. Our results demonstrate that contact resistance plays a significant role in measurements of protein conductivity, even for samples with lower conductivity. Our micrometer-scale studies thus complement and extend previous single-molecule studies which have shown that contact resistance masks the intrinsic conductance of biomolecules<sup>50, 51, 69</sup>.

To complement DC conductivity measurements, I performed AC impedance spectroscopy (IS) to separate electronic and ionic conductivity<sup>38</sup>. I fit the data to the equivalent circuit containing only electrode capacitance and crystal resistance (Figure 2.3). Because there is no additional plateau in impedance at higher frequency, I determined that the IS of a single **X1** microcrystal showed that there was no major ionic contribution to the sample conductivity (Figure 2.3)<sup>38</sup>. Acidic and basic side chains have been known to increase the ionic conductivity in some cases<sup>66, 70</sup>. Therefore, the lack of charged residues in the **X1** peptide is consistent with the lack of ionic current in these microcrystals. Resistance values extracted from an equivalent circuit analysis of these AC measurements were comparable to DC resistance values, thus validating our

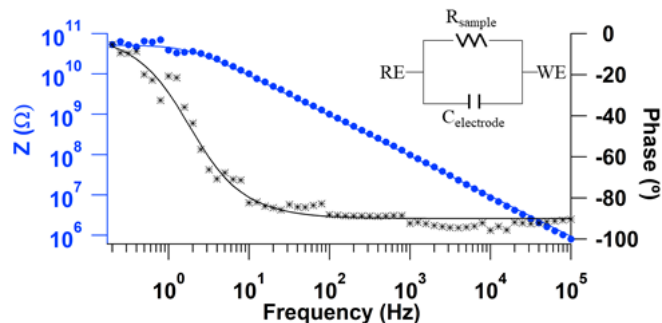


**Figure 2.3: Impedance spectroscopy confirms purely electronic conductivity in amyloids.** AC impedance spectroscopy (IS) on **X1** single crystals. (Inset) The circuit diagram used to fit to the data. The fits for a circuit with a true capacitor were compared to those modeled with a constant phase element and no significant differences were seen.

measurement approach that measured conductivity by 4-probe method is primarily electronic in nature (Figure 2.2E).

### 2.5.3. Increased Structural Rigidity of Amyloids due to Metal Ions Enhances Conductivity

The conductivity of **X1** was higher than **X2** despite having nearly identical structures with close tyrosine stacking. The main difference between these two structures is the introduction of  $Zn^{2+}$  in **X1** instead of glycine (Figure 2.1C and D). As the tyrosines and surrounding residues are conserved, it would be expected that both microcrystals have similar conductivity. However, redox activity or charge transfer involving tyrosine is typically proton-coupled owing to the high acidity of oxidized tyrosine ( $pK_a \sim -2$ )<sup>71</sup>, which gives rise to proton-coupled electron transfer (PCET). Because tyrosine participates in PCET, any changes in the hydrogen bonding network surrounding tyrosine can modulate the rate of charge transfer<sup>1,71</sup>. Notably, in both **X1** and **X2**, tyrosine is within close hydrogen bonding distance to the nearest glutamine sidechain ( $pK_a \sim 2$ ), positioning the glutamine as a probable proton acceptor for proton transfer (PT)<sup>1</sup>. The tyrosine OH could be stabilized in a stretched configuration by hydrogen bonding

interactions with the amide oxygen or nitrogen of the glutamine, analogously to the PT mechanism from Tyr to Gln proposed for the blue-light using FAD (BLUF) domain protein<sup>72-74</sup>.

My coauthors performed molecular dynamics (MD) simulations at 300 K to investigate ensembles of conformations of **X1** and **X2** and examine their hydrogen-bonding networks. To analyze structural changes involving charge transfer residues, we monitored three key distances over the MD trajectories: tyrosine edge-to-edge, tyrosine hydroxyl-oxygen (Tyr-O) to glutamine amide-oxygen (Gln-O), and Tyr-O to glutamine amide-nitrogen (Gln-N) (Figure 2.4A-C). The comparison of **X1** and **X2** revealed that  $Zn^{2+}$  stabilizes the microcrystal structure of **X1**, as evidenced by the wider tyrosine edge-to-edge distance distribution in **X2**, with a larger tail compared to **X1** which could reduce electron hopping in **X2** (Figure 2.4A). There was no significant difference in crystal packing of **X1** and **X2** to explain the difference in distributions<sup>59</sup>.

Analysis of the other key distances showed that the glutamine can form two distinct rotamer forms designated R1 and R2, with the Gln-O or Gln-N closest to the tyrosine, respectively (Figure 2.4D and E). **X1** can stably form the R1 conformation which becomes more prominent as temperature is lowered (Figure 2.4B and Figure 2.7C). In addition, it has a high likelihood of remaining at distances around 3.8 Å for Tyr-O to Gln-O and 3.4 Å for Tyr-O to Gln-N at 300 K (Figure 2.4B). PT rates are known to depend strongly on the proton donor-acceptor distances<sup>71,74</sup>. Therefore, our analysis suggests that when the R1 conformation is stabilized by  $Zn^{2+}$ , the Gln-O is the preferred proton acceptor in **X1**, whereas when the R1 conformation is not stabilized both the Gln-O and N are equally accessible. In contrast, the **X2** microcrystal was more likely to form the R2

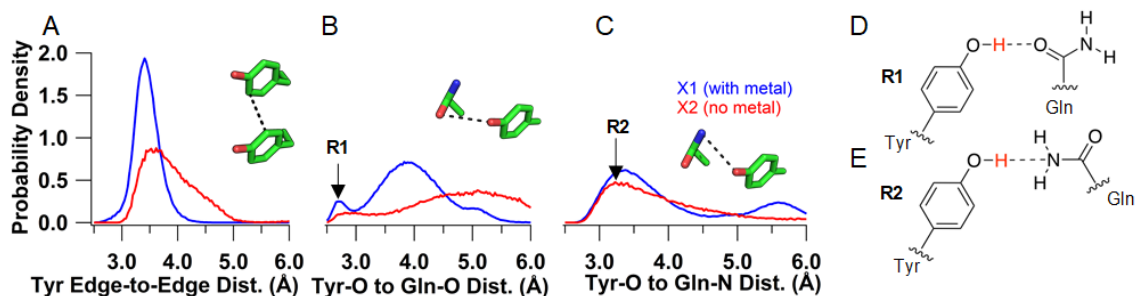


**Figure 2.4: Tyrosine stacking and proton acceptor availability govern conductivity.**

MD simulations at 300 K to compare the order of **X1** (blue) and **X2** (red) crystals. (A-C) Probability density distributions of the separation between key residues. **A**, Tyrosine edge-to-edge distance. **B**, Tyrosine hydroxyl-oxygen to glutamine amide-oxygen distance with the R1 conformation labelled at the 2.7 Å peak of **X1**. **C**, Tyrosine hydroxyl-oxygen to glutamine amide-nitrogen distance with the R2 conformation labelled at the 3.24 Å peak in **X2**. Insets show the distances measured with a black dotted line. **D**, Chemical representation of the R1 and **E**, R2 rotamers.

conformation at 300 K as evidenced by the larger probability of short Gln-N distances (3.2 Å), indicating the most probable proton acceptor in **X2** is the Gln-N (Figure 2.4C).

Considering that **X1** and **X2** would primarily utilize the closest available proton acceptor for PCET, charge transfer would likely be overall slower in **X2** because it has larger mean tyrosine edge-to-edge separations and proton donor-acceptor distances when compared to **X1**.

In addition to hydrogen bond network changes from thermal fluctuations, electronic effects that modulate the pKa of any residues surrounding the charge transfer region could also regulate PCET<sup>1</sup>. Although Zn<sup>2+</sup> is not redox active and cannot directly take part in electron transport, it could potentially lower the pKa of residues by up to 4 pH units which would facilitate PCET<sup>75</sup>. However, our density functional theory (DFT) calculations showed that Zn<sup>2+</sup> does not significantly change the pKa of tyrosine in **X1** microcrystals (SI Table 3), confirming that it must play a primarily structural role. In summary, **X1**, which contains a readily available proton acceptor and rigid tyrosine stacking, displays higher conductivity than **X2**. This suggests that ordered metal incorporation likely enhances conductivity by making the structure more rigid,

preventing thermal fluctuations from disrupting the charge transport pathway and stabilizing the R1 conformation.

#### 2.5.4. DFT suggests Hole Conductivity due to Proton Rocking and the Energetics of Proton Acceptor Determines the Transport Rate.

Our MD simulations combined with conductivity measurements indicated that the surrounding hydrogen-bonding network was fundamental to charge transport in the highest conducting amyloids, **X1**, by maintaining close tyrosine stacking and short proton donor-acceptor distance for PCET. To explore the possibility that proton transfer can occur in **X1**, my coauthors performed DFT calculations on model amyloid chains (SI Fig. 2 and SI Table 4). Due to the presence of both R1 and R2 rotamers in our MD simulations (Figure 2.4D and E), they included both forms in their calculations. Relaxed

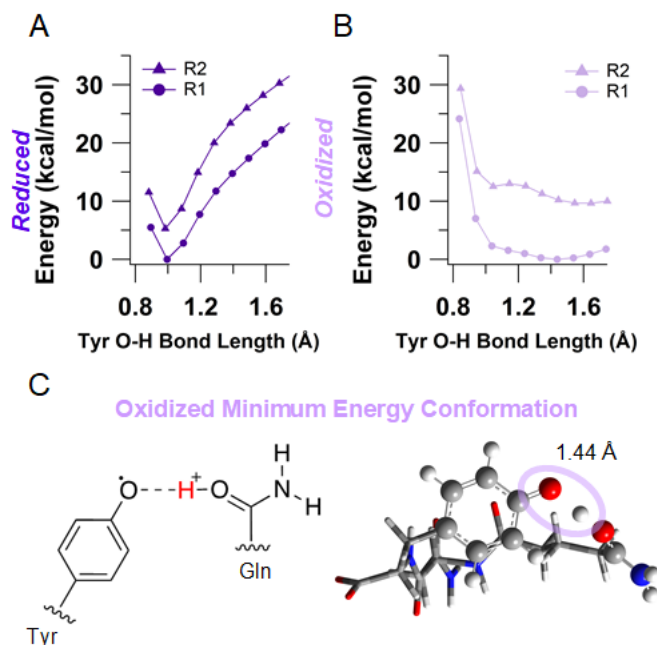


**Figure 2.5: DFT calculations confirm proton transfer in oxidized X1.**

Relaxed potential energy scan for reduced, **A**, and oxidized, **B**, **X1** in R1 and R2 conformations. Energy is normalized to the minimum value of R1 scans. **C**, Chemical structure of oxidized minimum energy conformation (left) and the DFT optimized geometry (right). The oval highlights the tyrosine O-H bond and the optimized bond length. Chemical elements are colored as grey: carbon, blue: nitrogen, red: oxygen, white: hydrogen.

potential energy scan calculations, in which geometry optimizations were performed at fixed tyrosine O-H distances with a polarizable continuum model for water, revealed that both reduced conformations (R1 and R2) had a single minimum at a tyrosine O-H bond distance of 1 Å suggesting that proton transfer does not occur (Figure 2.5A). In contrast, potential energy profiles for the oxidized R1 conformation indicated that there was no barrier to PT as the potential energy curve has a single-well shape characteristic of strong hydrogen bonds (Figure 2.5B)<sup>76</sup>. The oxidized R2 conformation was characterized by a low-barrier hydrogen bond with a barrier of 0.5 kcal/mol that can be overcome by thermal energy (Figure 2.5B). Thus, our DFT calculations showed that PT can readily proceed when the tyrosine is oxidized in the R1 conformation (Figure 2.5C), while it is unlikely to occur in the reduced state. Further, the R1 conformation is thermodynamically favored in the reduced form (5.3 kcal/mol) and even more so after oxidation (11.4 kcal/mol), consistent with the MD simulations for **X1** (Figure 2.7C; SI Tables 5 and 6). In the oxidized R1 conformation, the small energetic difference between protonated and deprotonated Tyr suggests that the proton can move back and forth readily. Therefore, we conclude that the single-well potential or proton transfer in this conformation may indicate a proton rocking mechanism, where the proton can be delocalized in the barrier-less energy well, in a manner similar to TyrZ in photosystem II and Tyr122 in ribonucleotide reductase<sup>1</sup>. The oxidation of tyrosine creates a positive charge that may be associated with ionic transport as seen in other systems<sup>77</sup>, however this proton rocking mechanism does not require long-range proton transport and is therefore consistent with our impedance experiments that did not show any ionic conductivity (Figure 2.3). Calculations performed in polarizable continuum models resembling the dielectric

environments inside and on the surface of proteins showed nearly identical results (SI Fig. 5 and SI Tables 4-6).

### **2.5.5. Stacking Substantially Lowers the Redox Potential of Tyrosine**

Our contact-free conductivity measurements were performed under ordinary thermal conditions at low bias potentials (Figure 2.2C). Because specific hydrogen bonding networks and hydrophobic protein environments can change the effective oxidizing potential of tyrosine my coauthors investigated the oxidation potential in the case of **X1**<sup>1</sup>. They performed DFT calculations of tyrosine in the R1 conformation of **X1** using implicit solvents with several dielectric constants and found that the maximum potential for oxidation was +0.8 V vs SHE or +5.2 V vs vacuum (SI Table 7). Comparison of one- and two-layer models of **X1** showed that tyrosine stacking lowers the oxidation potential by approximately 150 mV (SI Table 8). The calculated oxidation potential of tyrosine in **X1** is in proximity with reported values for the Fermi level of gold electrodes (approximately +5.1 V vs vacuum)<sup>78</sup>. This proximity between the redox potential of the tyrosine and the Fermi level of the electrode allows for charges to be injected even at low applied bias.

On the other hand, the oxidation potential of tyrosine in the R2 conformation was roughly 340 mV higher than R1 in all dielectric environments due to the facile proton transfer that stabilizes the oxidized R1 species. As the R1 conformation is also the thermodynamically favored conformation in the reduced state, we propose that the charge transport mechanism involves proton rocking in the R1 conformation.

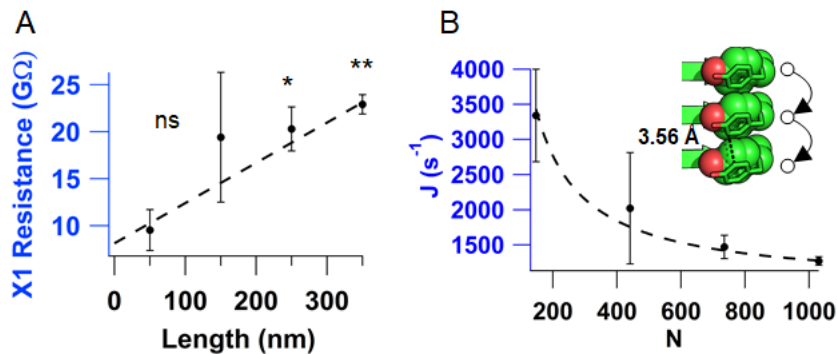


**Figure 2.6: Resistance increases linearly with crystal length, consistent with a hopping mechanism.** **A**, 4-probe resistance versus length measurements of **X1**. P-values: \* =  $p < 0.05$ , \*\* =  $p < 0.01$ . Linear fit  $R^2 = 0.8$ . **B**, Electron flux ( $J$ ) vs. number of carriers calculated from (A). Values represent mean  $\pm$  S.E.M. ( $n=3$ ). Inset: Schematic of hole hopping through tyrosines with their edge-to-edge distance labeled.

### 2.5.6. Resistance Increases Linearly with Protein Length Suggesting a Hopping Mechanism

The electrical resistance was measured as a function of microcrystal length (Figure 2.6A) to probe the mechanism of charge transport through the highest conducting amyloids (**X1**). The four-probe technique was adapted such that the first two probes remained stationary and the distance to the final two electrodes increased by one electrode after each measurement until the desired length was reached. The resistance versus length relationship for **X1** agreed well with the expected linear relationship of a hopping conductor. The calculated conductance from the linear fit yielded a conductivity of  $4.8 \pm 0.76 \mu\text{S/cm}$  in agreement with our measurements (Figure 2.2D). Although many proteins are shown to transport electrons by tunneling with the resistance increasing exponentially with distance<sup>50, 53</sup>, computational studies on longer peptides have predicted a transition from tunneling to hopping as a dominant transport mechanism<sup>79</sup>. In addition, computational studies on proteins have predicted hopping transport<sup>80, 81</sup>. Our finding of linearly increasing resistance suggests hole hopping between closely stacked tyrosines as a dominant mechanism of conductivity (Figure 2.6). Using a steady state hopping theory,

I estimated the hopping rate between tyrosines by using  $J = (k_{up} + k_{hop}/N)$  where  $k_{hop}$  is the hopping rate and  $k_{up}$  is related to injection rate from the electrode into the crystal<sup>82</sup>. By converting resistance into electron flux, and distance into the number of hopping steps, I found that hopping rate was  $\sim 10^5 \text{ s}^{-1}$  and  $k_{up}$  was  $\sim 10^2 \text{ s}^{-1}$  at 100 mV for **X1** (Figure 2.6B). These rate measurements suggest that transport through tyrosines is 1000-fold faster than the charge injection into the protein. This rate was estimated with the assumption that all tyrosines in the crystal contribute to measured current under uniform electric field. However, due to coplanar geometry of electrodes, the electric field is not uniform and possible defects in the crystal may lower the number of tyrosines participating in the transport. Therefore, the estimated rate represents a lower limit<sup>56</sup>. Nevertheless, the hopping rate measured at ordinary thermal conditions is comparable to rates for charge transfer in protein crystals with heme or metal cofactors<sup>82-84</sup> measured by photochemical injection methods.

### **2.5.7. Higher Availability of the Proton Acceptor leads to a 200-fold Increase in Amyloid Conductivity.**

Our DFT calculations and resistance versus length measurements suggest that proton rocking coupled with electron hopping is a likely mechanism for charge transport in **X1**. To further investigate the mechanism of conductivity, I analyzed the temperature dependence of the conductivity as measured in a four-probe configuration (Figure 2.7A-black). The conductivity increased exponentially to 260 K and then decreased exponentially to 225 K. The response was reversible without any hysteresis. An Arrhenius fit to the data for the 225-260 K range, using  $\sigma(T) = \sigma_0 \exp(\frac{T_0}{T})$  yielded an activation energy ( $k_B T_0$ ) of 0.77 eV. As nanoscale measurements have also reported

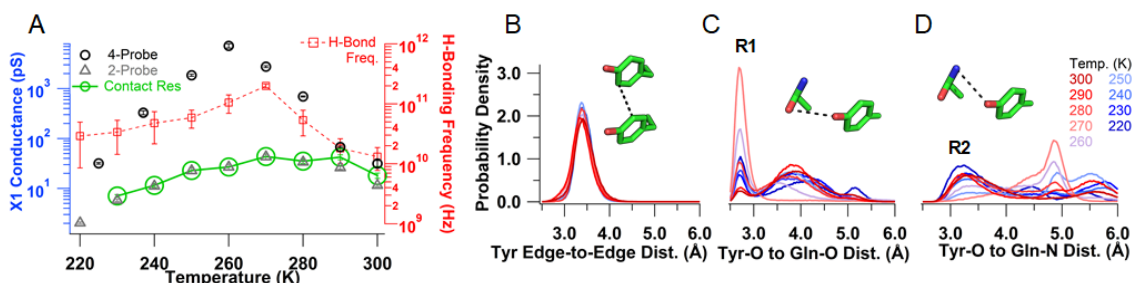


**Figure 2.7: Exponentially-Increasing Crystal Conductivity Upon Cooling Near Physiological Temperatures due to Increased Availability of Proton Acceptor.**

**A**, Temperature dependence of the **X1** conductance measured with a four-probe (black circles) and two-probe (grey triangles) arrangement. The green circles and solid line indicate the inverse of the contact resistance. Errors shown are fit errors to the linear region of an I-V curve measured as in Fig. 2 at each temperature. The calculated hydrogen bonding frequency between Tyr-O and Gln-O is also shown (red squares) with the S.E.M. reported for each temperature ( $n=6$ ). **B-D**, MD simulations from 300-200 K to determine changes in **X1** structure upon cooling. **B**, Tyrosine edge-to-edge distance. **C**, Tyrosine hydroxyl-oxygen to glutamine amide-oxygen distance with the labelled R1 conformation. **D**, Tyrosine hydroxyl-oxygen to glutamine amide-nitrogen distances with the labelled R2 conformation. Insets: the corresponding distances are indicated with a black dotted line with the residues colored as in curve measured as in Fig. 2 at each temperature. The calculated hydrogen bonding frequency between Tyr-O and Gln-O is also shown (red squares) with the S.E.M. reported for each temperature ( $n=6$ ). **B-D**, MD simulations from 300-200 K to determine changes in **X1** structure upon cooling. **B**, Tyrosine edge-to-edge distance. **C**, Tyrosine hydroxyl-oxygen to glutamine amide-oxygen distance with the labelled R1 conformation. **D**, Tyrosine hydroxyl-oxygen to glutamine amide-nitrogen distances with the labelled R2 conformation. Insets: the corresponding distances are indicated with a black dotted line with the residues colored as in Figure 2.1.

similar activation energy, our measurements thus establish that proteins can extend transport from nanometers to micrometers with no change in the activation energy<sup>56</sup>.

In contrast to the four-probe arrangement, two-probe measurements (Figure 2.7A-grey) showed a much weaker temperature dependence. The slopes in the major regions, 220-260 K and 260-300 K, decreased by 2 and 7-fold respectively compared to four-probe measurements (Figure 2.7A, SI Table 9). Notably, the changes in slope led to an activation energy of 0.30 eV in the 2-probe measurements, which is substantially lower than 0.77 eV measured using four-probe. Therefore, our studies indicate that the true activation energy can be severely underestimated when using the two-probe method due to large contact resistance.

Notably, the potentials corresponding to the measured activation energy are comparable to the potentials that enhance conductivity for both the two- and four-probe

measurements of current voltage curves (Figure 2.2F). The four-probe measurement showed an increase in conductance around 0.7 V indicated by linear behavior with a different slope. The two-probe measurement showed an increase around 0.3 V with behavior that fit well to a linear + cubic relationship, consistent with a Simmons model of a tunneling barrier forming at the contacts<sup>85</sup>. This response was reversible because reversing the polarity yielded similar non-linear region with similar slope (Figure 2.2F). These comparative measurements demonstrate that contact resistance strongly affects the two-probe measurements and the increase in current at low potentials is likely due to a barrier bending effect that decreases the contact resistance at higher bias<sup>85</sup>. Therefore, it is important to evaluate the role of contacts in prior studies that used two-probe and bulk methods to evaluate charge transport through aromatic amino acids, including tyrosines<sup>86-89</sup>.

The large differences in slopes between two- and four- probe measurements further underscore how contacts mask the true nature of protein conductance and why is it critical to measure intrinsic conductivity to determine underlying transport mechanisms. I compared the contact resistance to the sample response, which revealed that contact resistance dominates the response for two-probe measurements (Figure 2.7A-green circles). Thus, our measurements show that the contact resistance masks the true temperature dependence of protein conductivity in the two-probe approach, making it difficult to resolve the underlying conduction mechanism. This is important because previous studies have found different transport mechanisms based on temperature dependencies that were impacted by the contact resistance.

To understand the mechanism underlying a 200-fold increase in conductivity upon cooling, my coauthors performed MD simulations in the temperature range 300-220 K (Figure 2.7B-D). Our MD simulations at 300 K had indicated that the sidechains involved in charge transfer experienced substantial thermal fluctuations. Therefore, we examined these same key distances as the temperature was lowered. We found that the tyrosine edge-to-edge distance was well preserved for all temperatures with a peak around 3.4 Å (Figure 2.7B). The Tyr-O to Gln-O distance distribution sharpened to a prominent peak at 270 K and then returned to a broader distribution at 220 K (Figure 2.7C). My coauthors also computed temperature-dependent hydrogen bonding frequencies to account for both donor-acceptor distance and orientation. The probability of forming a hydrogen bond between Tyr-O and Gln-O (R1 conformation) increased by 15-fold when cooling from 300 to 270 K (Figure 2.7A). In contrast, hydrogen bonding between the Tyr-O and Gln-N (R2 conformation) was at least an order of magnitude less frequent than in the R1 conformation for all temperatures (SI Fig. 6). The observed increase in probability to form a hydrogen bond with the proton acceptor upon cooling in R1 is consistent with the increased conductivity (Figure 2.7A) indicating that the PT mechanism through the R1 conformation results in the most efficient charge transport. Thus, the observed temperature dependence of the **X1** microcrystal can be explained by a competition between the increasing availability of a proton acceptor and the decreasing thermal energy available for hopping as the temperature is lowered, resulting in a crossover at 260 K.

## 2.6 Discussion

Recent studies have identified the critical need to develop model systems to understand the mechanism of charge transport in proteins<sup>35</sup>. Here, I utilize four fibril forming short peptides with atomically resolved structures to determine how charge transport is influenced by the protein environment, aromatic residues, and metal ions. Our combined experimental and computational analysis suggest that PCET confers conductivity in amyloid microcrystals. The high conductivity of the **X1** microcrystals compared to the other examined microcrystals suggests that the presence of periodically stacked aromatic residues can mediate efficient charge transport with the availability of a nearby proton acceptor. Using a four-electrode setup, I measure intrinsic charge transport unaffected by contacts or other typical artifacts to determine the length- and temperature-dependencies of conductivity. With recent advances in fabrication of nanoscale electrodes down to sub-nanometer<sup>90</sup>, this method could be widely applicable to a large number of biomolecular systems irrespective of their size<sup>18, 38, 44</sup>.

It has been suggested that chains of redox active amino acids could serve a biological role by mediating hole hopping to prevent oxidative damage of enzyme active sites<sup>34</sup>. Here, I provide direct evidence that proteins can transport charges over micrometer distances under low applied bias potentials via stacked tyrosine residues. Our study shows that carefully structured protein environments can lead to tyrosine oxidation well below the standard oxidizing potential and without any need for a photosensitizer to generate a high oxidation state. We also found that rigidity of the structure, enhanced by the incorporation of a metal ion, is important in maintaining the efficiency of the charge transport pathway as suggested by the higher conductivity of **X1** than **X2** microcrystals.

Both structures showed higher conductivity than metal-incorporated peptide microcrystals that lacked tyrosine residues (**X3**), demonstrating the crucial role of aromatic residues as a hopping step for transport. We have thus employed both theory and experiments to develop a model for charge transport in these peptide crystals.

Computational studies on modeling of current in filaments of *Shewanella oneidensis* have also invoked multi-step hopping models<sup>81</sup>. These studies concluded that to account for observed currents, charge localizing sites need to be within 1 nm even if reorganization energies are assumed to be zero<sup>81</sup>. However, structural studies found that cytochromes on these filaments are up to 40 nm apart<sup>91</sup>. Therefore, it has been proposed that diffusion of cytochromes along the filaments confer the conductivity to filaments<sup>91</sup>. A hopping model<sup>80</sup> has also been invoked for the electron transfer through monomeric cytochromes<sup>92</sup>. While we have demonstrated long-range hole hopping through closely stacked tyrosines, there are many ways for proteins to carry out charge transport, and more studies are needed to understand the varying mechanisms.

We expect that these results will motivate the synthesis of new peptides to test predictions of computational models. These findings can help to facilitate a bottom-up atomic-level approach to conductive protein design with structure-function correlation studies leveraging atomic-resolution structures of amyloid crystals. Our methodology will help to set standards for reporting protein conductivity for accurate comparison of different protein systems. In addition, the suggested critical role of the glutamine rotamer conformation is similar to the proton transfer mechanism proposed for the BLUF domain protein<sup>72</sup>. Therefore, the suggested transport mechanism may help address long-standing questions about how protein architecture influences electron transport<sup>32</sup> for a wide range

of applications which all employ aromatic residues and PCET, including artificial photosynthesis, biocatalysis, prevention of oxidative damage, and nucleic acid biosynthesis.

## **2.7 Materials and Methods**

### **2.7.1. Preparation of Peptide Microcrystals.**

Crystals **X1**<sup>48</sup>, **X2**<sup>48</sup>, and **X3**<sup>49</sup> were prepared as described previously. Microcrystal **X4** was prepared by purchasing KVQIINKKL synthetic peptide from GenScript. KVQIINKKL was crystallized using the hanging drop method with a 2:1 mixture of 20 mg/mL KVQIINKKL and 0.2 M Lithium Citrate, 20 % PEG 3350. All microcrystal hanging drop samples were diluted in their respective crystallization reservoir buffer for storage and subsequent single-crystal conductivity measurements.

### **2.7.2. Sample Preparation for Conductivity Measurements.**

Nanoelectrode devices were washed with acetone, isopropanol, ethanol and water twice then plasma cleaned for 2 minutes on a low setting (Harrick Plasma Cleaner, PDC-001-HP). All microcrystals were suspended in their respective reservoir buffer at varying dilutions. Appropriate dilutions of the original microcrystal stock solution (1:100) were made with either reservoir buffer or water and 3-4  $\mu$ L was dropped onto a clean device. Devices were first dried in a desiccator for ~25 minutes. Excess dried buffer was removed with filter paper. Samples were checked under the MPI probe station optics and if necessary, a microcrystal was moved onto the center of electrodes using a titanium probe needle. For all samples, the area of the device around the electrodes was cleaned with water and dried with filter paper to remove residual buffer. All samples were air dried overnight and mounted onto a metal puck for imaging by AFM in air (Oxford

Instruments Co, Cypher ES or Bruker Dimension Fastscan). All experiments were performed at atmospheric pressure in ambient air.

### **2.7.3. Direct Current (DC) Conductivity Measurements.**

Connections to device electrodes were made with a probe station (MPI TS50) inside a Dark Box. Current and voltage were applied using a semiconductor parameter analyzer with preamplifiers (Keithly 4200 A-SCS) allowing for 1 fA current and 0.5  $\mu$ V resolution. Two-probe DC conductance measurements utilized two probe needles to contact the device on two adjacent electrodes. A fixed voltage was applied to the two electrodes for a minimum of 200 s in sampling mode until a steady current was reached. Voltage-current points were fit with a line, and the slope was used to determine conductance (G). In four-probe DC measurements, contacts were made with 4 gold electrodes connected by a microcrystal. Current was applied to the outer two electrodes in the range of +/- 1-100 pA. The current was held for a minimum of 200 s, and the voltage difference at steady state was recorded from the two inner electrodes. The slope of the subsequent V-I curve was used to determine intrinsic sample resistance. For resistance versus length measurements, the setup started in the four-probe setup; the last two probes were moved over by one electrode such that the four probes spanned 5 electrodes. The resistance was measured, and the last two probes were again moved by one electrode. This process was repeated three times to reach 350 nm. For measuring conductivity using both two- and four-probe measurements, linearity of current and voltage was maintained by applying appropriate voltage and current respectively.

#### 2.7.4. Impedance Spectroscopy (IS)

IS was performed at ambient room temperature and humidity. For all experiments, humidity was continuously monitored and maintained at less than 50%. The probe station connections and sample prep were identical to those for two-probe measurements. The two probe needle cables were connected to working and sense and counter and reference electrodes respectfully on a Gamry Interface1000. An AC voltage of amplitude 100 mV was applied in Potentiostatic mode sweeping from 100,000 to 0.2 Hz. Equivalent circuit modeling was performed with Echem Analyst Software, and all data was fit to a resistor and constant phase element in parallel.

#### 2.7.5. Temperature Dependent DC Conductivity Measurements.

The sample was placed in a cryostat (Quantum Design DynaCool PPMS), and conductivity was measured using the Keithly 4200 A-SCS. Both two and four-probe DC measurements were performed at each temperature once the temperature reached an equilibrium. Activation energy was calculated by an Arrhenius fit to the natural logarithm of conductivity versus the inverse temperature.

#### 2.7.6. Conductivity Calculations.

Conductivity of the microcrystals was calculated by using the conformal mapping

technique:  $\sigma = \frac{-\pi G}{L} * \ln \left( \frac{1 - \tanh \frac{\pi a}{2g}}{4 \tanh \frac{\pi b}{2g}} \right)^{-1}$  where  $G$  is the conductance (S),  $a$  is half the

separation of electrodes (150 nm),  $b$  is the width of the electrode plus  $a$  (450 nm),  $L$  is the length of the microcrystal in contact with the electrode, and  $g$  is the height of the microcrystal<sup>38</sup>. In our case  $g=L$  because the microcrystals are very regular in shape. A table of all crystal conductivities, average resistance, and average heights can be found in SI Table 10. Conductivity of a blank device was calculated using the formula  $\sigma = KG$

where  $K$  is the cell constant calculated to be  $K=50630 \text{ m}^{-1}$  for  $n=2$  electrodes of length 30  $\mu\text{m}$ , width 300 nm and gap size 300 nm<sup>93</sup>. The conductivity value for resistance versus length was calculated by using the linear fit at 300 nm to get a resistance value and then using the equation above. Flux at 0.1 V was calculated by assuming all tyrosines within the crystal are active carriers and that transport occurs only along the crystal's long axis. Additionally, I assumed every charge transport path is independent of one another and thus adds linearly to the flux. The height of the crystal was 200 nm. Assuming a square cross-sectional area and 0.5 active Tyr per nm<sup>2</sup> (from the structure), I calculated the flux per path of stacked tyrosines (Figure 2.6B). Length was converted to number of hopping steps by dividing the distance by edge-to-edge separation of Tyr (3.5 Å). Contact resistance in Figure 2.7 was calculated as the difference between the two and four probe resistances at each temperature of two separate crystals.

### **2.7.7. Acknowledgments**

We thank Sharon Hammes-Schiffer, Eric Martz and Matthew Guberman-Pfeffer for helpful discussions. Computational work was supported by the Air Force Office of Scientific Research Grant FA9550-17-0198 (V.S.B) and high-performance computing time from NERSC and from the high-performance computing facilities at Yale. This research was supported by the Career Award at the Scientific Interfaces from Burroughs Wellcome Fund (to N.S.M.), the National Institutes of Health Director's New Innovator award (1DP2AI138259-01 to N.S.M.), the NSF CAREER award no. 1749662 (to N.S.M.). Research was sponsored by the Defense Advanced Research Project Agency (DARPA) Army Research Office (ARO) and was accomplished under Cooperative Agreement Number W911NF-18-2-0100 (with N.S.M. and V. S. B). This research was

supported by NDSEG Graduate Research Fellowship award (to C.S.). Research in the Malvankar laboratory is also supported by the Charles H. Hood Foundation Child Health Research Award, and The Hartwell Foundation Individual Biomedical Research Award.

## **2.8 Supplementary Information**

Any supplemental information not performed directly by this author was excluded and can be found in the SI to the published work at this location:

<https://doi.org/10.1073/pnas.2014139118>

### 3. OmcS as a physiological nanowire

#### *Redox Regulation and Re-Engineering in a Multiheme Cytochrome Nanowire*

Matthew J. Guberman-Pfeffer\*, Catharine Shipps\*, Pilar C. Portela, Vishok Srikanth, Jens Neu, Carlos A. Salgueiro, Nikhil S. Malvankar

#### 3.1 Author Contributions

C.C.S., N.S.M., and C.A.S. designed experiments, P.C.P. and C.C.S. purified protein samples. C.C.S. performed electrochemistry experiments on nanowires, M.G.P. performed computational analyses, V.S. produced TEM images, J.N. fabricated electrodes.

#### 3.2 Summary

The role of OmcS in EET has been under reinvestigation since the discovery that it forms cytochrome nanowires. OmcS is essential for growth on Fe(III) oxides and its transcripts are upregulated under a variety of other growth conditions for *Geobacter sulfurreducens*. Although genetic studies suggested that OmcS plays a terminal role in EET, the underlying biophysical mechanism is unclear due to the far-negative redox potential (-0.212 V) reported for OmcS, measured under non-physiological conditions. I find through spectroelectrochemistry that the macroscopic midpoint potential of the OmcS nanowire is physiologically relevant at -0.130 to -0.176 V range. Electrochemistry of nanowire films by differential pulse and cyclic voltammetry agreed well with solution state spectroelectrochemistry. The microscopic potentials derived from spectroelectrochemistry are quantitatively reproduced by quantum mechanical/molecular mechanical computations, permitting an assignment of the spectroelectrochemical data to specific hemes in the cryoEM structure. The resulting redox landscape along a subunit of the nanowire follows an overall nearly thermoneutral pattern, consistent with the

negligible decay in electron energy over micrometers observed in experiments These results help to establish OmcS's role in EET as a protein that can favorably accept electrons from the periplasm while simultaneously being the terminal electron donor and can enable the rational design of mutants to increase conductivity or cellular function.

### 3.3 Introduction

*Geobacter sulfurreducens* (*G.s.*) uses direct extracellular electron transfer (EET) to transport electrons generated by the TCA cycle through the inner and outer membrane to external electron acceptors including metal oxides by direct contact<sup>14</sup>. The electron acceptors in soil are diverse and bacteria that utilize them likely have a multitude of metabolic pathways and feedback mechanisms to survive<sup>94</sup>. *G.s.* has a putative 111 cytochromes based on recognition of heme binding sites<sup>11</sup>. Of these, several outer membrane cytochromes have been shown to be important for growth on insoluble Fe(III) oxide including OmcS<sup>23</sup>, OmcB<sup>95</sup>, and OmcE<sup>23</sup> because knockouts of the genes show poor or absent Fe(III) oxide reduction. There are many additional genes for which transcription is upregulated when grown on Fe(III) oxide, but the highest upregulated gene is *omcS* and its co-transcribed homologue *omcT*<sup>96</sup>. In addition to growth on Fe(III) oxide, *omcS* was found to be upregulated in an adapted strain grown on Fe(III) citrate in the absence of OmcB<sup>97</sup>. OmcS is also essential for syntrophic growth with *Geobacter metallireducens*<sup>98</sup>.

Since OmcS is one of the most abundant proteins in outer surface preparations and was shown to be important for a variety of growth conditions, multiple studies focused on determining OmcS's direct role in EET<sup>23</sup>. Two previous studies have largely solidified the current model for OmcS in EET<sup>14</sup>. First, a localization study found that OmcS

antibodies decorated extracellular filaments, presumed to be comprised of PilA-N, on WT cells grown on Fe(III) oxide<sup>99</sup>. Concurrently, the redox potential of OmcS was reported to be -212 mV vs SHE with a 320 mV redox active range and experiments confirming that OmcS can donate electrons to a variety of terminal electron acceptors<sup>100</sup>. These studies together seemed to solidify OmcS's role as the final step in EET. The mechanism of electron transfer to OmcS was still under study but it was thought that electrons would travel from periplasmic cytochromes through e-pili, or through trans-outer-membrane porin cytochrome complexes<sup>101</sup>, to OmcS then to terminal electron acceptors<sup>99</sup>. With the recent discovery that OmcS polymerizes into cytochrome nanowires, along with OmcE and OmcZ, the model for EET must be reevaluated to probe the role of cytochrome nanowires<sup>18, 19, 21</sup>.

The collection of extracellular structures on *G.s.* is growing more complex than previously realized. Filaments of multiple outer surface cytochromes, PilA-N/C, and DNA have morphologies that are challenging to consistently, accurately distinguish in routine images from AFM, TEM, and even Cryo-EM micrographs<sup>21</sup>. Thus, we need to reinterpret previous work with caution especially when viewing images of nanowires. The simplest reinterpretation of the localization of OmcS antibodies on filaments, based on structural analysis, is that those filaments were OmcS filaments as no biochemical evidence was given in that study to show otherwise<sup>99</sup>.

The OmcS's redox potential was measured before the discovery that OmcS formed nanowires on bacterial surface<sup>18</sup>. As a result, the study subjected OmcS preparations to boiling in an aqueous solution of the denaturant sodium dodecyl sulfate which may have

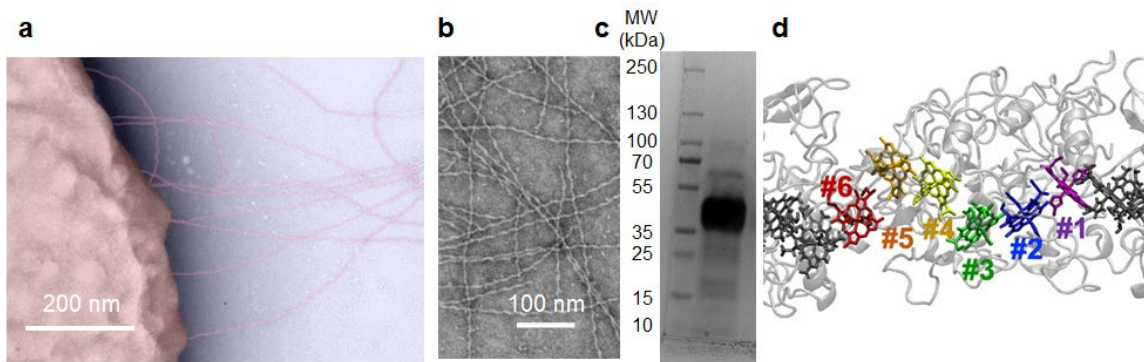


**Figure 3.1: Strategy to determine role of OmcS in EET**

**a**, TEM Image of OmcS nanowires attached to a  $\Delta OmcZ$  cell. **b**, TEM image of the purified nanowire sample. **c**, Heme stain of purified nanowire sample and **d**, Trimer model used throughout the study from structure of OmcS (PDB 6EF8).

broken the filaments leaving the hemes more solvent exposed. The greater polarity of an aqueous environment compared to the protein could stabilize the oxidized state of the heme cofactor, thereby making the redox potential more negative. Consistent with this hypothesis, microperoxidases which are prototypical systems for fully solvent-exposed hemes with bis-histidine ligation, exhibit macroscopic midpoint potentials in the -0.190 to -0.220 V range<sup>102-104</sup>. Common periplasmic cytochromes typically have more positive redox potentials. Since OmcS was reported to be more negative than common periplasmic cytochrome PpcA and family<sup>14</sup>, and it was previously reported that its location was outside the periplasm due to immunogold labeling<sup>99</sup> it was deduced that it played no role in periplasmic electron transfer.

Extracellular OmcS is still likely to be one of several terminal steps in EET but the procession of electrons to nanowires is still not understood<sup>14</sup>. Understanding the redox potential of intact OmcS nanowires, and the individual hemes in OmcS, will help reevaluate their role in EET, especially within the periplasm, and enable rational design for mutants to tune nanowire conductivity and possibly alter the range of terminal electron acceptors available to the cell.

Herein, I perform the first measurements of redox potential for intact OmcS nanowires. We compare and quantitatively reproduce experimental estimates for the six heme redox potentials in OmcS. Finally, I analyze surface potentials of OmcS and periplasmic cytochromes to determine possible interaction sites and propose a new model for EET involving nanowires.

### **3.4 Results**

#### **3.4.1. Redox characterization of OmcS nanowires reveals more positive midpoint potential**

To investigate the redox potential of native OmcS nanowires, I purified them from *ΔomcZ* cells grown under fumarate conditions in combination with size exclusion chromatography to specifically purify OmcS nanowires (see Methods) (Figure 3.1a-c). I used spectroelectrochemistry (SEC) to determine the redox potential of nanowires in solution at pH 7<sup>105</sup>. Spectroelectrochemistry is a sensitive electrochemistry technique that allows you to measure the redox potential of your protein in solution without the need to subtract background current or modify electrodes as in other voltammetry techniques. I found the midpoint to be  $-129 \pm 13$  mV vs SHE which is 80 mV more positive than the previously reported potential (Figure 3.2c). There was some hysteresis observed with the anodic trace being on average more positive than the cathodic by 17 mV. The hysteresis might indicate some changes in protein structure accompanied with the redox transition<sup>106</sup> or it could be from the large macroscopic nature of the nanowires or aggregation which might influence reaction kinetics at the electrode surface. The active range for OmcS was on average between -0.31 to 0.05 V for a total range of 360 mV which is similar to the previously reported range for OmcS<sup>100</sup>. Additional measurements

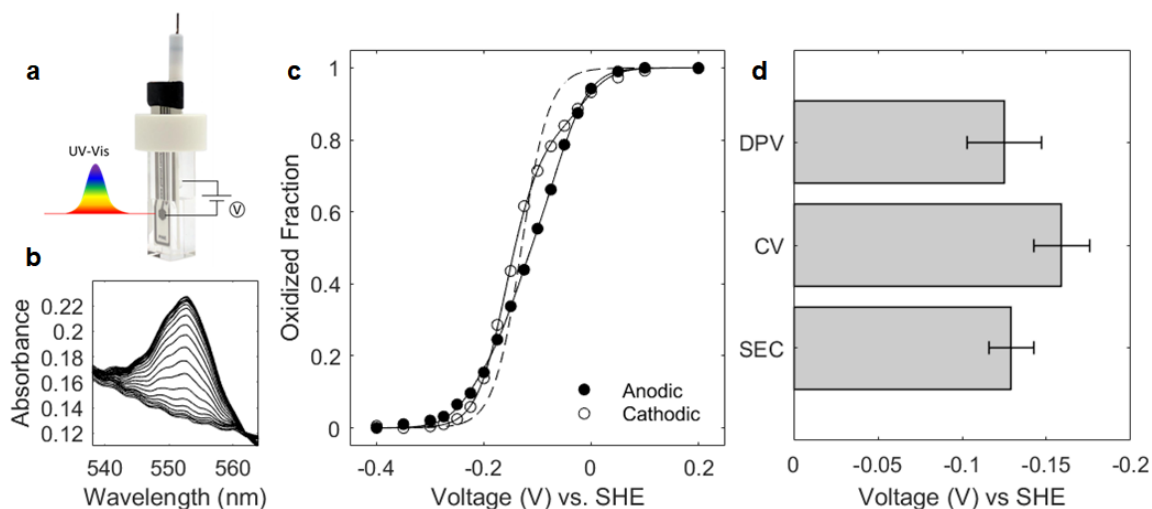


**Figure 3.2: OmcS has more positive redox potentials than previously reported.**

**a**, Modified schematic of spectroelectrochemistry setup from Pine Research Honeycomb Spectroelectrochemical Cell User Guide (see methods). **b**, The alpha peak in the Q-band region of OmcS nanowires shown as it changes from oxidized to reduced as a representative image. **c**, Oxidized fraction of OmcS nanowires shown versus applied potential calculated from the area of the alpha peak in **(b)**. Anodic (filled circles) and cathodic (open circles) traces are shown in addition to a six-heme independent Nernstian with hemes fitted individually (solid lines) or with all hemes having a potential of -130 mV vs SHE (dashed line) **d**, Comparison of solid-state measurements by cyclic voltammetry (CV) and differential pulse voltammetry (DPV) of OmcS redox potential to spectroelectrochemistry (SEC).

of nanowire films in solid state with differential pulse voltammetry (DPV) and cyclic voltammetry (CV) were consistent with spectroelectrochemistry results (Figure 3.2d).

The more negative results from CV could be due to irreversible dynamics of the system (shown by hysteresis) or the fact that CV is less sensitive than SEC or DPV<sup>107</sup>.

### 3.4.2. Macroscopic Reduction Potentials

With a better understanding of the experimental redox potential of OmcS we can explore the ways to tune its electrical properties and interactions with other proteins by modulating the individual heme potentials. Fully determining individual heme redox potentials on a multiheme cytochrome requires a combination of redox titration measurements with complex NMR measurements. To include the possibilities of heme interactions and redox-Bohr effects, individual hemes signals need to be monitored by NMR at different pH values and oxidations states<sup>108, 109</sup>. Nanowires are challenging to

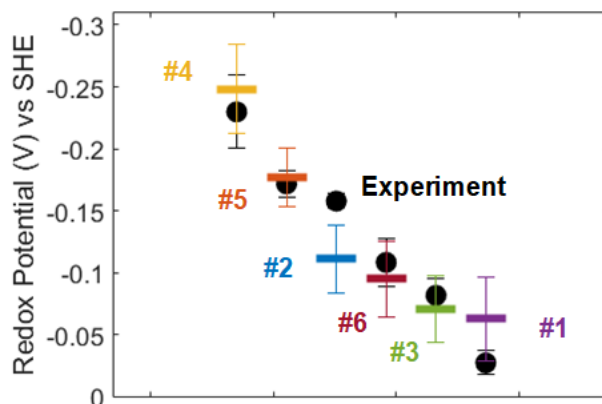


**Figure 3.3: Computational calculations of heme redox potential agree with experimental microscopic potentials.**

The final calculated heme potentials compared to the six independent Nernstian-fit experiment values with their errors indicated and heme numbers shown for computational values. All values with error bars are mean  $\pm$  SEM.

purify, and as of yet there is no way to monitor them by NMR, so for simplicity here I just report the results of fitting spectroelectrochemical experiments compared to computational modeling as a secondary input.

Spectroelectrochemical data can be fit with either independent or sequential redox centers, where the sequential model implies interaction between hemes and the independent model does not<sup>110</sup> (Equation 3.1-3.5). I tested fitting the experimental data (Figure 3.2c) with both six independent and six sequential Nernstian centers which yielded similar results (Figure 3.3). The close agreement suggests that the heme-heme interactions were presumably small compared to the uncertainties in the reported

**Table 3.1: Macroscopic potential comparison between experiments and computations**

All Values in volts (V) vs SHE. Error as standard error of the mean (SEM)

| Sequential | SEM   | Independent | SEM   | Heme # | Computed | SEM   |
|------------|-------|-------------|-------|--------|----------|-------|
| -0.240     | 0.024 | -0.230      | 0.030 | 1      | -0.063   | 0.034 |
| -0.184     | 0.009 | -0.172      | 0.011 | 2      | -0.111   | 0.027 |
| -0.151     | 0.005 | -0.158      | 0.006 | 3      | -0.071   | 0.027 |
| -0.106     | 0.011 | -0.108      | 0.019 | 4      | -0.248   | 0.036 |
| -0.075     | 0.010 | -0.082      | 0.013 | 5      | -0.177   | 0.024 |
| -0.021     | 0.008 | -0.027      | 0.010 | 6      | -0.095   | 0.031 |

potentials. I thus used the independent model values to limit assumptions about the system.

Calculations for heme redox potentials were carried out on a trimer model of OmcS (Figure 3.1c) by my coauthor to include heme distortions and full electrostatic solvation using QM/MM methods. These calculations agreed well with experimental values (Figure 3.3). The close agreement between calculations and experiment can be leveraged for rational design and re-engineering the redox-based conductivity of this biological nanowire. Work is underway to elucidate the controlling factors that sculpt the redox landscape at an atomistic level. The resulting redox landscape across a subunit of the

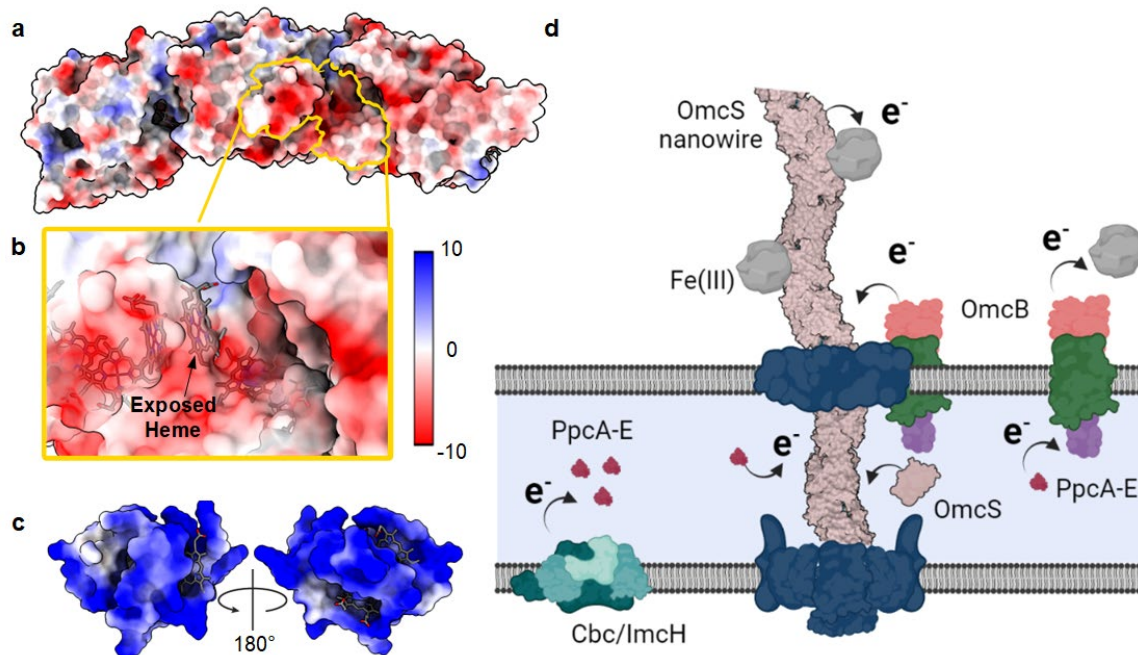


**Figure 3.4: Revised model of extracellular electron transfer with OmcS**

**a**, Surface potential of OmcS filament highlighting the regions of negative potential in various places including pockets between protomers that have exposed hemes (yellow outlined region). **b**, Zoom-in image of the yellow outlined region in **(a)** showing the exposed heme surrounded by a negative surface potential. **c**, Surface potential of PpcA showing mostly positive charge including in areas around the exposed hemes. Surface potential in **(a-c)** is shown using the color bar in **(b)** with units of kcal/e•mol. **d**, Model of extracellular electron transfer where PpcA receives electrons from the inner membrane complex and donates them to OmcS nanowires which then transport electrons outside the cell due to the potential difference between the cell and surrounding environment. The OmcB complex could also be involved in transporting electrons to the nanowire. Panel **d** generated in Biorender.

nanowire follows an overall nearly thermoneutral pattern, consistent with the negligible decay in electron energy over micrometers observed in experiments<sup>111</sup>.

### **3.4.3. Surface potentials of OmcS and PpcA are compatible**

To understand the possibility of electron transfer between OmcS and PpcA I look to their surface potentials. OmcS has a variety of surface potentials while PpcA is primarily positive (Figure 3.4a-c). One area of possible interaction could be near an exposed heme on OmcS surrounded by an area of negative potential (Figure 3.4b). The contrasting surface potential of the two proteins in this region combined with relative heme exposure could create an opportunity for electron transfer between the two proteins. Detailed interaction studies would be needed to confirm this hypothesis.

## **3.5 Discussion**

### **3.5.1. Proposed model for periplasmic electron transfer to OmcS**

The mechanism of electron transfer would depend on how OmcS nanowires are assembled, and if they are accessible in the periplasm. With our data and considerations, I present the model that PpcA could diffusively exchange electrons with exposed OmcS nanowires in the periplasm facilitating extracellular electron transport (Figure 3.4d). This model for EET does not exclude respiratory electrons from passing through other pathways which are known to be important such as the OmbB/OmaB/OmcB complex which is pictured<sup>14</sup>, or other porin cytochrome complexes such as ExtABCD, ExtEFG, OmbC/OmaC/OmcC<sup>112</sup>. While it would require future study, it is also possible that OmcB can transfer electrons to nearby OmcS nanowires<sup>14</sup>. This model emphasizes that given the more positive midpoint potential of OmcS nanowires, they could be involved in periplasmic electron exchange. Collaborators are currently investigating electron transfer

between PpcA and OmcS nanowires by NMR. These results will tell us if electron transfer is possible between the two proteins.

### **3.6 Materials & Methods**

#### **3.6.1. Purification of OmcS**

*ΔOmcZ* cells were grown in 10 L jugs at 25 C to OD ~0.8-1 in NBAF media with 10xMgSO<sub>4</sub> compared to typical growth and without reazurin<sup>113</sup>. Cells were collected at ~15,000 g for 12 minutes. Pellets were resuspended in 150 mM ethanolamine pH 10.5 and homogenized with a tissue grinder then left to stir at 4 C overnight. Cells were then blended on low speed for 2 minutes and cell debris was pelleted by spinning at 10,000 g for 30 minutes. Supernatant was homogenized by stirring overnight with 1 ml 12.5% Triton X-100 per 250 ml supernatant. The solution was then dialyzed to 20 mM triethanolamine pH 8 exhaustively using 50 kDa cutoff membrane. Nanowires were pelleted by spinning solution at 23,000 g for 1 hour. Pellets were resuspended in 20mM ethanolamine pH 10.5 and left on a rotary shaker overnight. Any insoluble material left was removed by centrifugation at 10,000 g for 30 minutes. This process was repeated as desired if sample had an excess of undesired proteins at this stage. Sample was run through gel filtration column Sephacryl S-500 HR and fractions were pooled to contain purified nanowires.

#### **3.6.2. TEM Imaging**

Electron microscopy Sciences grids (mesh size 400) were plasma cleaned for 30 s in PDC-001-HP Harrick Plasma cleaner. 5 μl of sample (nanowires or cell culture) was dropped onto carbon face of grid and let stand for 10 minutes. Excess solution was blotted. Samples were placed face down on 50 μL drops of negative stain (1%

phosphotungstic acid, pH 6) for 30 seconds, remaining solution was removed by blotting, then repeated once more. Grids were air-dried and stored in a sealed case until imaging using JEM-1400Plus microscope operating at 80 kV (JEOL).

### **3.6.3. Electrostatic Potential Visualization**

The electrostatic potential was generated on OmcS (PDB: 6EF8) and PpcA (2MZ9) using ChimeraX software<sup>132</sup>.

### **3.6.4. Electrochemistry**

Platinum wire with 0.5 mm diameter served as the counter electrode while an Electrolytica C-925 1mm (Ag/AgCl with 3.4 M KCl) served as the reference electrode. The reference was compared to a standard before each use. The counter electrode was cut fresh or cleaned in 0.5 M H<sub>2</sub>SO<sub>4</sub> as the gold electrodes before use by holding 2.04 V for 5s, -0.31 V for 10 s, followed by cyclic voltammetry from -0.26 V to 1.6 V at 4000 mV/s for 20 cycles then at 100 mV/s for 4 cycles<sup>114</sup>. Electrodes were then washed in ethanol then water and dried in stream of N<sub>2</sub>. 1.5 μL of filament solution was drop cast onto the device and air dried overnight before measurement. Cyclic Voltammetry (CV) and Differential Pulse Voltammetry (DPV) were performed using Gamry potentiostats. For all biofilms, CV was performed from 0.4 to -0.7 with step size of 1 mV at a scan rate of 5mV/s unless otherwise indicated. All DPV was performed from 0.4 to -0.7 with a step size of 1 mV, sample period of 0.5 s, pulse size of 25 mV and pulse time of 0.1 s. The electrolyte in all cases was 50 mM KH<sub>2</sub>PO<sub>4</sub> and 100 mM KCl at pH 7 sparged with N<sub>2</sub> for at least 30 mins and stored in a serum tube to remain anaerobic<sup>113</sup>. Peak fitting was performed using MATLAB scripts including the EzyFit<sup>115</sup> and peakfit<sup>116</sup> modules.

### 3.6.5. Spectroelectrochemistry

Spectroelectrochemistry experiments were performed in Pine Research Honeycomb Spectroelectrochemical Cell according to the user guide<sup>105</sup>. Briefly, 1 ml of purified OmcS was concentrated through a 30 kDa cutoff Amicon centrifugation column at 14,000 g for 5 mins. 400  $\mu$ l electrolyte solution (50 mM  $\text{KH}_2\text{PO}_4$  and 100 mM KCl at pH 7) was added to the column and any pelleted nanowires were resuspended. This process was repeated 3X. A final spin at 17,000 g was used to pellet nanowires into an Eppendorf tube. Any excess buffer was pipetted off leaving a pellet of nanowires. The tube was put into an anaerobic chamber with the cap open so ambient oxygen was removed by transferring purge process. The pellet was resuspended in 200-400  $\mu$ l of electrolyte until homogenous. The concentration of OmcS was measured by absorbance at the 528 nm peak<sup>100</sup> and was between 30-60  $\mu$ M for all trials. A solution of equal concentrations of 15 mediators that span a potential range from -440 to +80 mV vs SHE was added to a final concentration of 1-2 % of the heme concentration in the sample<sup>100</sup>. Additional investigation shows that higher [Mediator]/[Hemes] percentage resulted in distortion of the alpha peak and background subtraction could not consistently correct the issue (SI Figure 3.1). Subsequent potential steps were applied to the sample for 2 minutes and simultaneous UV-Vis spectra were recorded. Samples were scanned in the cathodic then anodic direction and the cuvette solution was mixed in between runs.

#### *Data processing*

Spectra were recorded continuously throughout the measurements and the time signatures of the applied potentials and spectra were synched to process only the spectra recorded at the end of the 2-minute window. Isosbestic points were calculated by finding

the points with lowest standard deviation across the collected spectra in the expected range (540-565 nm). The area under the alpha peak above the line between isosbestic points was used to calculate the oxidized fraction. Midpoint was determined by fitting a single Nernst equation to the data (Equation 3.1). Individual macroscopic potentials were fit with either independent or sequential six-centered Nernst equations (Equation 3.2-3.5)<sup>110</sup>.

$$P_{ox}(x) = \frac{e^{(x-v_1)k}}{(1 + e^{(x-v_1)k})} \quad 3.1$$

$$P_{ox}(x) = \frac{1}{6} \sum_{i=1}^6 \frac{e^{(x-v_i)\frac{F}{RT}}}{(1 + e^{(x-v_i)\frac{F}{RT}})} \quad 3.2$$

$$p_r = 6 + 5e^{(x-v_1)\frac{F}{RT}} + 4e^{(2x-v_1-v_2)\frac{F}{RT}} + 3e^{(3x-v_1-v_2-v_3)\frac{F}{RT}} \dots \quad 3.3$$

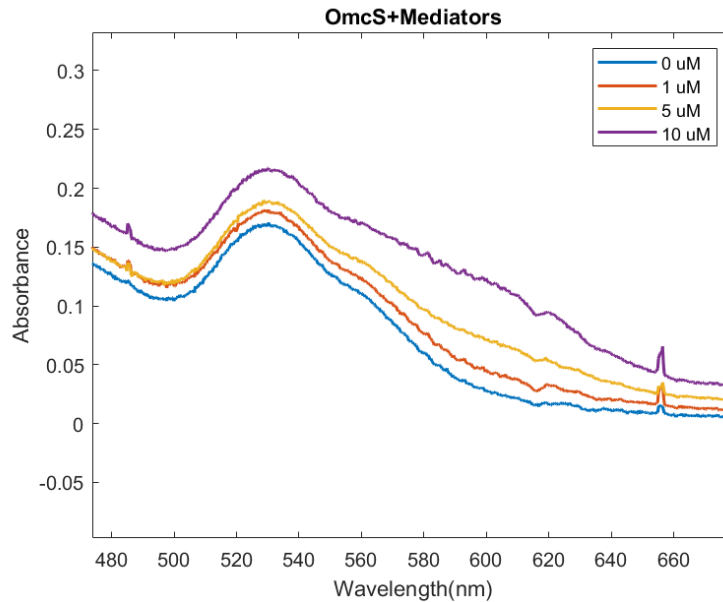
$$+ 2e^{(4x-v_1-v_2-v_3-v_4)\frac{F}{RT}} + e^{(5x-v_1-v_2-v_3-v_4-v_5)\frac{F}{RT}}$$

$$Z = 6(1 + e^{(x-v_i)k} + e^{(2x-v_1-v_2)\frac{F}{RT}} + e^{(3x-v_1-v_2-v_3)\frac{F}{RT}} + e^{(4x-v_1-v_2-v_3-v_4)\frac{F}{RT}} \dots \quad 3.4$$

$$+ e^{(4x-v_1-v_2-v_3-v_4)\frac{F}{RT}} + e^{(5x-v_1-v_2-v_3-v_4-v_5)\frac{F}{RT}} + e^{(6x-v_1-v_2-v_3-v_4-v_5-v_6)\frac{F}{RT}}$$

$$P_{ox}(x) = 1 - \left(\frac{p_r}{Z}\right) \quad 3.5$$

### 3.7 Supplement



**SI Figure 3.1: OmcS and mediator interference is concentration dependent.**

The absorbance of purified oxidized OmcS nanowires at concentration  $37\mu\text{M}$  with the indicated concentration of mediators representing at 0, 0.5, 2.5, and 5 % ratio of mediators to hemes in the sample. The mediators spectra is most strong around 600 when oxidized. The spectrum around the alpha band remains undistorted for percentages less than 2.5 %. Thus we chose a mediator ratio in 1-2 % to avoid the signal interference.

## **4. Nanowires in mutant biofilms: a look at what OmcS and OmcZ do for EET**

*Tunable redox profile and conductivity of biofilms via cytochrome nanowires*

Catharine Shipps, Cong Shen, Zion Perry, Aldo I. Salazar Morales, Jens Neu, Nikhil S. Malvankar

### **4.1 Author Contributions**

C.C.S. and N.S.M. designed experiments, C.C.S. and C.S. performed electrochemistry on biofilms, C.C.S. and Z.P. performed electrochemistry on nanowires, C.C.S. performed conductance measurements, biochemical analyses, and analyzed all data. A.S.M. provided strains and TEM imaging. J.N. fabricated electrodes.

### **4.2 Summary**

Cytochromes OmcS and OmcZ have been found to be of critical importance to *Geobacter sulfurreducens* respiration processes over the years. Recently the discovery that both proteins form micrometer long nanowires *in vivo* has prompted an investigation into how each nanowire contributes to cellular metabolic processes. It is known that OmcS is important for growth on solid electron acceptors, and it is known that OmcZ is critical for high current production. However, all previous work investigating the redox properties of these two cytochromes has been on monomeric samples. Here I determine the redox properties of purified OmcZ nanowires. I also investigate how differential expression of nanowires over time controls biofilm conductivity and redox potential in strains of wild type,  $\Delta omcS$ , and  $\Delta omcZ$ . I find that OmcZ nanowires have multiple redox peaks that range from -70 to -281 mV which indicates unique heme grouping in OmcZ. I find that knockout strains produce continually increasing amounts of extracellular protein

and that OmcS and OmcZ abundance increases over time. I find that wild type reaches a plateau very early on for both proteins' expression. I find that electrochemical gating of wild type and  $\Delta$ OmcS matches the gating of OmcZ nanowires very well and confirm that OmcZ has greater than 400-fold conductance compared to OmcS. Understanding how the nanowires' and biofilms' redox behavior overlaps will help us not only understand *G.s.* metabolism but help us tune the performance of biofilms for use in energy harvesting and as chemically tuned biological switches.

### 4.3 Introduction

The criticality of OmcS and OmcZ to extracellular electron transport (EET) in various conditions has been extensively demonstrated<sup>117</sup>, but with the recent discovery that the two proteins form distinct nanowires we must reevaluate their roles in the EET pathway<sup>18, 19, 22</sup>. In early studies of biofilms, OmcZ was found to be essential for high current production as metabolic current remained low and resulting biofilms were thin in an OmcZ knockout<sup>24</sup>. OmcZ was found to be highly concentrated near anodes in biofilms where the metabolic activity of cells is highest, and less concentrated in biofilm layers away from the electrode where cells show lower activity<sup>118, 119</sup>.

Recent studies created strains that overexpressed proteins critical for biofilm growth including OmcS and OmcZ found increases in current density, biofilm conductance, and biofilm thickness<sup>120</sup>. Other studies that looked at strains where OmcS or OmcZ nanowires were omitted but flagella were introduced looked to study how nanowires effected the structural components of biofilms<sup>121</sup>. They found that OmcZ was critical to both while lack of OmcS made biofilms more resistive but did not affect biofilm heights<sup>121</sup>.

Electrochemical studies of mutant biofilms show differentiation in redox profiles due to mutations<sup>120, 122</sup>. The potentials of biofilms are complex but the final steps in EET to the anode should be visible in voltammetric studies. In order to compare redox profiles of OmcS and OmcZ to these biofilm studies we need accurate redox profiles of nanowires as previous studies were performed on SDS-boiled monomers<sup>100, 106</sup>. Another challenge of many biofilm studies is that protein abundance is often analyzed or inferred from whole cell lysates or transcriptional data which may not accurately show the extracellular abundance of nanowire proteins.

Here I use simultaneous electrochemical and biochemical analysis on identical biofilms and new redox measurements on purified OmcZ nanowires to compare extracellular cytochrome filament OmcS and OmcZ composition to biofilm phenotypes in WT,  $\Delta omcS$ , and  $\Delta omcZ$  biofilms. I find that the  $\Delta omcS$  strain lacks OmcZ nanowires at early growth stages and overproduces them over time which correlates with the increase in metabolic current and across-biofilm conductivity. The  $\Delta omcZ$  cells overproduce OmcS significantly outside the cell but show no increase in current and maintain low conductance underscoring the critical role for OmcZ in biofilm performance. Electrochemical signatures from  $\Delta omcS$  biofilms agree very well with purified OmcZ nanowires, while WT has additional negative signatures not accounted for by OmcZ nanowires.

#### **4.4 Results**

I investigated biofilms of three strains of *Geobacter sulfurreducens*: WT,  $\Delta omcS$ , and  $\Delta omcZ$ . All strains were monitored over time in microbial fuel cells operating in constant flow-through mode. Figure 4.1a shows the schematic for simultaneous

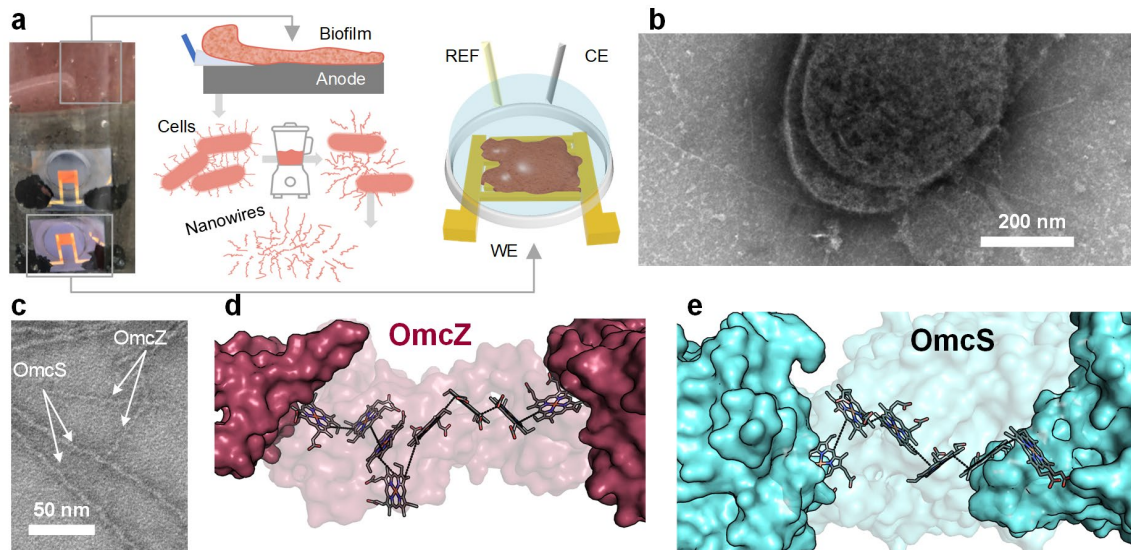


**Figure 4.1: Strategy to investigate nanowire expression and conductivity, redox profile simultaneously.**

**a.** (*left*) Image of biofilm grown on a graphite electrode (red substance) with interdigitated gold electrodes for concurrent biochemical and biophysical analysis of biofilms. (*center*) Biochemical analysis of extracellular nanowire production by scraping biofilm from electrodes, shearing nanowires, and collecting them via salt precipitation. (*right*) schematic of electrochemical measurements with counter (CE), reference (REF), and working electrodes (WE) shown of biofilm in solution taken directly from the electrode. Conductance measurements performed similarly without counter and reference submerged using the two gold contacts shown. **b.** Image of  $\Delta omcS$  cell with nanowires protruding from surface. **c.** Close up TEM image of OmcS and OmcZ nanowires. **d.** OmcZ nanowire structure showing the close spacing of hemes and thinner nanowire than in **e**, OmcS nanowire.

biochemical and electrophysical analysis on grown biofilms that focus on analysis of cytochrome nanowire expression. When the fuel cell is disconnected at a certain time point, the biofilm is collected and nanowires are extracted using previously established methods<sup>19</sup>. I chose to do nanowire purifications rather than whole cell lysates because I specifically wanted to look at extracellular nanowire composition rather than unpolymerized monomers of OmcS and OmcZ. I attached interdigitated microelectrode arrays to graphite electrodes to collect enough biofilm for nanowire purification and have the same biofilm grown on electrodes for electrochemistry and conductance measurements. The devices were removed from the graphite block to be measured in our electrochemical setup (Figure 4.1a, right). A representative TEM image of cell from a  $\Delta omcS$  biofilm shows nanowires protruding from its surface (Figure 4.1b). Comparisons

of the OmcZ and OmcS nanowires in TEM reveal morphological differences which reflect their structures (Figure 4.1c-e). OmcZ is thinner than OmcS and the hemes in OmcZ are more closely packed than in OmcS (Figure 4.1d-e)<sup>22</sup>. OmcZ also has a heme that breaks from the center heme chain and is solvent-exposed. These structural differences could account for the different physiological roles of the two nanowires discussed above.

#### 4.4.1. Extracellular OmcZ nanowires stimulate biofilm metabolic current and conductivity

Figure 4.2 shows analysis of all three strains of biofilms over time. The metabolic current of all three strains varied with WT reaching maximum current quickly whereas the  $\Delta omcS$  strain exhibited a lag in current production, and  $\Delta omcZ$  did not produce much current at all (Figure 4.2a). These results were consistent with previous findings on strains with critical cytochrome knockouts<sup>22, 122</sup>. The metabolic current at harvesting is summarized in Figure 4.2b showing WT was relatively consistent over the examined time while  $\Delta omcS$  showed an increase over time and  $\Delta omcZ$  produced very little current

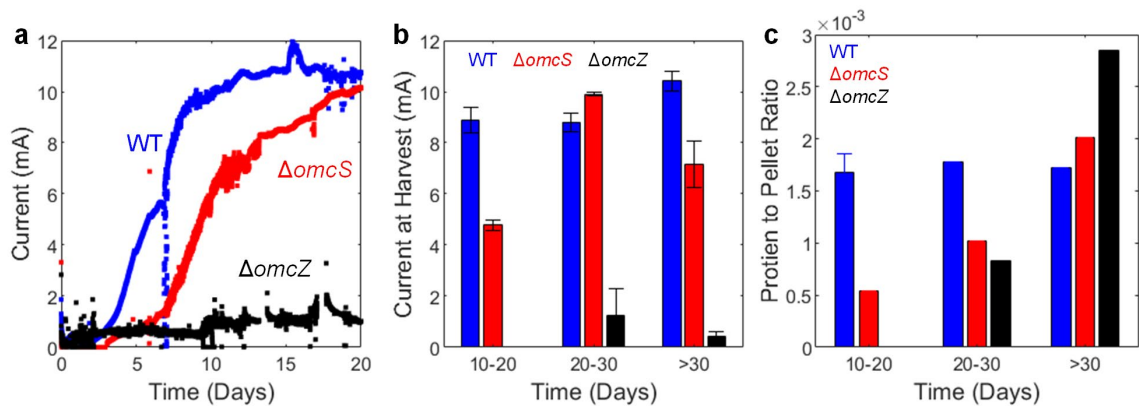


**Figure 4.2: Nanowire-deficient mutants have more protein in filament preparations over time.**  
**a,** A representative metabolic current from the biofilms over time. **b,** The metabolic current at the point the fuel cells were taken down for conductance analysis. **c,** Quantification by Bradford colorimetric assay of protein mass from nanowire preparations of harvested fuel cells divided by the cell pellet mass of the collected biofilm. Errors shown are standard deviation. The color code is blue:WT, red: $\Delta omcS$ , black: $\Delta omcZ$ .

compared to the other two. This immediately confirms the importance of OmcZ for current production of biofilms, as summarized by other studies<sup>120-122</sup>. Extracellular filament preparations were harvested as described previously<sup>19</sup>. The total amount of protein collected in the filament preparation (mg) divided by the total cell pellet collected (mg) was measured and shown to increase over time for the mutants but remain relatively constant for the WT strain (Figure 4.2c, SI Figure 4.2). The lag in protein production in  $\Delta omcS$  correlates with the lag in current production for  $\Delta omcS$  fuel cells. However, this is not the case for  $\Delta omcZ$  cells which failed to produce large current even at later time points (Figure 4.2a). Even though the protein-to-pellet ratio increases over time, the ratio in  $\Delta omcS$  does not match WT until the final time point even though metabolic current catches up around 20 days. Alternatively, the  $\Delta omcZ$  ratio far exceeds the other two in the final time-point with very low current. The general amount of protein in this purified fraction does not correlate with metabolic current for the mutants. Thus, I decided to look at the distribution of OmcS and OmcZ nanowires in these fractions by western blot analysis.

Western blots of the filament preparations for each strain over time for both OmcS and OmcZ proteins are shown in Figure 4.3a. Each sample was normalized to the cell pellet mass of the smallest scraped biofilm ( $\Delta omcZ$  timepoint 2), then equal volumes were loaded onto the gel for each timepoint such that the protein loaded would represent the rough filament distribution in the biofilm at that timepoint. I see that there is no OmcS in the  $\Delta omcS$  strain, that  $\Delta omcZ$  shows a large increase in OmcS filament production and that WT has a very constant OmcS production. The quantification of the western by densitometry is shown in Figure 4.3b (top) as a visual guide. Blotting for

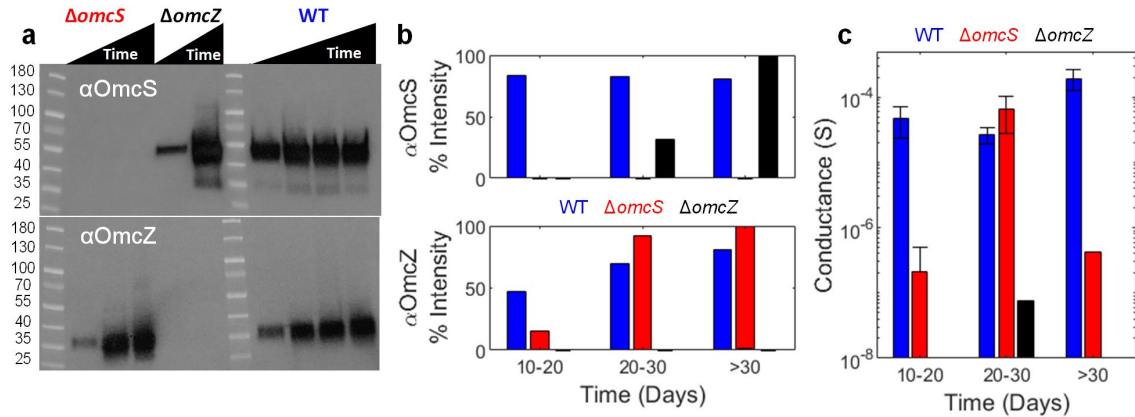


**Figure 4.3: Conductance increases with OmcZ production in biofilms.**

**a**, Westerns of the filament preparations blotted with antibody for OmcS (top) and OmcZ (bottom). The lanes were loaded by normalization of the cell pellet. The ladder is labeled in kilodaltons. **b**, Quantification of the western gels in **a** for OmcS (top) and OmcZ (bottom) normalized to the most intense band. **c**, The conductance of each biofilm across three strains measured in the indicated time range shown below. All errors shown are standard deviation.

OmcZ shows no signal for  $\Delta omcZ$  and that WT and  $\Delta omcS$  increase OmcZ production over time, with  $\Delta omcS$  exceeding WT levels. Quantification is again shown in Figure 4.3b (bottom) as a guide. These comparisons illustrate that although total protein in the filament prep was lower in  $\Delta omcS$  than in WT at the second time point, the amount of OmcZ was greater and correlates with the timeline of metabolic current (Figure 4.1a,c and Figure 4.2b, bottom). The opposite is true for OmcS which is greatly overproduced at late times in  $\Delta omcZ$  biofilms but again is not accompanied by an increase in current (Figure 4.1a,c Figure 4.2b, top). Western blot staining for Gro-El, a cytoplasmic protein<sup>123</sup>, showed no signal in the filament preps (SI Figure 4.2).

The conductance of each biofilm was measured under hydrating conditions in an anaerobic environment. The conductance of WT increased slightly over time while that of  $\Delta omcS$  increased to the second time point but then fell after 30 days (Figure 4.3c). The fall in conductance was likely due to poor electrode coverage on that last timepoint (SI Figure 4.1). Increases in conductance are correlated with an increase in OmcZ production in  $\Delta omcS$  in the second time point. The  $\Delta omcZ$  strain could only be measured once and

its second timepoint value was low but indicates that OmcS nanowires contribute some conductance to biofilms. The challenge with measuring the devices concurrently was that it was difficult to remove them from the graphite electrode without breaking them (SI Figure 4.1). This method could be improved in the future to get more consistent readings of biofilm conductance.

#### 4.4.2. OmcZ shows broad redox range similar to $\Delta omcS$ biofilms

While the redox potential of both OmcS<sup>100</sup> and OmcZ<sup>106</sup> has been previously reported after harsh denaturing treatments, it is important to evaluate the redox potential of whole filaments since these are physiologically relevant to the EET pathway. Because OmcZ is found closest to the anode under biofilm growth conditions and because it is essential for high current production<sup>118</sup> I focused on electrochemical studies of OmcZ nanowires. I utilized electrochemical techniques to determine the midpoint of OmcZ nanowire films. Under DPV, three peaks arose when measuring purified OmcZ nanowires near -280, -140, and -70 mV vs SHE. The values were averaged over both anodic and cathodic DPV

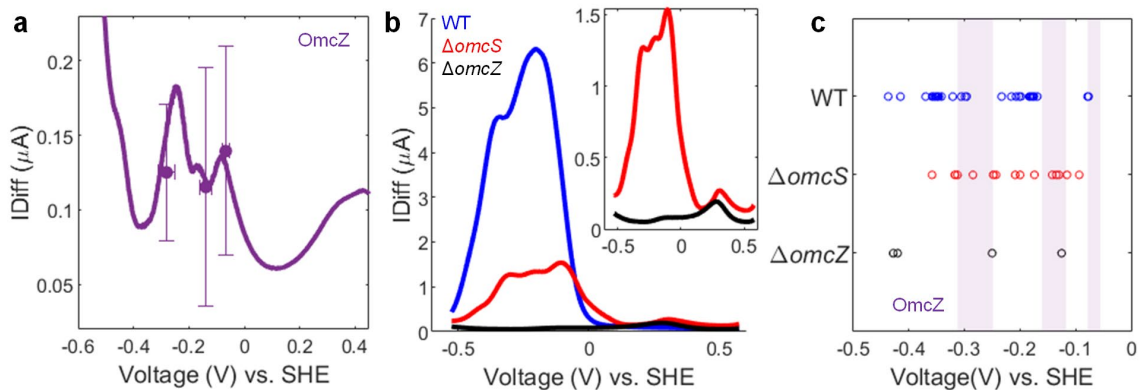


**Figure 4.4: OmcZ nanowires show multiple redox centers that overlap with biofilm signatures.** **a**, Differential pulse voltammetry of OmcZ nanowires with the averaged results of multiplex fitting the DPV signal. Three peaks were identified at -0.27, -0.34, -0.48 vs Ag/AgCl. **b**, Representative DPV signals from the three strains of biofilms from timepoints older than 20 days. **c**, All redox peaks taken from multiplex fitting of DPV signals shown over time plotted for each strain (biological replicates = 17, 7, 4 in WT,  $\Delta omcS$ , and  $\Delta omcZ$  respectively). Also shown are shaded purple boxes indicating the average  $\pm$  standard deviation of redox peaks in OmcZ (n=8 over 4 biological replicates combining anodic and cathodic values)(a).

scans (Figure 4.4a,c). The previously reported value of -220 mV could be skewed by exposed hemes in a monomer compared to a filament, or the harsh conditions utilized to purify the sample.

I then compared the behavior of the three strains of biofilms to the OmcZ nanowire behavior at late time points. I show representative DPV scans for the three strains with  $\Delta omcS$  and  $\Delta omcZ$  shown for clarity again in the inset (Figure 4.4b). I used multiplex fitting to fit the DPV data to produce Figure 4.4c which indicates the peaks that appeared across all biofilm samples over all periods of time. Overall, I see that the WT biofilm has two clusters of redox centers, and the  $\Delta omcS$  biofilm has a large spread with some clustering near the lower two potentials measured in OmcZ. WT is marginally more negative than  $\Delta omcS$  and OmcZ potentials.  $\Delta omcZ$  biofilms showed very low signal with some peaks but the overall signal was greatly lower than the other two strains due to poor growth overall (Figure 4.2a).

#### **4.4.3. Electrochemical gating on biofilms shows overlap with OmcZ**

Electrochemical gating is a tool that can reveal underlying mechanisms of conductivity for a material. If a material behaves like a band conductor, the material will show a constant current with gate voltage and only a change in current with source-drain voltage. If the material is a redox conductor the material will show a peak in current with gate voltage near the redox centers of the material<sup>124, 125</sup>. I performed electrochemical gating on OmcZ nanowire networks by using the bipotentiostat method<sup>126</sup>. I found that OmcZ exhibits a large gating effect with a large enhancement of current around the potentials found by DPV centered at  $-186 \pm 3$  mV (Figure 4.5a). OmcS exhibits a smaller peak centered around  $-146 \pm 10$  mV. The fact that OmcZ and OmcS exhibit peaks near

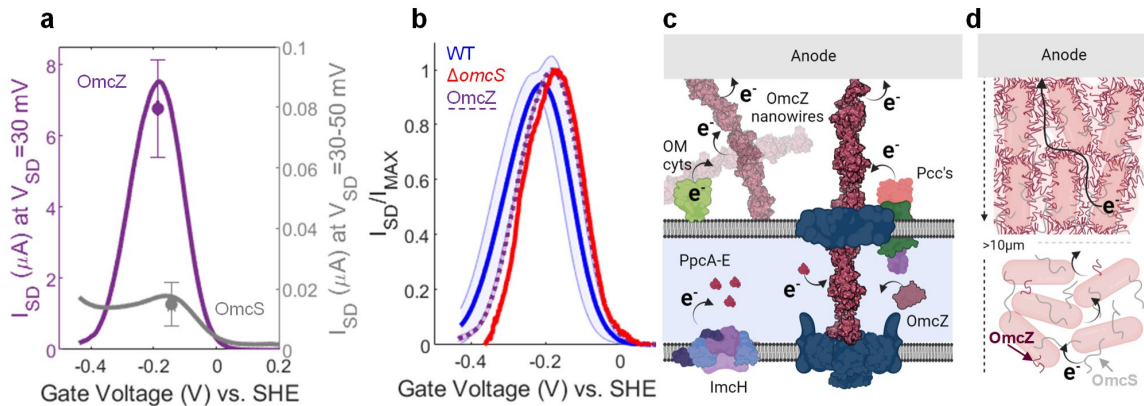


**Figure 4.5: Electrochemical gating shows overlap between biofilm and OmcZ response.**

**a**, Electrochemical gating of nanowire films of OmcZ and OmcS compared. Representative data curves are shown with the average peak center and height overlaid as dots. Values are mean  $\pm$  standard deviation ( $n=2$  biological replicates for both). **b**, Gating on  $\Delta omcS$  (red) and WT (blue) biofilms with OmcZ (dashed purple) gating for comparison. All responses are normalized to the maximum current for better comparison. Shading indicates standard deviation of averaged curves ( $n=15, 1, 2$  for WT,  $\Delta omcS$ , and OmcZ respectively). All scans shown are in the cathodic direction. **c**, A model for extracellular electron transfer to anodes involving OmcZ nanowires which can communicate with periplasmic cytochromes given its broad span of redox potentials. OmcZ may also accept electrons from other outer membrane cytochromes. **d**, A model for the composition of WT biofilms shows the nanowires dispersed at varying density with OmcZ in very dense aggregates near the anode and sparse greater than  $10\mu\text{m}$  away due to changes in metabolic needs of the biofilm. Panel **d** generated in Biorender.

their redox centers suggests that they are redox conductors<sup>126</sup>, as has been shown for OmcS<sup>111</sup>. The gating curve for OmcZ was quite wide which indicated multiple overlapping redox potentials contributing to the maximum current, consistent with the tri-fold redox behavior found in DPV<sup>126</sup>. These results are consistent with the fact that OmcZ has been shown to have higher conductivity than OmcS at pH 7<sup>19</sup>. These and previous measurements are performed in a two-probe geometry and cannot perfectly exclude the effects of contact resistance between OmcS and OmcZ. The solvent exposed hemes in OmcZ can be contributing to a lower contact resistance, and the greater than 400-fold difference in peak gate current between the two nanowires. Gating on WT and  $\Delta omcS$  biofilms exhibit some overlap with gating on OmcZ nanowires when the current is normalized to the maximum (Figure 4.5b). The WT biofilms, consistent with their

DPV signal, exhibit a more negative potential shift when compared to the other two. The shape and peak positioning of  $\Delta omcS$  agrees very well with OmcZ nanowires.

#### 4.5 Discussion

The combined results demonstrate that OmcZ is the primary nanowire required for biofilm conductivity and current production. I show that although OmcS was thought to be critical to early-stage biofilm growth, the biofilm lag and recovery is largely correlated with external production of OmcZ nanowires. Thus the lag is likely due to delay in the production of OmcZ nanowires by  $\Delta omcS$  cells. The regulatory mechanisms of OmcS and OmcZ production are not fully understood. It is known that pilA-N, and hence PilR/PilS system<sup>127</sup>, is required for extracellular localization of OmcS, OmcZ<sup>20</sup>. It's known that overexpression of OmcZ can downregulate OmcS expression<sup>128</sup> and it was recently shown that transcription of pilA-N, OmcS, and OmcZ share the transcriptional regulator GSU1771<sup>129</sup>. The complex regulatory relationship between these proteins could explain the lag in extracellular OmcZ production in the  $\Delta omcS$  strain.

Knowing that OmcZ forms nanowires that aggregate and that they accumulate near the anode surface, it seems reasonable that they can be responsible both for turnover current (DPV) and source-drain current, or conductance along the biofilm-anode interface<sup>125</sup>. This would explain the similarity between responses of biofilms and OmcZ nanowires.

The multicentered, wide redox potential window of OmcZ nanowires make them capable of interacting with a larger variety of electron donors and acceptors<sup>106</sup>. It is critical to note that OmcZ has redox centers within range of the most abundant

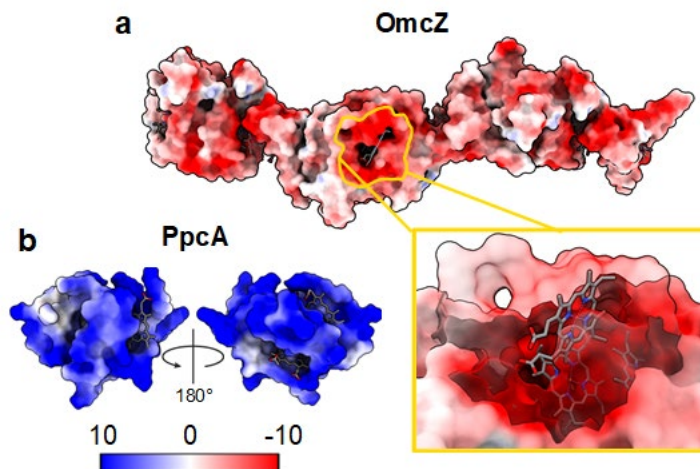


**Figure 4.6: Electrostatic potentials favor interaction between PpcA and OmcZ.**

**a**, The electrostatic surface potential of OmcZ with the inset showing a very negative area around an exposed heme of OmcZ. **b**, Surface potential of PpcA showing largely positive surface. Colors are shown according to the color bar in units of kcal/e•mol.

cytochrome in the periplasm, PpcA, which is crucial for EET<sup>108</sup> (Figure 4.5c). The nanowires may also be capable of accepting electrons from donors in the periplasm to export to extracellular acceptors, contrasting with the somewhat outdated view that they only play a role on the cell surface. The electrostatic surface potentials of PpcA and OmcZ favor interactions near exposed hemes on each molecule (Figure 4.6). The wide range in potential of OmcZ implies that it could also accept electrons from porin cytochrome complexes or other outer-membrane cytochromes, who may divert electrons to OmcZ for more efficient delivery to the anode under biofilm conditions. The *extABCD* complex is important for current generation in biofilms and may directly give electrons to OmcZ<sup>130</sup>. Since OmcZ seems to form very dense aggregates around cells near the anode<sup>22, 118</sup>, perhaps it acts to facilitate a conductive matrix between the electrode and the cells so that any OmcZ nanowire contact with outer-membrane electron donors can easily pass electrons out of the cell, regardless if that OmcZ nanowire was actually anchored to that particular cell (Figure 4.5c,d).

In the layers of biofilm away from the electrode OmcZ is less abundant and it is possible that OmcS nanowires play a role there along with OmcB which appears more often farther from the anode (Figure 4.5d)<sup>131</sup>. Although  $\Delta omcZ$  biofilms did not grow well, they showed some low conductance in the second time point indicating they can confer some conductivity to biofilms but can't sustain high metabolic currents (Figure 4.3). WT biofilms show steady amounts of OmcS produced over time (Figure 4.2b). Immunogold labeling indicates OmcS is dispersed throughout the biofilm in WT<sup>16</sup>. Perhaps the metabolic cost of producing that specific ratio of cytochrome nanowires is ideal, but not required, to maintain through-biofilm conductance to the anode. Immunogold for OmcZ through  $\Delta omcS$  biofilms could tell us whether all cells produce OmcZ to compensate for a lack of OmcS or OmcZ is merely overproduced even more at the cells near the anode. The results shown here make it clear that OmcS plays a role in biofilms that can be filled by OmcZ and any other changes in cytochrome expression undergone by the cells.

I demonstrated that the metabolic response, conductivity, and redox properties of  $\Delta omcS$  biofilms is dominated by OmcZ nanowires. WT biofilm redox properties overlap with OmcZ but exhibit an additional more negative redox center. By tuning the quantity and type of nanowires within biofilms we can thus tune their conductivity or ability to interface with other materials. Turning on and off the expression of OmcZ nanowires would significantly impact the conductivity of biofilms. As we strive to achieve combination between living materials and electronics, tuneability is of the utmost importance.

## 4.6 Methods

### 4.6.1. Device fabrication and preparation

Devices were fabricated as described previously<sup>31</sup>. PDMS wells with outer diameter 9 mm and inner diameter 6 mm were attached to each device around the interdigitated array by ambient air plasma cleaning both the device and PDMS well on medium for 45s. Then the well was placed on the device and pressed firmly together. The gold electrodes were then electrochemically cleaned as described previously<sup>114</sup>. Briefly, each chip underwent a potentiostatic hold at 2.04 V for 5 s then a hold at -0.311 V for 10 s. The potential was then swept from -0.261 to 1.59 V at a scan rate of 4 Vs<sup>-1</sup> for 20 scans. Then the scan rate was reduced to 100 mV/s for 4 additional scans. Afterwards the electrode was rinsed with ethanol and water.

### 4.6.2. Bacterial strains and growth conditions

*Geobacter sulfurreducens* wild-type (WT) strain PCA (designated WT) (ATCC 51573)<sup>12</sup>, *omcS* knock-out mutant strain<sup>23</sup> (designated as  $\Delta omcS$ ), the *omcZ* knock-out mutant strain<sup>24</sup> (designated as  $\Delta omcZ$ ) were obtained from our laboratory culture collection. *G. sulfurreducens* cultures were maintained at 30 °C under strictly anaerobic conditions in growth medium supplemented with acetate (10 mM) as the electron donor and fumarate (40 mM) as the electron acceptor. As described previously<sup>18</sup>, the *G. sulfurreducens* cells were grown in sterilized and deoxygenated NBAF medium<sup>113</sup>, and 1 L NBAF medium contained the following: 0.04 g/L calcium chloride dihydrate, 0.1 g/L, magnesium sulphate heptahydrate, 1.8 g/L sodium bicarbonate, 0.5 g/L sodium carbonate, 0.42 g/L potassium phosphate monobasic, 0.22 g/L potassium phosphate dibasic, 0.2 g/L ammonium chloride, 0.38 g/L potassium chloride, 0.36 g/L sodium

chloride, vitamins and minerals as listed in <sup>113</sup>. 1 mM cysteine was added as an oxygen scavenger. All bacterial strains were stored at 80 °C as 15 % DMSO stocks for *G. sulfurreducens*.

#### **4.6.3. Biofilm Growth**

Graphite electrodes were cleaned by soaking in 0.5 M HCL and 0.5 M NaOH. Then 2-3 IDA devices were attached to a plastic coverslip with double tape, then the assembly was attached via carbon paint to the surface of the graphite such that each gold finger of the device was electrically connected to the graphite. After the carbon paint dried, PDMS was poured into an 8 cm<sup>2</sup> well surrounding the devices such that the electrical contacts of the device were coated except the center array of electrodes. The PDMS was cured in an oven at 120 °C for 30 mins. The graphite electrode was then attached to the microbial fuel cell connector pin and assembled as described previously<sup>113</sup>. WT,  $\Delta omcS$ , and  $\Delta omcZ$  were handled in an identical manner. Cell cultures were thawed and grown in anaerobic NBAF medium in a 10 ml serum tube and grown to exponential phase, then transferred into a 100 ml bottle and grown to exponential stage twice before inoculation. Fuel cells were inoculated with 50ml of the third transfer of culture at OD around 0.4. MFC's were operated at 25 °C for the indicated time at which point cells were harvested and biomass and electrodes were measured. Interdigitated electrodes were removed from the graphite with a razor blade in an anaerobic chamber and kept anaerobic and hydrated until measurement. Growth medium was dabbed off and replaced with electrolyte solution so there was no excess acetate in solution.

#### **4.6.4. Filament Preparations**

Cells were scraped from biofilm with a plastic spatula and suspended in PBS isotonic wash buffer. The suspension was spun at 2500 g to pellet cells. The supernatant was poured off and the pellet dried for 1 min over a Kim wipe before recording cell pellet mass. The cells were then resuspended in 150 mM ethanolamine (ETA) at pH 10.5 and blended in a commercial blender on low setting for 2 minutes. The mixture was collected and spun at 13000 g for 30 minutes and the supernatant was collected. The filaments were precipitated with 12.5% saturated ammonium sulfate overnight at 4 C and then spun down at 23000 g for 1 hr. The pellet was collected and resuspended in 1.3 ml ETA pH 10.5 for all samples.

#### **4.6.5. Protein Normalization & Gels**

The cell pellet mass was recorded as described above. Before loading into gel each filament sample was normalized to the lowest cell pellet mass of 0.134 g so notably the amount of loaded protein per well is intentionally unequal and should represent the mixture of filaments per 0.134 gram of cells. The samples were mixed with 4X loading dye with  $\beta$ -mercaptoethanol as the reducing agent and boiled for 10 min at 95 C. Equal volumes of sample were loaded in the wells of BioRad 4-12% SDS gels and run at 190V for 36 minutes.

For westerns the gel was transferred to a PVDF membrane, blocked in 5% milk in TBST, then incubated with primary antibody overnight at 4 C. We used 1:500 OmcS antibody (2 mg/ml) and 1:2000 OmcZ antibody (2.75 mg/ml). The membrane was washed in TBST then incubated with secondary antibody for 1 hr at room temperature. The membrane was washed in TBST and water then incubated with Immun-Star AP Goat

Anti-Rabbit IgG (H+L) substrate for 5 mins. Membrane was imaged for colorimetric and chemiluminescence.

#### **4.6.6. Electrochemistry**

Platinum wire with 0.5mm diameter served as the counter electrode while an Electrolytica C-925 1mm (Ag/AgCl with 3.4 M KCl) served as the reference electrode. The reference was compared to a standard before each use. Cyclic Voltammetry (CV) and Differential Pulse Voltammetry (DPV) were performed using Gamry potentiostats. For all biofilms, CV was performed from 0.4 to -0.7 with step size of 1 mV at a scan rate of 5mV/s unless otherwise indicated. All DPV was performed from 0.4 to -0.7 with a step size of 1mV, sample period of 0.5 s, pulse size of 25 mV and pulse time of 0.1s. The platinum counter electrode was freshly cut or cleaned in same manner as the gold electrodes before use. The electrolyte in all cases was 50 mM KH<sub>2</sub>PO<sub>4</sub> and 100 mM KCl at pH 7 sparged with N<sub>2</sub> for at least 30 mins and stored in a serum tube to remain anaerobic<sup>113</sup>. Peak fitting was performed using MATLAB for DPV results.

Electrochemical gating was used as described previously<sup>125</sup>. Briefly two potentiostats were connected to the IDA such that one formed a three-electrode circuit with the left side of the IDA and the other formed a three-electrode circuit with the right. Both used common counter electrode and reference. Synchronized cyclic voltammetry sweeps were performed with a 30-50 mV offset so the source-drain voltage was 30-50 mV. The source-drain current was calculated by subtracting the raw source current from the raw drain current to remove any faradic background current.

#### 4.6.7. Conductance Measurements

The conductance of the biofilm was measured with a Gamry potentiostat while submerged under electrolyte solution. The current at a constant voltage was recorded for 100 s and an exponential fit to the current versus time trace was used to determine the current at each voltage point. The IV curve was extracted, and the slope of the linear region was used as the conductance.

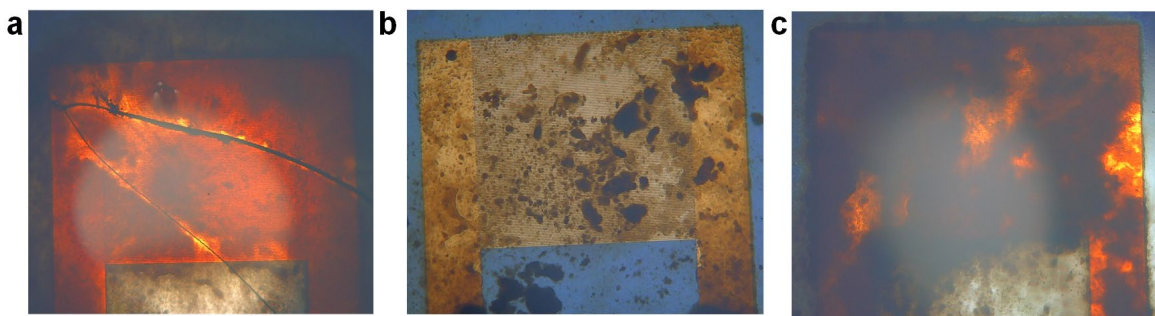
#### 4.6.8. Data Analysis

All data analysis was performed using MATLAB scripts including the EzyFit<sup>115</sup> and peakfit<sup>116</sup> modules.

#### 4.6.9. Electrostatic Potential Visualization

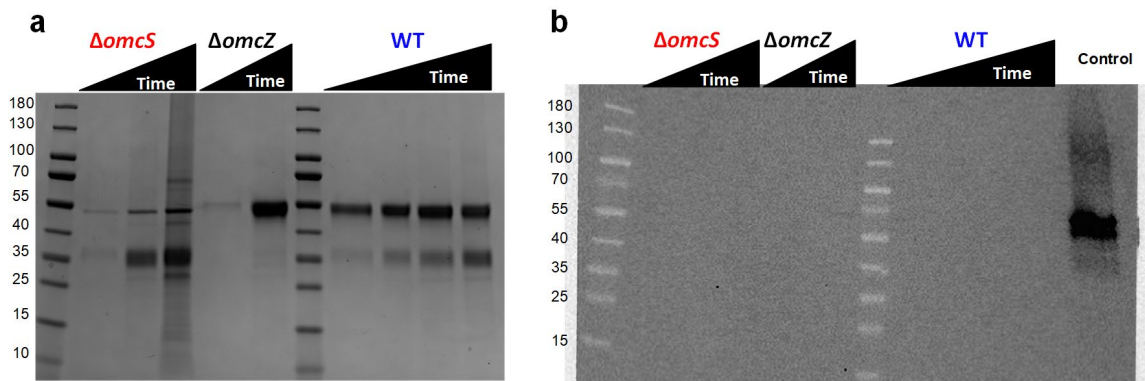
The electrostatic potential was generated on OmcS (PDB: 7LQ5) and PpcA (2MZ9) using ChimeraX software<sup>132</sup>.

### 4.7 Supplement



**SI Figure 4.1: Atypical growth on  $\Delta omcS$  final timepoint.**

**a**, Coverage of  $\Delta omcS$  biofilm from > 30 days on electrode that broke when removing from graphite surface. **b**, Coverage of an electrode on same graphite surface in the exact same fuel cell had less coverage likely due to bad electrical connection. The final conductance point was measured on this biofilm which may explain the drop from previous timepoint as this coverage is atypical. **c**, Coverage of solid electrode used for electrochemistry also taken from the same graphite surface showing typical coverage. All gold electrode are 3mm wide for scale.



**SI Figure 4.2: Additional gel images on filament preparations.**

**a**, Coomassie stained gel of filament preparations used in this study. **b**, Anti-Gro-EL western of filament preparations. Gels were loaded by normalizing to cell pellet. Final lane is the lysate of collected cells from the later time WT strain.

## 5. Living Photoconductors

*Microbial biofilms as living photoconductors due to ultrafast sub-picosecond electron transfer in cytochrome OmcS nanowires*

Jens Neu\*, Catharine C. Shipps\*, Matthew J. Guberman-Pfeffer, Cong Shen, Vishok Srikanth, Jacob A. Spies, Nathan D. Kirchhofer, Sibel Ebru Yalcin, Gary W. Brudvig, Victor S. Batista, and Nikhil S. Malvankar

\*These authors contributed equally

This chapter is a modified excerpt of a published paper<sup>133</sup>.

DOI: <https://doi.org/10.1038/s41467-022-32659-5>

### 5.1 Author Contributions

J.N. and N.S.M designed experiments, J. N. fabricated electrodes and performed fs-TA with J.A.S., J.N. and C.C.S. measured conductivity of nanowires and biofilms C.C.S. measured UV-Vis spectra, M.J.G. performed computation under the supervision of V.S.B, C.S. grew biofilms on electrodes in microbial fuel cell and fabricated electrodes, V.S. purified protein nanowires, N.K. and S.E.Y. performed pc-AFM, G.W.B helped with data interpretation and N.S.M. supervised the project. J.N. C.C.S. and N.S.M. wrote the manuscript with input from all authors.

### 5.2 Summary

Light-induced microbial electron transfer has potential for efficient production of value-added chemicals, biofuels and biodegradable materials owing to diversified metabolic pathways. However, most microbes lack photoactive proteins and require synthetic photosensitizers that suffer from photocorrosion, photodegradation, cytotoxicity, and generation of photoexcited radicals that are harmful to cells, thus

severely limiting the catalytic performance. Therefore, there is a pressing need for biocompatible photoconductive materials for efficient electronic interface between microbes and electrodes. Here I show that living biofilms of *Geobacter sulfurreducens* use nanowires of cytochrome OmcS as intrinsic photoconductors, without the need for additional dyes. Photoconductive atomic force microscopy shows >10-fold increase in photocurrent in purified individual nanowires. Photocurrents respond rapidly (<100 ms) to the excitation and persist reversibly for hours. Femtosecond transient absorption spectroscopy and quantum dynamics simulations reveal ultrafast (~200 fs) electron transfer between nanowire hemes upon photoexcitation, enhancing carrier density and mobility. Our work reveals a new class of natural photoconductors for whole-cell catalysis.

### **5.3 Introduction**

Living cells have been incorporated with quantum dots and nanostructures for fluorescent labelling and drug delivery for over two decades<sup>134</sup>. However, light-absorbing nanostructures have not been used to drive catalytic reactions inside of cells due to lack of biocompatibility and high cytotoxicity of foreign materials, such as photosensitizers, inside the cell which often limits the operational efficiency<sup>134</sup>. Furthermore, inherent defects in synthetic photosensitizers cause several problems such as photocorrosion, photodegradation and the generation of photoexcited radicals, which results in low stability, irreproducibility and lack of sustainability of biohybrid materials<sup>135</sup>.

Some bacteria produce light-absorbing centers but suffer from low electron transfer efficiency and a lack of durability<sup>134</sup>. Natural electron transfer proteins such as azurins, myoglobin and c-type cytochromes do not show photoconductivity<sup>136, 137</sup> due to short (~

ps) carrier lifetimes of the heme iron which inhibits any charge separation<sup>138</sup>. Covalently linking artificial photosensitizers to these proteins yields low electron transfer rate on the 10 ns timescale or slower, greatly limiting their applications<sup>139</sup>. Furthermore, it is not feasible to use of longer excited state lifetimes, such as electron injection from the triplet states due to rapid degradation caused by reactive oxygen species produced in these processes. Therefore, there is an urgent need to develop novel biomaterials capable of ultrafast primary electron transfer to achieve efficient charge separation, followed by sequential secondary electron transfer for long-lived charge separation and charge accumulation<sup>139</sup>.

To evaluate the use of engineered living materials as living photoconductors, we chose the electroactive soil organism *Geobacter sulfurreducens* because it has evolved the ability to export electrons, derived from metabolism, to extracellular acceptors such as metal oxides and electrodes in a process called extracellular electron transfer (EET)<sup>18, 19</sup>. Bacteria establish direct electrical contact to electron acceptors via micrometer-long, polymerized cytochrome nanowires, called OmcS, which eliminates the need for diffusive redox mediators<sup>18, 19</sup> (Figure 5.1b). Hemes in the OmcS nanowire form a parallel, slipped-stacked pair with each pair perpendicular (T-stacked) to the next pair, forming a continuous chain over the entire micrometer length of the nanowire<sup>7</sup> (Figure 5.1d). The minimum edge-to-edge distances is 3.4-4.1 Å between the parallel-stacked hemes and 5.4-6.1 Å between the T-stacked pairs.

Owing to this evolutionary optimized OmcS nanowire structure with seamless stacking of hemes, *G. sulfurreducens* can transfer electrons over one hundred times their size by forming more than 100 µm-thick highly-conductive nanowire network in

biofilms<sup>38, 140</sup>, which enables cells to generate the highest current density in bioelectrochemical systems<sup>141</sup>. Owing to large electron storage capacity, cytochromes also confer high supercapacitance to biofilms with low self-discharge and reversible charge/discharge<sup>142</sup>. Moreover, a network of purified nanowires can transfer electrons over thousands of times the size of a cell<sup>140</sup>. Therefore, *G. sulfurreducens* serves as an ideal model system for electrocatalysis, metal corrosion and production of fuels<sup>143, 144</sup>. It was previously thought that conductive filaments of the surface of *G. sulfurreducens* are pili<sup>145</sup> and a network of pili confers conductivity to *G. sulfurreducens* biofilms<sup>38, 143</sup>. However, structural, functional and localization studies revealed that nanowires on bacterial surface are composed of cytochromes whereas pili remain inside the cell during EET and are required for the secretion of cytochrome nanowires to the bacterial surface<sup>20, 146</sup>.

Nanowires could be widespread and their photophysical properties could be physiologically important because many *Geobacter*-like metal-reducing bacteria form highly conductive biofilms<sup>147, 148</sup> and are widely distributed at the surface of earth in shallow sediments which contain abundant sunlight and metal oxides<sup>149-151</sup>. The sediments are capable of transporting electrons over centimeters<sup>152</sup> and can convert incident light into electricity<sup>153</sup>. Illuminating visible light on *G. sulfurreducens* cells have been shown to improve its catalytic performance such as increase in metabolic electron transfer to metal oxides<sup>154</sup> or other semiconductive materials by over 8-fold compared to that observed under dark conditions<sup>149</sup>. Furthermore, light-induced bacterial electron transfer correlated well with the rates of microbial respiration and substrate consumption<sup>154</sup>. However, the underlying molecular and physical mechanism for this

increased photocatalytic performance has remained unclear. We hypothesized that cytochrome nanowires in the biofilms could be photoactive, enabling efficient electronic interface between microbes and electrodes.

In addition to light-induced whole-cell catalysis<sup>149, 154</sup>, artificially expressing cytochrome OmcS in photosynthetic cyanobacteria, increased catalytic performance in diversity of processes such as an increase in photocurrent by 9-fold<sup>27</sup>, increased nitrogen fixation by 13-fold<sup>155</sup> and improved photosynthesis by increasing 60% biomass<sup>156</sup> compared to the wild-type cyanobacteria. These studies highlight the important role of OmcS in light-driven biocatalysis. However, intrinsic photophysical properties of OmcS, which could account for these catalytic improvements, have not been investigated.

OmcS is also required for interspecies electron transfer in *Geobacter* cocultures to carry out “electric syntrophy”<sup>98, 143, 157</sup>. This interspecies electron transfer via naturally conductive microbial consortia is important in diverse environments<sup>158-160</sup>. Photosynthetic bacterial species have also been shown to perform electric syntrophy with light-driven conversion of CO<sub>2</sub> to value-added chemical commodities<sup>135</sup>. However, the components and pathways responsible for such light-driven biocatalysis have not been identified and potential for photoactivity beyond photosynthetic microorganisms remains largely unknown.

Here we show that living biofilms of *Geobacter sulfurreducens* use nanowires of cytochrome OmcS as intrinsic photoconductors. Surprisingly, nanowires show photoconductivity with ultrafast, sub-picosecond heme-to-heme electron transfer which could explain their influence on photocatalytic performance mentioned above. These rates are among the highest reported for excited-state electron transfer in biology<sup>161</sup>.

## 5.4 Results

### 5.4.1. Photoconductivity in living biofilms made up of OmcS nanowire network

To determine the role of OmcS nanowires in light-induced electron transfer, we used the genetically engineered *G. sulfurreducens* strain CL-1 because it overexpresses OmcS nanowires (Figure 5.1c-d) and forms highly conductive and cohesive biofilms<sup>16</sup> (Figure 5.1a). Upon laser photoexcitation ( $\lambda=408$  nm) which is specific to the Soret band of *c*-type hemes<sup>137</sup>, biofilm conductance remained ohmic and increased by  $72 \pm 21\%$  (Figure 5.1e-f). These studies show that living *G. sulfurreducens* biofilms can serve as intrinsic photoconductors.

### 5.4.2. Rapid photoconductivity in purified nanowires reversible for hours

To determine the origin of photoconductivity in biofilms, we purified nanowires from the CL1 strain (Figure 5.2a). The ultraviolet-visible (UV-Vis) absorbance spectrum of nanowires showed a strong Soret band at 410 nm for air-oxidized nanowires (Figure 5.2b). Nanowires were fully oxidized under these conditions because addition of oxidant

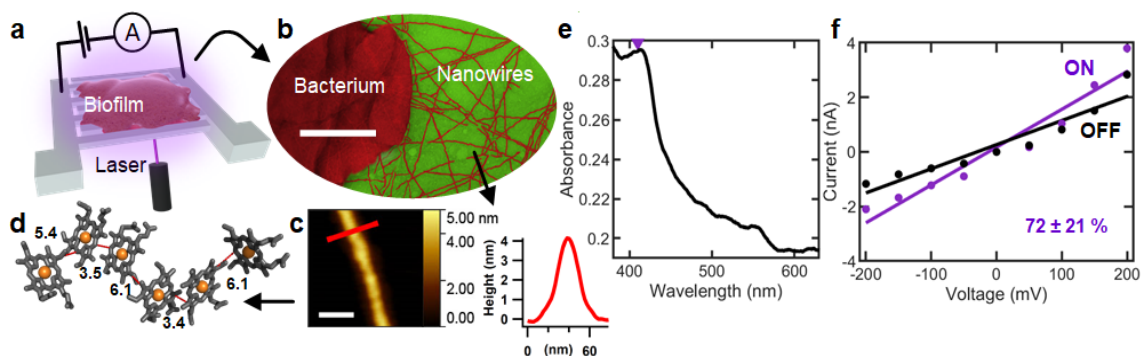


**Figure 5.1: Living photoconductors.**

**a**, Measurement schematic. Biofilms are grown on transparent fluorine-doped tin oxide (FTO) electrodes. **b**, Transmission electron microscopy of CL-1 cells producing OmcS nanowires. Scale bar, 200 nm. **c**, AFM height image of a single OmcS nanowire on mica (left) and corresponding height profile (right) at a location shown by a red line. Scale bar, 50 nm. **d**, Hemes in OmcS stack seamlessly over the entire micrometre-length of nanowires. Edge-to-edge distances are in Å. **e**, UV-Visible spectroscopy of biofilm on FTO electrode with the excitation wavelength of 410 nm marked as a pink triangle. **f**, Current voltage response of biofilm with the laser on and off. Percentage value represents mean  $\pm$  standard deviation (S.D) of two biological replicates.

(ferricyanide) did not change the spectrum (SI Figure 5.1). Upon addition of a chemical reductant sodium dithionite, the Soret band for reduced nanowires red-shifted to 420 nm as expected<sup>137</sup> (Figure 5.2b). I placed the nanowires on interdigitated gold electrodes and illuminated from the top (Laser Power = 100 mW/cm<sup>2</sup>). Photoconductance of nanowire network initially increased more than 6-fold (Figure 5.2c), but the extent of conductance increase decreased over time, likely due to laser damage. Nanowires responded faster than 100 ms (Figure 5.2c inset). The photoresponse persisted for hours but decreased over time (Figure 5.2c). Both the dark current and photocurrent were proportional to an applied voltage ranging from -0.2 to +0.2 V (Figure 5.2d), indicating an ohmic conduction behavior of nanowires similar to biofilms. Remarkably, nanowire networks, with and without laser excitation, showed a linear current-voltage response with an

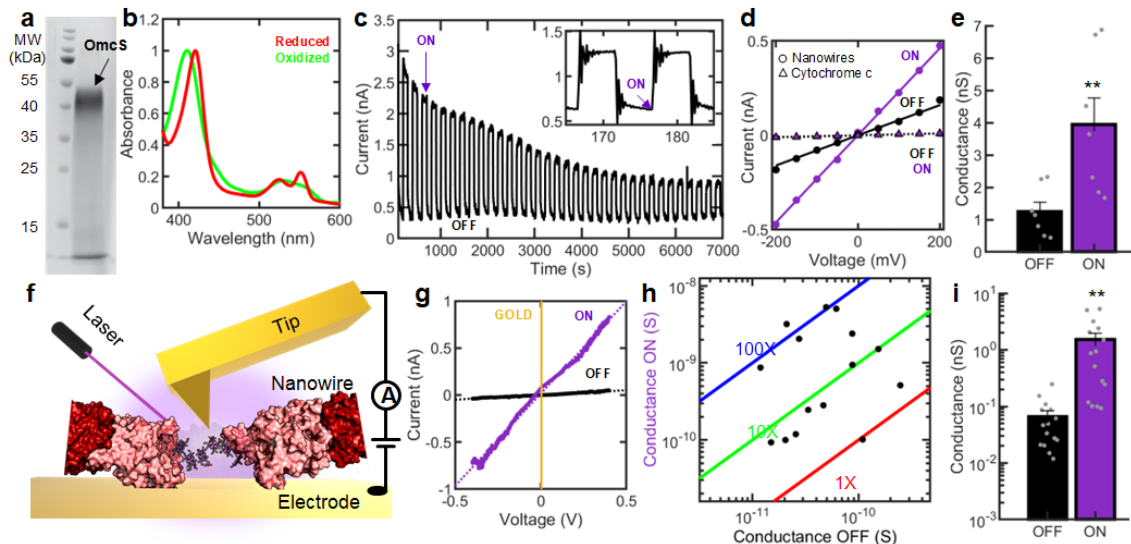


**Figure 5.2: High photoconductivity in purified protein nanowires.**

**a**, Heme staining gel of nanowires showing a single band of OmcS. **b**, UV-Vis spectrum of oxidized (green) and reduced (red) nanowires. **c**, Photocurrent response of nanowire network at 200 mV with the current decay of the off-state subtracted. **Inset**: Fast (<100 ms) photoresponse of nanowires. Axes are same as in Fig. 2c. **d**, Current-voltage response of nanowire network and cytochrome c for comparison **e**, Comparison of conductance of nanowire network with laser on or off. Values represent mean  $\pm$  standard error of the mean (S.E.M) with individual data points shown as grey dots (n=7). \*\* indicates p value = 0.003. **f**, Schematic of pc-AFM of individual nanowires. **g**, Current-voltage response of an individual nanowire with a linear fit shown by a purple dashed line. **h**, Comparison of conductance increase upon photoexcitation in individual nanowires. Values represent mean  $\pm$  S.E.M. ( $10 \leq n \leq 120$ ). **i**, Comparison of conductance of individual nanowires with laser on or off. Values represent mean  $\pm$  S.E.M with individual data points shown as grey dots (n=15). \*\* indicates p value = 0.007.

average conductance increase of  $230 \pm 28\%$  ( $n=7$ ), which is higher than common perovskites<sup>162, 163</sup> and porphyrin nanowires<sup>164</sup> (Figure 5.2d-e). In contrast, horse-heart cytochrome-c showed very low dark current and photocurrent as expected<sup>136, 137</sup> when measured under identical conditions (Figure 5.2d). Switching the electrode material from gold to tungsten also retained photoconductivity, confirming that the measured response is not an artifact of the electrode material (SI Figure 5.2). Furthermore, chemically reduced nanowires ( $\lambda_{\text{Soret}}=420$  nm) did not show significant photoconductance upon excitation at  $\lambda=405$  nm, confirming that photoreduction of oxidized hemes are necessary for photoconductivity in nanowires at this excitation (SI Figure 5.1). The ratio of laser-on/ laser-off (on/off) current of nanowires increased with increasing laser power, further demonstrating that the measured photoconductivity is solely due to laser excitation (SI Figure 5.3). All these experiments together confirm that the nanowires show intrinsic photoconductivity which can account for observed photoconductivity in living biofilms. The difference in photoconductivity between biofilms and purified nanowires is likely due to non-conductive materials such as cells and polysaccharides present in the biofilms.

#### **5.4.3. Individual nanowires show up to 100-fold photoconductivity increase**

To quantify the photoresponse of individual nanowires, we used photoconductive atomic force microscopy (pc-AFM)<sup>165</sup> ( $\lambda=405$  nm, Initial Power =  $3.20$  kW/cm<sup>2</sup>). Individual nanowires generally showed a 10-fold increase in conductance upon photoexcitation with some nanowires showing up to a 100-fold increase (Figure 5.2h-i), likely due to variation in the laser power caused due to limitation of experimental setup (see Methods 5.6.7 and SI Figure 5.11). The difference in the photoconductivity between individual nanowires and nanowire network is likely due to inter-nanowire as well as

nanowire-electrode contact resistance. Notably, the observed 10 to 100-fold increase in conductance for protein nanowires at relatively low bias ( $< 0.5$  V) is substantially greater than that of synthetic porphyrins<sup>166</sup> that show only up to a 5-fold increase at very high bias of 12 V.

These experiments on individual nanowires confirm that the observed photoconductivity response in networks of nanowires is due to nanowires alone and not because of an artifact of the measurement setup. Furthermore, the observed photoconductivity is not due to heating effects because All pc-AFM experiments were performed in a temperature-controlled environment thus inhibiting any large increase in temperature. Furthermore, the linearity and stability of our IV curves indicate that measured conductivity increase is not due to heating (Figure 5.2g). In addition, the conductivity of OmcS nanowires decreases upon heating<sup>111</sup> whereas we observed up to 100-fold increase in conductivity upon photoexcitation.

#### **5.4.4. fs-TA reveals sub-picosecond charge separation in nanowire**

To understand the mechanism of photoconductivity in protein nanowires, we performed femtosecond transient absorption (fs-TA) spectroscopy by determining the electron dynamics upon photoexcitation on an ultrafast ( $\sim 100$  fs) time scale<sup>138,167</sup> (Figure 5.3a). Fs-TA tracks the UV-Vis spectral changes by changing the time delay  $\Delta\tau$  between the femtosecond laser pump and the probe pulses and recording a differential absorbance spectrum ( $\Delta A$ ) at each time delay<sup>167</sup> (Figure 5.3a). This difference spectrum contains information on the dynamic processes occurring in the system such as excited state energy migration, electron or proton transfer processes and isomerization<sup>167</sup>. In contrast to the above studies of photoexcitation in the Soret band (Figure 5.1 and Figure 5.2), we

performed fs-TA using excitation in the Q-band ( $\lambda=545$  nm) to avoid thermal damage, and to monitor changes in the region of the strongest absorption bands<sup>167</sup>. It is important to note that Soret and Q-band transitions arise from the same ground state making Q-band excitation a suitable proxy to monitor these processes<sup>167</sup>. Photoexcitation with  $\lambda=530$ , 545 and 400 nm yielded similar dynamics, demonstrating a wide spectral range for photoconductivity (SI Figure 5.4 and SI Figure 5.5). Neither buffer alone nor the blank substrate showed any response and measurements in solid and liquid state are similar (SI Figure 5.6 and SI Figure 5.7) indicating that observed dynamics are due to nanowires and not an artifact of the environment or the substrate.

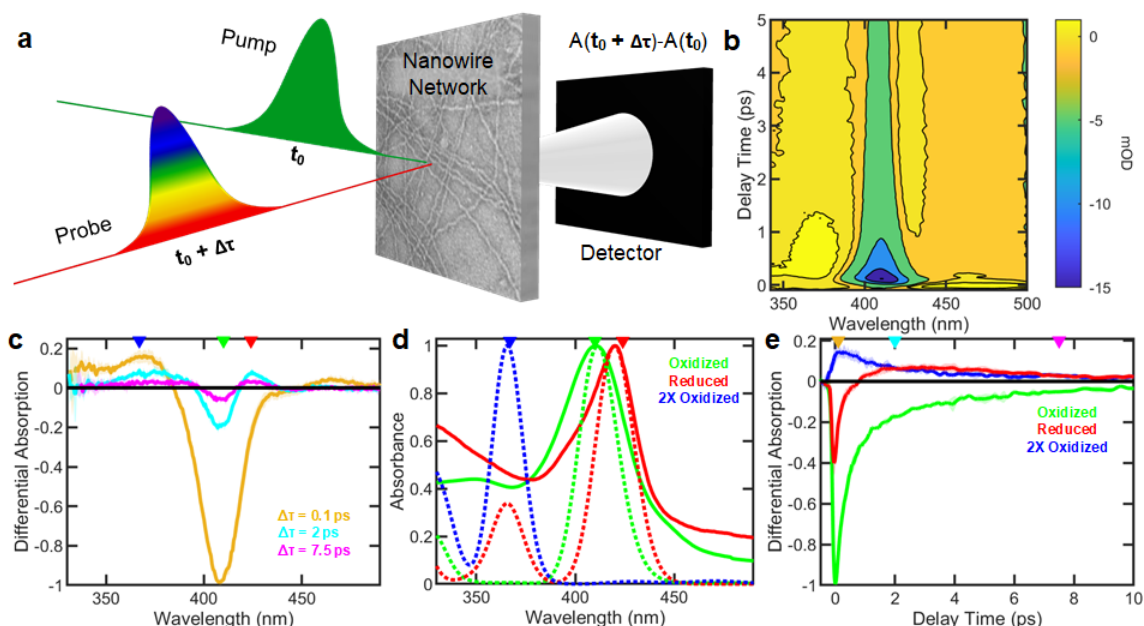


**Figure 5.3: Ultrafast (<100 fs) charge transfer between hemes in nanowires revealed by femtosecond transient absorption spectroscopy (fs-TA).**

**a**, Schematic of fs-TA. A pump beam ( $\lambda=545$  nm) followed by a probe beam with the difference absorption spectra detected. **b**, Averaged transient absorption data of nanowires ( $n=6$ ). **c**, Change in differential absorption with wavelength at different delay times. Key wavelengths are marked as  $\lambda=410$  nm (green),  $\lambda=424$  nm (red), and  $\lambda=367$  nm (blue). **d**, The experimental (solid) and simulated (dashed) spectra of oxidized, reduced, and singlet doubly-oxidized nanowires. Wavelength markers are same as in (c). **e**, Change in differential absorption over delay time at key wavelengths. Time-markers are shown in the same color as time traces in (c). Traces in c and e represent mean (line)  $\pm$  S.D. (shaded). ( $n=6$ ).

Upon photoexcitation of protein nanowires, electrons are promoted from the ground state to the excited state, decreasing the ground state population. This decrease caused a negative signal in  $\Delta A$  at 410 nm known as a ground state bleach<sup>167</sup>. In addition, we observed a positive  $\Delta A$  which is indicative of excited-state absorption at  $\lambda=367$  nm and  $\lambda=424$  nm after  $\Delta\tau=0.1$  ps and 2 ps, respectively (Figure 5.3c-d). These absorptions are absent in the native, air-oxidized, unexcited nanowires (Figure 5.3d), indicating that the photoexcitation is causing these absorptions. In particular, the absorption at  $\lambda=424$  nm agrees well with the absorption of chemically reduced nanowires (Figure 5.3d), suggesting that upon photoexcitation, excited-state electron transfer is reducing the hemes in the nanowires and thus photoreduction is a component of nanowire photoconductivity.

To understand the origin of different transient oxidation states, we determined the kinetics at the key wavelengths mentioned above using a sequential model<sup>167</sup> consisting of four interdependent exponential growth and decay rate equations that yielded the first excitation timescale of  $19 \pm 23$  fs (see Methods). This timescale is faster than the instrument response function ( $100 \pm 50$  fs) and can, therefore, be treated as an instantaneous excitation on the timescale of the measurement (Figure 5.4a). Following this excitation, the charges were transferred between hemes with a decay time of  $212 \pm 27$  fs. The corresponding spectra are a superposition of a ground state bleach and the appearance of a new feature around 367 nm, which can be attributed to the doubly oxidized hemes based on the spectral simulations (Figure 5.3d). Based on simulations (see below, Figure 5.4d), we conclude that the ultrafast charge transfer also results in the formation of a reduced heme in its excited state, which is spectroscopically dark. We also

found a second decay with a time constant of  $1.0 \pm 0.1$  ps that can be attributed to relaxation of the excited reduced heme that increases in absorption at the reduced Soret at  $\lambda=424$  nm. In addition, we found a third decay time of  $7.9 \pm 0.3$  ps that can be attributed to the recombination to their initial state, including charge transfers back to the singly oxidized heme ground states.

#### **5.4.5. Computations suggest excited state electron transfer between hemes**

We further compared our experimental UV-Vis spectra of nanowires with TD-DFT calculations of hemes in the nanowire (Figure 5.3d). The maximum of the computed Soret band in the reduced heme ( $\lambda=420$  nm) is shifted by 9.5 nm to the red of the band maximum for the oxidized heme, in good agreement with the 10.5 nm shift observed experimentally (Figure 5.3d). These computational analyses further suggest that photoexcitation causes reduction of hemes in the nanowires. Our finding is consistent with prior studies of photoreduction of monomeric cytochromes mediated by the light-induced excited state of hemes even in the absence of external electron donors<sup>168, 169</sup>.

To evaluate the transient kinetics data obtained using the sequential model fitted to experimental data, we performed quantum dynamics simulations at the Extended Hückel level of theory<sup>170, 171</sup>. We simulated the propagation of an electron wavepacket in the excited state from hemes in the nanowires, in a slip-stacked as well as in T-stacked orientation<sup>18</sup>. Our simulations suggest a  $\sim 100$  fs timescale for photo-induced charge transfer between the slip-stacked pair of hemes (Figure 5.4d). This timescale agrees with the experimentally determined timescale for the excited state charge transfer ( $212 \pm 27$  fs). The survival probability for electron transfer in a slipped-stack heme pair remains low ( $< 60\%$ ) for most energy levels, indicating a high probability for electron transfer to a

nearby heme within 100 fs (SI Figure 5.9). Thus the timescale for electron transfer between slipped-stack heme pair is similar for most initial energy levels.

## 5.5 Discussion

### 5.5.1. Hemes are likely electron source for observed photoreduction

As no external electron donor was added, our results suggest that the additional electrons that reduce the heme are intrinsic to the nanowire itself. We further analyzed the possibility that surrounding protein causes the observed photoreduction of OmcS hemes. Several aromatic amino acids, including tryptophan and tyrosine, are within 5 Å of the hemes in the OmcS. Although excitation of either tryptophan or tyrosine is not possible at the wavelengths used in this study<sup>168, 169</sup>, we considered a possibility that electron transfer can quench a photoexcited heme in a manner similar to flavins in a cryptochrome<sup>172</sup>. This quenching would reduce a heme and leave behind an amino acid radical. The most likely amino acid candidate for radical formation is tryptophan because its radicals have absorbance which would explain the 367 nm species<sup>173</sup>. While the formation of such radicals is possible, the signal strength in fs-TA measurements is determined by the molar extinction coefficients ( $\epsilon$ ) of the (transient) species. The molar extinction coefficient of OmcS's Soret band is approximately 100 times larger than those of tryptophan radicals<sup>100, 173</sup>. The ground state bleach represents all the photoexcited hemes in the OmcS nanowires and the species corresponding to  $\lambda=367$  nm and 424 nm have differential absorptions of  $\sim 20\%$  and  $10\%$  of the total magnitude, respectively. Therefore, the number of tryptophan radicals created from electron transfer needs to be larger than the number of excited hemes in OmcS if the radical species at  $\lambda=367$  nm arises from tryptophan. Such a possibility seems unlikely because only one radical can be

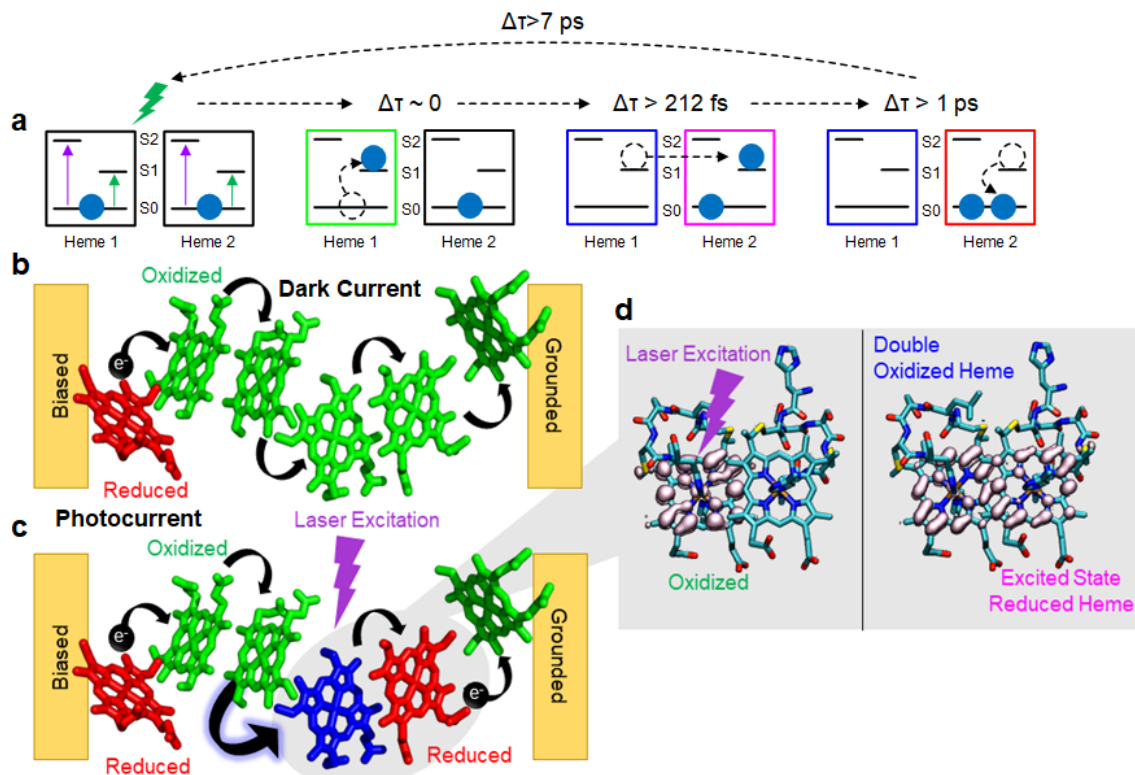


**Figure 5.4: Model for origin of photoconductivity in protein nanowires.**

**a**, Simplified energy level diagram depicting the changes that occur upon photoexcitation in transient absorption and their respective decay times. **b**, The dark current in the ground state arises due to propagation of a reduced state created by electron injection from the electrode. **c**, The photocurrent is due to the laser excitation initiating an ultrafast charge transfer between hemes, creating newly reduced and double oxidized hemes. The photoreduction provides additional charge carriers and larger driving force for charge transfer, which therefore increases the current under bias. **d**, Quantum dynamics simulations of ultrafast charge transfer between hemes in protein nanowires, forming a doubly oxidized heme and an excited state of a reduced heme.

created for every quenched excited heme. Thus, the observed spectra cannot be accounted for by amino acid radicals.

We also evaluated the possibilities of other electron sources causing photoreduction. We found that multi-photon processes are absent in our experiments because the ET dynamics were independent of the laser intensity and power (SI Figure 5.8). The magnitude of photocurrent is also linear with increased power (SI Figure 5.3). Redox impurities also did not contribute to the measured spectra because of identical dynamics

in solution and in solid-state (SI Figure 5.7). Photodegradation also did not change the electron transfer dynamics, only the magnitude of spectra by < 10% over two hours.

We therefore considered an alternative possibility that parallel-stacked hemes can serve as an electron donor and acceptor pair (Figure 5.4). We hypothesized that if the excited state charge transfer is occurring between two neighboring hemes with only one of the hemes being in the excited state. Such charge transfer would result in the appearance of a reduced heme and leave behind a doubly oxidized heme (Figure 5.4). The computed UV-Vis spectrum of a doubly oxidized heme indeed showed an absorption maximum at  $\lambda=365$  nm which agrees with the experimentally observed species at  $\lambda=367$  nm. Our computed spectrum of a doubly oxidized heme thus recaptures the blue shift observed in the transient absorption experiment (SI Figure 5.10). The qualitative agreement between the computed and experimental spectra is independent of the spin state of doubly-oxidized species such as the singlet and triplet state.

To identify the nature of doubly oxidized species, we performed an analysis of atomic spin populations. We found that the change in the spin populations occurs only on the ligands and not in the iron center. Therefore, our analysis suggests that doubly oxidized species are  $\text{Fe}^{3+}$  + porphyrin radical which agrees with the observed spectra at 367 nm. These analyses further suggest that the doubly oxidized species are not  $\text{Fe}^{4+}$  due to lack of change of spin density on the iron center upon additional oxidation of the heme in the  $\text{Fe}^{3+}$  state (SI Figure 5.10).

To further evaluate the thermodynamic feasibility of radical heme species, we used the Rehm-Weller cycle. This analysis requires four energetic terms: 1) energy required to form radical heme species (based on iron-porphyrin systems<sup>174</sup>) (1.7 V), 2) the ground

state redox potential of OmcS (-212 mV)<sup>100</sup>, 3) the photon energy used to excite OmcS nanowires ( $\lambda = 545 \text{ nm} = 2.3 \text{ eV}$ ), and 4) the vibrational energy difference between the ground and excited states called the Coulomb stabilization energy associated with the intermediate radical ion pair<sup>175</sup> ( $\omega_p$ )  $\sim 60 \text{ meV}$ . Therefore, the energetics of this process would be  $\Delta G_{\text{et}} = [1.7 \text{ eV} - (-0.212 \text{ eV}) + 0.06 \text{ eV}] - 2.3 \text{ eV} = -0.4 \text{ eV}$ . Thus,  $\Delta G_{\text{et}} < 0$  for the formation of the radical species. Our analysis is a lower estimate for the net energy available for the formation of the radical species. Therefore, in combination with our simulated analysis, our studies suggest that doubly oxidized species are  $\text{Fe}^{3+}$  + porphyrin radical and nanowires are photoreduced by ultrafast light-induced heme-to-heme charge transfer.

### **5.5.2. Proposed mechanism for ultrafast photoconductivity in OmcS nanowire**

Based on above results, we propose the following model for the origin of photoconductivity in OmcS nanowires (Figure 5.4). This model is focused on the singlet states and not triplet states because these states are spectroscopically dark and would be less pronounced due to their lower energies. As these nanowires transport charges through seamless stacking of hemes (Figure 5.1c), our prior experiments have shown that they can be treated as redox conductors, with the long-range charge transfer governed by a theoretically-predicted hopping mechanism with negligible carrier loss over micrometers<sup>111</sup>. All hemes in the nanowires are initially oxidized and in their ground state as confirmed by UV-Vis spectroscopy (Figure 5.2b). Upon applying a bias, electrons are injected from the electrode into the nanowire, creating a reduced state that travels through the nanowire (Figure 5.4b). The photoexcitation triggers an ultrafast charge transfer resulting in an additional reduced state that persists for picosecond timescale, without any

applied bias, far away from the electrode (Figure 5.4c). This newly formed reduced state will have a mobility similar to the electrode-injected state as they both are present in the same nanowire with identical structure. Therefore, upon photoexcitation, the density of reduced states is increased, thus increasing the carrier density of the nanowires to generate photoconductivity response in OmcS nanowires. The photoreduction observed in our fs-TA is consistent with this model.

In addition to the higher carrier density due to photogenerated electrons, it is likely that the mobility of electrons increases upon photoexcitation due to increased driving force for charge transfer in the excited state of hemes<sup>111</sup>. Upon photoexcitation an electron is promoted from the ground state to an excited state. The ultrafast charge transfer between neighboring hemes creates a reduced-state heme in the excited state and a doubly oxidized heme (Figure 5.4c-d). The reduced-state heme can then relax from the excited to the ground state. Upon photoexcitation, the uniformly oxidized nanowire is thus partially reduced and partially double oxidized (Figure 5.4c).

The generated doubly oxidized heme will alter the redox energies of the heme chain, with a more positive redox potential. We have previously found that the redox potential of OmcS hemes becomes substantially positive upon oxidation. The OmcS nanowires transport charges via a hopping mechanism<sup>111</sup> - a process in which a charge (electron or hole) temporarily resides at a heme, changing its redox state. The driving force for charge transfer depends on the redox energies of the electron donating and accepting hemes. Therefore, the charge transfer rate is directly related to the mobility.

For the fully oxidized (non-excited) state, this process initiates at the electrode surface where injected electrons hop to nanowire redox sites, creating locally reduced

hemes. For the photoexcited state, this process is enhanced because transferring an electron to the double-oxidized species, and removing an electron from a reduced heme, are significantly more favorable in the illuminated nanowire than for the oxidized nanowire in the dark. The increased likelihood for charge transfer upon photoexcitation will then result in increased mobility. Furthermore, the initial ultrafast charge transfer between hemes increases the lifetime of the photogenerated state. Both the generation of a “new” mobile charge and the increase in its mobility will contribute to the observed increase in conductivity upon photoexcitation.

In summary, we demonstrate, for the first-time, significant photoconductivity in a living system due to ultrafast light-induced charge transfer within protein nanowires. The surprising origin of photoconductivity in these natural systems lies in the higher carrier density and mobility upon photoexcitation.

Although ultrafast electron transfer can occur in monomeric cytochromes, it typically requires incorporated dyes as photosensitizers and sacrificial electron donors<sup>161</sup> which can be toxic to cells<sup>134</sup>. In contrast, we find that the protein nanowires intrinsically exhibit robust and ultrafast charge transfer without any need for such site-selective labeling. Our studies thus establish OmcS nanowires as photoconductors intrinsic to cells with capability of ultrafast electron transfer, thus eliminating the need for foreign materials such as molecular dyes or inorganic nanoparticles that limit the catalytic performance<sup>134</sup>.

Furthermore, our studies show that sub-ps charge transfer is possible in natural proteins in an excited state. Prior ultrafast electron transfer studies have reported the ground state rates of 15-90 ps in the closest-stacked hemes<sup>161</sup>. This difference is likely

because excited-state rates are known to be faster due to higher energy and larger orbital delocalization compared to the ground-state rates<sup>172</sup>.

Although many bacterial EET studies remain focused on electrons, protons play a very important role, not only in bacterial energy generation, but also in the electronic conductivity of proteins<sup>176</sup>. For example, through measurements of the intrinsic electron transfer rate, we previously found that both the energetics of a glutamine (proton acceptor) and its proximity to a neighboring tyrosine (proton donor), regulate the hole transport over micrometers in amyloids through a proton rocking mechanism<sup>31</sup>.

Therefore, it is very important to couple electron/proton transfer to accelerate EET and for the development of electronically conductive protein-based biomaterials.

The high surface area of these nanowires, combined with their biocompatibility and lack of toxicity, make them attractive candidates for an emerging field of light-driven whole-cell bioelectrocatalysis for a wide range of applications such as water splitting, chemical sensing and CO<sub>2</sub> fixation and production of chemicals, fuels and materials<sup>177</sup>. Our studies may also help establish the efficient and stable production of liquid fuels from sunlight using a liquid sunlight approach<sup>138</sup>. Future studies on nanowires with different heme stacking and protein environment<sup>19</sup> or substituting the metals from iron to zinc<sup>178</sup> or tin<sup>179</sup> could vary the interactions between the heme cofactors to alter the electronic and photophysical properties of nanowires for tunable functionality<sup>177</sup>.

## **5.6 Methods**

### **5.6.1. Bacterial Biofilm Growth and OmcS nanowire Purification**

*Geobacter sulfurreducens*<sup>9</sup> strain CL-1, which produces an elevated abundance of OmcS protein<sup>16</sup>, was obtained from our laboratory culture collection and grown on

electrodes in a bioelectrochemical system as previously described<sup>113, 148</sup>. For the growth in liquid culture, cells were grown until stationary phase<sup>113</sup> and collected via centrifugation, and then a slightly modified version of a previously described protocol<sup>18</sup> was used to shear extracellular filaments from the cells. In brief, pelleted cells were suspended in 150 mM ethanolamine pH 10.5 and blended for 2 minutes on low speed in a commercial unit (Waring). Cells and cell debris were removed by centrifugation, first at 13,000 and then at 23,000 x g. OmcS filaments were then collected either by precipitation in 12.5% ammonium sulfate or ultracentrifugation at 100,000 x g, in accordance with previously described protocols for obtaining microbial nanowires from *G. sulfurreducens*<sup>38</sup>. Collected OmcS filament samples were resuspended and stored in 150 mM ethanolamine pH 10.5 and dialyzed to remove residual ammonium sulfate where appropriate.

### **5.6.2. UV-Vis Spectroscopy**

UV-Vis spectra were recorded with an Avantes (AvaSpec-ULS2048CL-EVO). For nanowires, a quartz slide was cleaned with ethanol and 2  $\mu$ l of 80  $\mu$ M protein was dropped on this slide and then dried for 20 min in the desiccator. Another 2  $\mu$ l was dropped on the same spot and again dried in the desiccator for 20 min. The spectrum was collected for the air oxidized sample. Then 40 mg/ml of sodium dithionite in water was dropped to cover the protein spot (2-3  $\mu$ l). The dithionite caused a chemical reduction of the hemes in the protein. The spectrum of the reduced material was then recorded. All spectra were normalized such that the minimum and maximum absorbance values for wavelengths above 380 nm were set to zero and 1 respectively. The biofilm solid state

measurements were taken on a FTO electrode in hydrating conditions with the background of a clean FTO electrode subtracted.

### **5.6.3. Electrode Fabrication**

Three different types of electrodes, based on gold (Au), Tungsten (W) and fluorine doped tin oxide (FTO), were used. The designs consisted of interdigitated electrodes, which create a “finger” pattern in which every odd-numbered line is connected to one pad, and every even numbered to the opposite electrical contact. This dense electrode packing ensures a large number of electronic contacts. The measured data are averaging over 132 wire connection pairs and provides superior signal compared to a single electrode device.

For the gold-electrodes, the spacing between each line was 5  $\mu\text{m}$ , and for the tungsten and FTO-electrodes, the spacing was 10  $\mu\text{m}$ . For all cases, the electrode (the metalized part) was 10  $\mu\text{m}$  wide.

The gold and tungsten electrodes were fabricated using UV-Lithography on thermally oxidized Silicon wafer. The thermal oxidation created a 300 nm silicon oxide layer which provides a plain and electrically insulating substrate. The metal electrodes were fabricated by spin coating a double resist, consisting of LOR 5-A and S1805. LOR 5-A was coated at 3000 rpm for 1 min followed by 5 min heating at 180 °C. Following this baking step, a second resist layer S1805 was applied at 3000 rpm for 1 min and cured at 120 °C for 2 min. Afterwards, the resists were exposed to UV radiation through a shadowmask and developed in MIF 319 developer for 2 minutes. The structured photoresists were then metalized using 5 nm Ti or Cr and 40 – 60 nm Au or W. A lift-off in heated (80-120 °C) NMP removed the metalized resists and resulted in the final

microstructure electrode. A protection coating was then spin coated onto the device. This coating was washed off with acetone before using the electrode. Each electrode was tested prior to protein deposition to ensure proper electric insulation between the two electrodes.

For the FTO IDE electrodes, commercially available FTO on Quartz glass was used. S1805 resist was spin coated and structured as previously described. After structuring this resist was used as a soft mask in reactive ion etching. The etching was carried out in an Oxford Plasmalab 100 RIE with a chamber pressure of 8 mTorr, and a gas flow of 8 sccm Cl<sub>2</sub> and 40 sccm Ar. The etching was carried out until the unwanted FTO was completely removed. The remaining photoresist was cleaned off in hot NMP (120 °C) and the final devices were covered with protective coating. This coating was removed with acetone prior to usage of the electrodes. Each electrode was carefully checked to ensure that the two contacts are electrical insulated.

#### **5.6.4. DC Conductance of Biofilms and Nanowires**

Conductivity measurements on nanowires and biofilms were performed as described previously<sup>180</sup>. Connections to device electrodes were made with a probe station (MPI TS50) inside a Dark Box which formed a Faraday cage and also blocked background light. Current and voltage were applied using a semiconductor parameter analyzer with preamplifiers (Keithly 4200 A-SCS) allowing for 1 fA current and 0.5  $\mu$ V voltage resolution. Two-point DC conductance measurements utilized two probe needles to contact the device on two adjacent electrodes. A fixed voltage in the range of +/- 0.3 V was applied to the two electrodes for a minimum of 100 s in sampling mode until a

steady current was reached. Voltage-current points were fit with a line, and the slope was used to determine conductance (G).

Devices were prepared by dropping 0.5  $\mu\text{L}$  of 8  $\mu\text{M}$  nanowires in 150 mM ethanolamine pH 10.5 on to the device and let dry in ambient atmosphere overnight. The drop formed on the material had a diameter of 1.4  $\pm$  0.1 mm. The electrode area was 2x2 mm, which ensured that all the material was electrically contacted.

To perform photoconductivity measurements, the previously described probe station was equipped with a diode laser, with an average output flux of 100  $\text{mW}/\text{cm}^2$  and a center wavelength of 408 nm. This laser spot was adjusted to be larger than the electrode area which ensured a homogenous excitation of the material. The laser beam was blocked/released using an optical shutter with a 1 ms response time.

Conductance measurements on reduced nanowires was performed by mixing 0.25  $\mu\text{L}$  of a concentrated solution of sodium dithionite with 9.75  $\mu\text{L}$  of nanowires in an anaerobic environment such that there was 50-fold molar excess of dithionite to heme concentration in the final solution. 0.5  $\mu\text{L}$  was dropped onto an electrode and dried in the anaerobic chamber overnight.

#### **5.6.5. Transient Absorption (TA) Data Collection**

The transient absorption spectra were collected at the Center for Functional Nanomaterials (CFN), part of the Brook Haven National Laboratory. Further data was collected at Drexel University. The signal to noise ratio of the commercial CFN spectrometer was superior to the data from Drexel, hence the data collected at Drexel were solely used in the supplement of this manuscript. The detailed description refers to the data collection at CFN.

The TA spectra were collected using a Helios (Ultrafast Systems) TA spectrometer. The excitation wavelength was generated in a TOPAS OPA. The probe pulse was generated via supercontinuum in calcium fluoride.

For each measurement, spatial overlap was optimized for strongest signal. Each set of data was iterated for several hours. Each iteration was then compared to the mean of the iteration to ensure long-time stability of the spectrometer and the sample material.

The sample was prepared by drop casting 5  $\mu\text{l}$  of protein solution onto a freshly cleaned quartz substrate. The samples were allowed to dry for 60 minutes in a desiccator. This deposition was repeated to create thicker films. Based on the optical transmission a location on the sample with sufficient Soret band absorption and acceptable scattering was chosen.

#### **5.6.6. Transient Absorption (TA) Data Processing**

The collected TA spectra were processed using three softwares: Surface Xplorer (Ultrafast Systems), a selfwritten matlab script, and Glotaran (<https://www.jstatsoft.org/article/view/v049i03>). Surface Xplorer was used to visualize the data and select measurements with adequate signal to noise. This selection reduced the number of processed spectra to 15. Of these measurements seven were pumped at 545 nm (shown in the main text) four pumped at 530 nm (shown in SI) and four pumped at 400 nm (shown in SI). All these measurements were evaluated to determine kinetics and dynamics of the spectral evolution. The main evaluation was performed for a pump wavelength of 545 nm, as this was depositing the lowest energy and therefore heating into the sample material. The other two wavelength confirmed the determined kinetics.

Surface Explorer was used to compensate for spectral chirp associated with wavelength dependent dispersion in the used sample and the quartz substrate. This correction ensured that the time zero point was independent of the wavelength. After this initial processing, the measured 1024 wavelength points were adjacent averaged to 512 points, resulting in a wavelength resolution of approximately 1 nm.

The preprocessed data were then imported into the matlab script. Six measurements at 545 nm pump were averaged into a single set (after accounting for time-zero jitter). These data sets are shown in the main text. The dynamics at 410 nm, 367 nm, and 424 nm was simultaneously fitted with a double exponential function convoluted with the instrument response function and an instantaneous injection model as Heaviside function. The lifetimes from this simple three wavelength dynamic fit are used as starting points for the detailed target analysis using Glotaran.

The preprocessed data (from the Surface Explorer data processing) were then loaded into Glotaran and truncated to -2 ps to inf in time and 340-505 nm in the wavelength space. This software was used for global analysis. The model assumes a global decay dynamic defined by a fixed number of decay constants. Based on our model we decided that a sequential analysis is best suited to describe the processes in photoexcited OmcS.

The sequential model, however, cannot directly separate the individual species from the ground state bleach of the main species. This is caused by the temporal overlap between the decays and the parallel decay into the ground state from the excited heme species which is not completely undergoing a charge separation step.

The sequential model assumes an excitation, which fitted to  $19 \pm 23$  fs. This is faster than the instrument response function of  $100 \pm 10$  fs. The excitation can therefore be

considered to be instantaneous (justifying the used Heaviside approximation in the preliminary analysis in matlab). Following the excitation, the charges are transferred from one heme to another within  $212 \pm 27$  fs. The corresponding spectra are a superposition of a ground state bleach and the appearance of a new feature around 367 nm, which is identified as a double oxidized heme (according to the presented spectral simulation). This charge transfer results in the formation of a reduced heme in the excited state. A second decay with a time constant of  $1 \pm 0.1$  ps describes the relaxation of the excited reduced heme. A final third time constant with  $7.9 \pm 0.3$  ps describes the relaxation of the system to its initial state, including charge back transfer to the single oxidized heme ground state.

#### **5.6.7. Photoconductive AFM (pc-AFM)**

Topography and electrical conductivity of nanowires on the gold surface were both measured using conventional tapping (AC) and conductive atomic force microscopy (cAFM, ORCA™) measurement modes with a commercially available AFM (Cypher ES, Oxford Instruments Asylum Research, USA) equipped with blueDrive™ photothermal excitation. The probe was a commercially available ASYELEC-01-R2 probe (Asylum Research) with Ti/Ir coating and nominal resonant frequency  $f = 75$  kHz, spring constant  $k = 2.8$  N/m, and tip radius  $R_{tip} = 28 \pm 10$  nm; measured values were  $f_0 = 86.6$  kHz and  $k_0 = 5.8$  N/m for the specific probe used in these measurements. In order to bias the sample, a small neodymium magnet ( $1/32'' \times 1/16''$  diam., K&J Magnetics) was both adhered and electrically contacted to the top surface of the nanowires-on-gold sample using silver paint (PELCO® Leitsilber, Ted Pella).

For tapping mode topography, the probe was driven with piezo actuation at a scan rate of 1 line/s, a free amplitude of 120 nm (0.58 V at a sensitivity of 207 nm/V), and a ~100 nm setpoint (0.5 V) to keep the tip-sample interaction very gentle in the so-called “attractive” or “non-contact” state to avoid damaging the nanowires.

Following the topographical scan, cAFM was used with a force setpoint of 50 nN to execute point I-V measurements on individual nanowires to measure their conductivity (n=15 nanowires), with a sample voltage sweep of  $\pm 0.5$  V at 1 V/s sweep rate for 20 sweep cycles at 2 kHz acquisition rate (1 kHz lowpass filter). The additional effects of photoexcitation on nanowire conductivity was examined by toggling the blueDrive™ laser as the excitation source (405 nm, 10 mW DC, with a spot diameter of  $2 \pm 1$   $\mu\text{m}$ ) on at least 20 sequential I-V sweeps. This was accomplished using the provided 0.01X filter cube (Asylum Research) and positioning the laser spot at the very apex of the probe tip (rather than using it as the probe oscillatory excitation); this provides  $[10\text{e-}3 \text{ W}]/[\pi*(1\text{e-}6 \text{ m})^2]*0.01 = 32 \mu\text{W}/\mu\text{m}^2$  illumination on the nanowires.

For control experiments in these pc-AFM measurements, a fresh template stripped gold sample (identical to the surface that the nanowires were deposited on) was also prepared with an electrical contact as above. As a positive control, the tip-gold conductivity was measured at the same conditions (50 nN loading force,  $\pm 0.5$  V at 1 V/s, 20 cycles) to ensure an ohmic contact in the absence of nanowires. As a negative control for photoconductive measurements, the tip-gold conductivity was measured at the same conditions (50 nN loading force,  $\pm 0.5$  V at 1 V/s, 20 cycles) with the blueDrive excitation sequentially toggled on and off to confirm that there was no change in tip-gold conductivity from the 405 nm excitation in the absence of nanowires.

### *pc-AFM Data Analysis*

At each collection point on an individual nanowire, at least 20 IV curves were collected. The last half of all the current voltage curves collected (minimum 10 curves) at a single point were used to calculate conductance. The IV curves were then sorted by nanowire and the slope of each curve was measured to get the conductance. For all nanowires, any outliers in conductance were removed by three median absolute deviation analysis on the  $\log_{10}$  of conductance. All the remaining individual conductance values for each nanowire were averaged to get the mean conductance of the single nanowire. The analysis for the laser OFF and laser ON current voltage curves was identical.

#### **5.6.8. Laser Characterization**

When interpreting photoexcitation experiments it is crucial to verify whether the experiment was performed in a linear or non-linear excitation regime. In the later the photoexcitation would be strong enough to trigger non-linear effects (i.e., saturable absorption) or cause electron-electron interaction (e-e scattering, Auger-effect, etc.). These effects would make a conclusive discussion of the experiments more challenging. In the linear regime, only a small percentage of molecules is excited, while the majority remains in their ground state. While there is no ultimate threshold for the linear vs non-linear regime, it is common to accept less than 1% excitation as linear.

We calculated the percentage excitations based on the known optical power density  $100 \text{ mW/cm}^2$ , and the total lifetime of the photoexcited system ( $\tau = 7.9 \text{ ps}$ ). The core concept used here is that for any given time point a certain number of photons hit the hemes and excite them while previously excited hemes are recombining into their ground state.

The recombination is described as  $N(t) = N(t-\Delta t) e^{-\Delta t/\tau}$ , with  $\Delta t$  as small time step<sup>181</sup>. The CW laser excitation was discretized using the time step to yield a total photon flux set by the laser power. Assuming a 100% quantum yield, this means that the generation of excited hemes is described directly by the photon flux. Starting at  $t=0$ , the population rises in competition with the recombination as  $N(t) = G(\Delta t) - N(t-\Delta t) e^{-\Delta t/\tau}$ . After a time of a nanosecond,  $N(t)$  approaches a quasi-steady state value of  $1.6 \cdot 10^6$  molecules/cm<sup>2</sup>. Comparing this value to the total protein density of  $2.5 \cdot 10^{13}$  molecules/cm<sup>2</sup> yields a ratio  $6.4 \cdot 10^{-6}$  %. This approximated value is well below 1%, justifying the linear interpretation of our experiments.

### 5.6.9. Computational Methods

*OmcS Structure Modeling.* The *c*-type heme cofactors of OmcS were modelled as iron porphyrin, with the methyl, thioether, and propionic acid substituents of the macrocycle replaced by hydrogen atoms. The two axially coordinated histidine residues were truncated at the C<sub>b</sub>-C<sub>g</sub> bond to give 1-methylimidazole ligands. This model system has been extensively used to theoretically characterize the structures, spectra, and reactivity of heme cofactors.<sup>182</sup>

The geometry of the heme model was optimized at the density functional theory (DFT) level in the reduced, singly oxidized, and doubly oxidized redox states. Harmonic frequency analyses confirmed that the heme model was at a local minimum on the respective ground state potential energy surface for each redox state. The reduced and singly oxidized species were optimized with the lowest spin multiplicity (singlet and doublet, respectively). The doubly oxidized heme model was examined in both the triplet and singlet manifolds. For the ground-state singly and doubly oxidized species, the

expectation value of the spin-squared operator,  $\langle S^2 \rangle$ , was 0.75, and 2.00 after annulation of spin contaminates.

All geometry optimizations and harmonic frequency analyses were performed with the Becke, three-parameter, Lee–Yang–Parr (B3LYP) hybrid functional<sup>183</sup> and a mixed basis set, applying the LANL2DZ effective core and valance functions to Fe,<sup>184</sup> and the 6-31G(d) basis to H, C, and N atoms. As with the vertical excitation calculations described in the next subsection, we employed tight self-consistent field convergence and an ultrafine integration grid, as implemented in Gaussian 16 revision A.03.

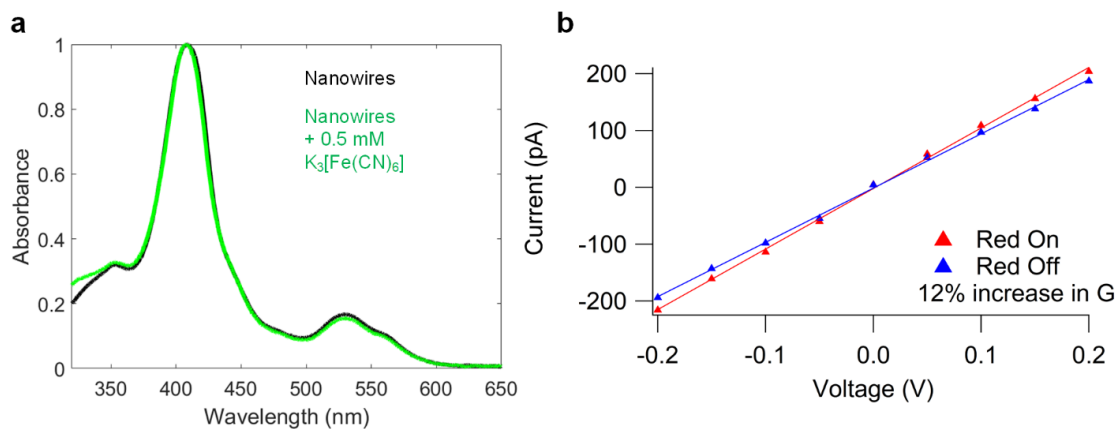
The simulation was performed on two types of adjacent heme pairs, namely T-Stack and slip stack present in the OmcS structure (Figure 5.1d). Only the slip-stack pairs exhibited charge transfer (SI Figure 5.9b). Therefore, this calculation was limited on neighboring hemes.

*Simulated absorption spectra.* The absorption spectrum of the heme in each redox state was simulated *in vacuo* with time dependent (TD)-DFT using the B3LYP functional and a 6-31+G(d) basis set for all atoms.<sup>185-187</sup> The predicted spectra were uniformly shifted by 38 nm to improve the alignment with the experimental spectra. The excited states of interest—the two Soret transitions—exhibited some spin contamination for the singly and doubly oxidized species, which is a well-known issue with TD-DFT<sup>188</sup>. However,  $\langle S^2 \rangle$  deviated by only 0.2-0.5 from the uncontaminated value, and the blue-shift predicted for the doubly oxidized species relative to the reduced or singly oxidized species was similar irrespective of whether it was modeled as a closed-shell singlet or open-shell triplet. We therefore conclude that the blue shift needed to explain the

experimental observation is independent of the spin contamination present in our open-shell calculations.

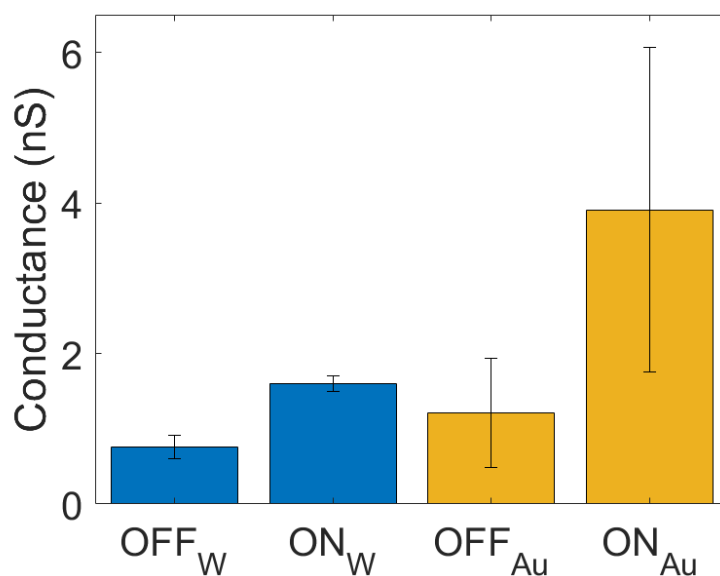
*Quantum dynamics simulations.* The dynamics of photoinduced intermolecular electron transfer between adjacent hemes was modeled with a previously described wavepacket propagation methodology implemented within the tight-binding Extended Hückel framework.<sup>170</sup> This level of theory was previously used to describe the electronic structure of iron-, as well as other, metalloporphyrins.<sup>171</sup>

## 5.7 Supplement



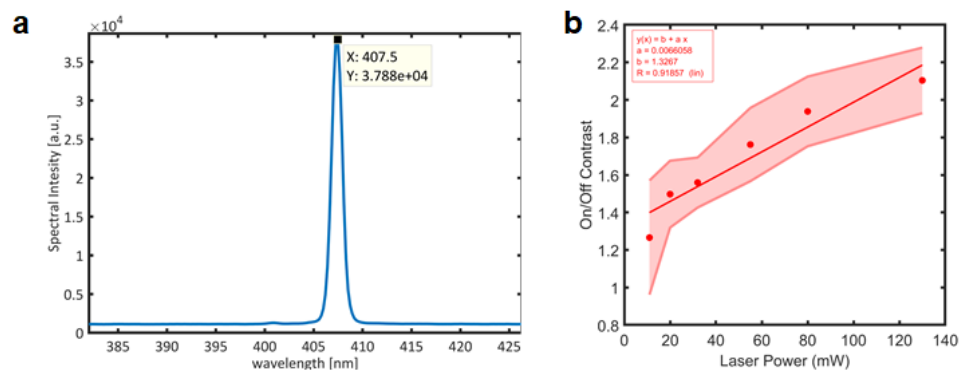
**SI Figure 5.1: Nanowires are oxidized in air and chemically reduced nanowires do not show significant photoconductivity.**

**a**, The UV-Vis of nanowire solutions after normal preparation and with a molar excess of potassium ferricyanide. Current-voltage curves showing very low (12%) change in conductance (G) for chemically reduced nanowires.

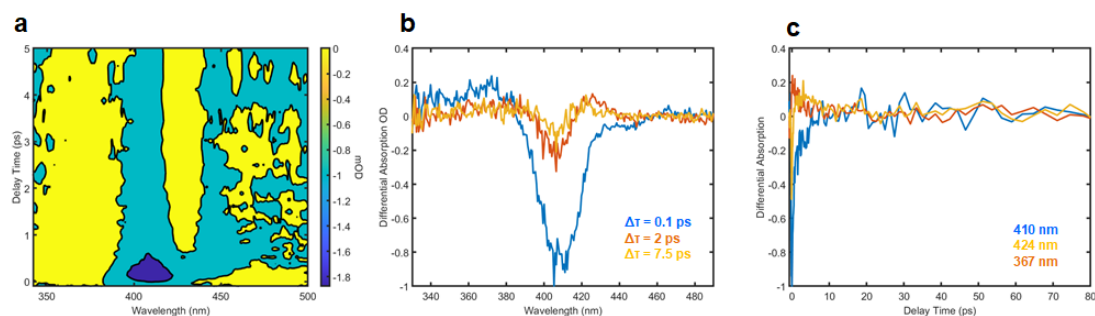


**SI Figure 5.2: Nanowires show photoconductivity irrespective of electrode materials.**

Upon photoexcitation, nanowire conductance increased 110% on tungsten electrodes with 10  $\mu\text{m}$  spacing (blue) and 230% on gold electrodes with 5  $\mu\text{m}$  spacing (yellow).

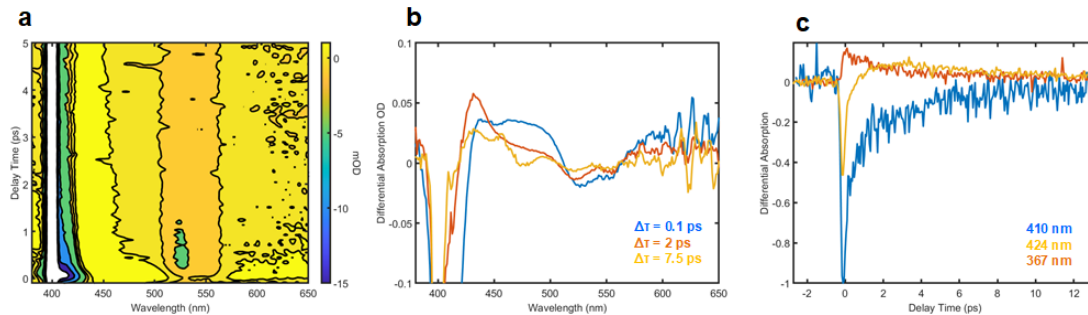


**SI Figure 5.3: Nanowire conductance increase upon laser on/off increases with laser power.** a, Laser characterization for network measurements. b, Ratio of current for nanowires with laser on and laser off under 200 mV bias with a linear fit shown by a solid line. Values represent mean  $\pm$  S.D. (shaded region) for three independent samples.



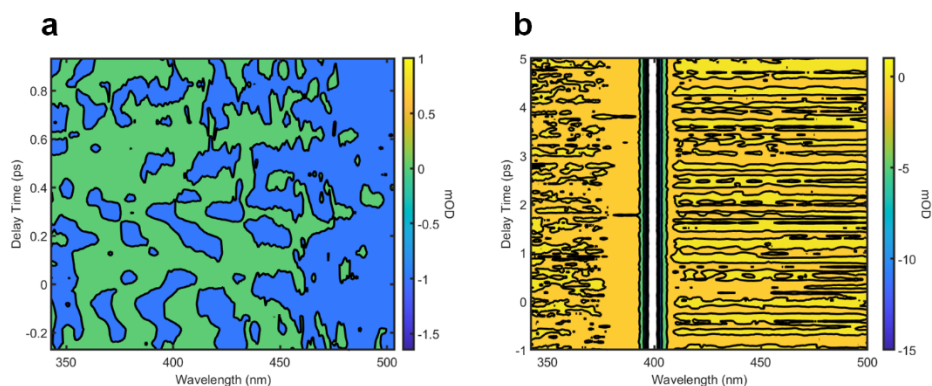
**SI Figure 5.4: Ultrafast (<100 fs) charge transfer between hemes in nanowires revealed by fs-TA with a pump beam at  $\lambda=530$  nm.**

a, 2-D map of differential absorption over the probed wavelengths and delay time. b, Change in differential absorption over wavelength at different delay times as stated in legend. c, Change in differential absorption over delay time at key wavelengths.



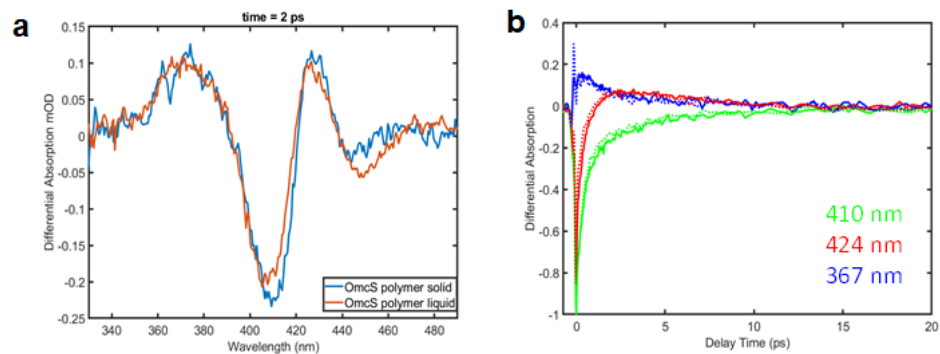
**SI Figure 5.5: Ultrafast (<100 fs) charge transfer between hemes in nanowires revealed by fs-TA with a pump beam ( $\lambda=400$  nm).**

**a**, 2-D map of differential absorption over the probed wavelengths and delay time. **b**, Change in differential absorption over wavelength at different delay times as stated in legend. **c**, Change in differential absorption over delay time at key wavelengths.



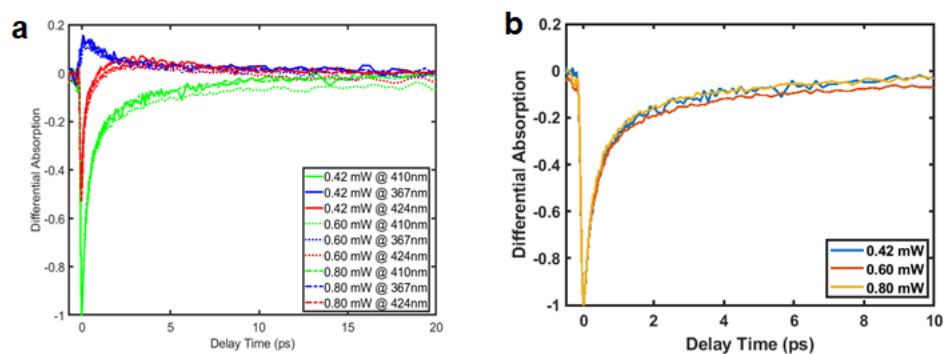
**SI Figure 5.6: Lack of charge transfer without nanowires.**

**a**, 2-D map of differential absorption over the probed wavelengths and delay time shows lack of charge transfer in the substrate alone without nanowires and **b**, lack of charge transfer in the buffer alone without nanowires.



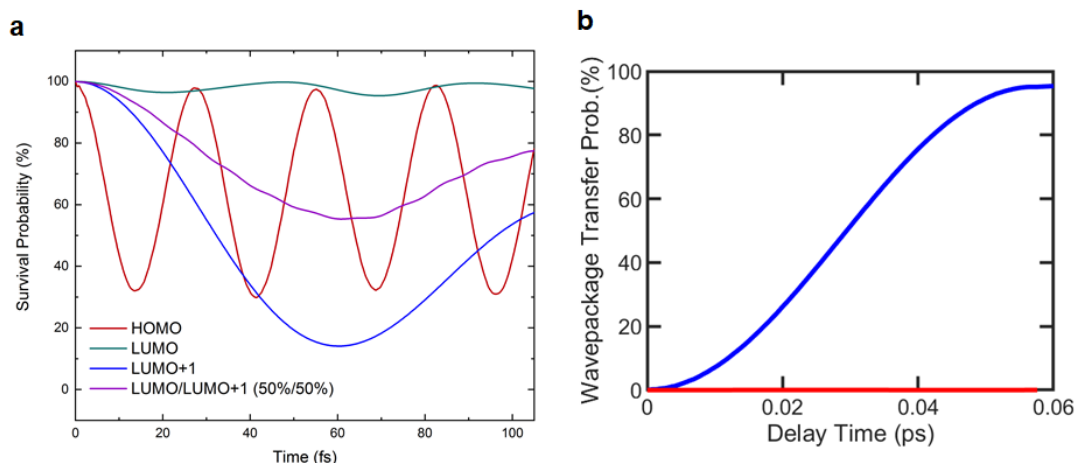
**SI Figure 5.7: Solid state and liquid measurements give similar dynamics.**

**a**, Change in differential absorption over wavelength 2 ps after photoexcitation. **b**, Change in differential absorption over delay time at key wavelengths; solid line shows solid state and dashed lines are liquid state.



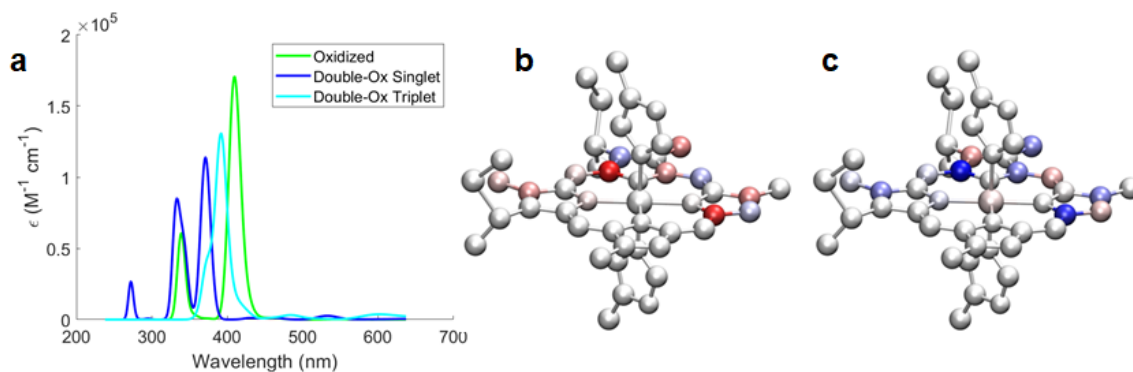
**SI Figure 5.8: Transient absorption dynamics not dependent on laser power.**

**a**, Normalized change in differential absorption over delay time at key wavelengths. **b**, Normalized dynamics in at indicated powers for 410 nm wavelength.



**SI Figure 5.9: Electron survival probability.**

**a**, Survival probability of an electron starting in each initial state on a slip stacked pair of hemes. Sub picosecond transfer is likely (>40%) for all states except LUMO. **b**, Wavefunction transfer probability for parallel-stacked (blue) vs. perpendicular stacked hemes (red)



**SI Figure 5.10: Atomic spin populations for doubly oxidized species.**

**a**, Simulated UV-Vis spectra for doubly oxidized species in singlet and triplet state compared to the ground state. Representation of the change in Mulliken atomic spin populations upon conversion of the singly oxidized heme in the doublet spin state into either the open-shell singlet (**b**) or triplet (**c**) doubly oxidized species. Coloration from blue to red indicate positive to negative changes in spin populations along a symmetric color range between  $\pm 0.13$ . Note that there is hardly any change in the spin population on the Fe center as a result of the second oxidation.

SI Table 5.7.1: Spin Densities

Summary of Mulliken atomic spin densities upon second oxidation of the heme cofactor

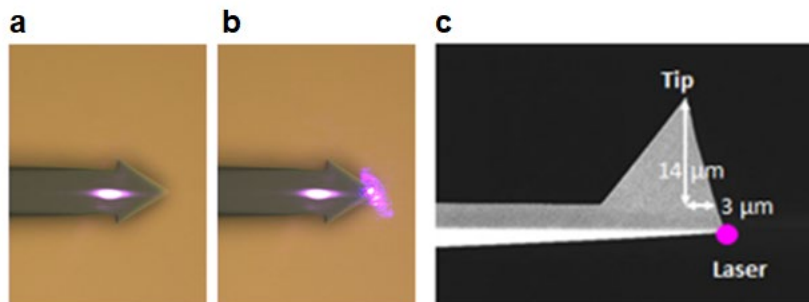
|                      | Singly Oxidized<br>(Doublet) | Doubly Oxidized<br>(Open Singlet) | Doubly Oxidized<br>(Triplet) |
|----------------------|------------------------------|-----------------------------------|------------------------------|
| Fe                   | 1.038                        | 1.037                             | 1.022                        |
| Ligands <sup>a</sup> | -0.039                       | -1.036                            | 0.980                        |
| Total                | 1.000                        | 0.001                             | 2.002                        |

<sup>a</sup>The ligands to the Fe center include the tetrapyrrolic macrocycle with all substituents (except the propionic acid groups) and 4-methylimidazole axial ligands

**SI Table 5.7.2: cp-AFM Nanowire Conductance Values.**

The number of conductance values used to calculate the average conductance of each nanowire with the laser ON and the laser OFF under cp-AFM.

| NW | N used to calc.<br>AVG. |     | NW | N used to calc.<br>AVG. |     |
|----|-------------------------|-----|----|-------------------------|-----|
|    | ON                      | OFF |    | ON                      | OFF |
| 1  | 40                      | 10  | 9  | 10                      | 30  |
| 2  | 80                      | 40  | 10 | 10                      | 10  |
| 3  | 100                     | 20  | 11 | 10                      | 10  |
| 4  | 20                      | 40  | 12 | 120                     | 70  |
| 5  | 40                      | 60  | 13 | 20                      | 120 |
| 6  | 40                      | 20  | 14 | 20                      | 40  |
| 7  | 80                      | 80  | 15 | 20                      | 40  |
| 8  | 20                      | 40  |    |                         |     |



**SI Figure 5.11: Laser alignment for Pc-AFM.**

**a**, No blue laser applied. **b**, Blue laser aligned to cantilever. **c**, Schematic showing the laser aligned to the cantilever (purple dot) and the angle between the laser alignment and tip. The laser power that reaches nanowires will differ from the applied power.

### *Energetic Considerations*

We used the Rehm-Weller cycle to determine whether the radicals are thermodynamically favorable. Unfortunately, we did not find any electrochemical energies reported on identical hemes. We turned to work that looked at different heme-porphyrin salts and the redox energies involved in radical formation<sup>174</sup>. Based on the energetically least favorable transformation ( $\sim 1.7$  V), the previously published redox potential of OmcS ( $-212$  mV)<sup>100</sup>, and the photon energy ( $545\text{nm} = 2.3$  eV) we calculated an energy of  $\Delta G_{\text{et}} = 1.7\text{eV} - (-0.212\text{ eV}) - 2.3\text{ eV} + \omega_{\text{p}} \approx -0.4\text{ eV} + \omega_{\text{p}}$ . The above values correspond to the highest energy barriers reported in the cited paper, and even with these worst-case-assumptions electron transfer still has a driving force of  $-0.4$  eV. Whether  $\text{Fe}^{4+}$  or  $\text{Fe}^{3+}$  porphyrin radicals are formed cannot be determined from this energetical considerations.

## 6. Conclusions and Future Directions

In this thesis I showed that long range electron transport over micrometers can be accomplished given the right arrangement and stability of electron donor and acceptor molecules including proton acceptors as necessary. I also showed that both OmcS and OmcZ nanowires have broad redox potential windows that may allow them to interact with periplasmic cytochromes. OmcS has a more uniform heme environment than OmcZ shown by its single redox peak compared to the tri-centered behavior of OmcZ. This multipeak behavior is mimicked by biofilms that overexpress OmcZ nanowires, lack OmcS, and produce metabolic current equally well as wild type. Thus, I showed that OmcZ can completely account for biofilm conductance and metabolic current in the absence of OmcS nanowires. Finally, I show how cytochrome nanowire OmcS acts as an intrinsic photoconductor to biofilms because it exhibits photoconductivity when the hemes are excited due to ultrafast heme-to-heme electron transfer. This finding explains why OmcS can improve catalytic performance in bacteria that undergo photosynthesis.

Both OmcS and OmcZ nanowire networks show hallmarks of redox conductors, as shown in Chapter 4, therefore determining the exact potential landscape of their heme cofactors is critical to understanding and tuning nanowire functions<sup>111</sup>. OmcZ is a more recently discovered nanowire with structural details just now available. Its higher conductivity and seemingly evolved role to operate in conductive networks gives it high potential for use as an electronic biomaterial<sup>19, 22</sup>. Studies to perform spectroelectrochemistry on OmcZ nanowires are ongoing but its sensitivity to ionic strength is a challenge for solution-state electrochemical experiments<sup>22</sup>. Calculations of the redox landscape as was done for OmcS are underway to help determine external

factors that control individual heme potentials such as heme distortion and surrounding electrostatics.

OmcZ is essential to high current production in biofilms and therefore enhancement of OmcZ conductivity could improve metabolic current output of biofilms which can lead to better catalytic performance<sup>156</sup>. Thus, conductivity and optical studies on OmcZ nanowires and biofilms that overproduce OmcZ could yield significant improvement over the effects shown for OmcS (Chapter 5) and have implications for a wide range of bioelectrochemical systems<sup>28</sup>.

Understanding electron transport in nanowires and biofilms is critical to creating new classes of biomaterials that can interface with electronics from sustainable sources at a low cost. A major barrier that remains to utilizing nanowires at a large scale is isolation of enough purified nanowires to perform bulk spectroscopic measurements. With the continuous discoveries of new extracellular filaments that co-purify, detailed purification protocols for each separate nanowire must be developed<sup>18-22</sup>. Alternatively, production of cytochrome nanowires from *E.coli*, as has been done for various periplasmic cytochromes<sup>108</sup>, would be a better way to scale up nanowire protein production because of the ease of growing *E. coli* over *Geobacter*. Expressing nanowires in *E. coli* could also help ease the incorporation of isotopic elements necessary for determining heme signatures in NMR, and thus determining the exact redox landscape inclusive of proton-coupled electron transfer effects<sup>108</sup>. Scaling up protein production would help to probe additional nanowire modifications such as removing or replacing heme metals.

## References

1. Migliore, A., Polizzi, N.F., Therien, M.J. and Beratan, D.N. Biochemistry and Theory of Proton-Coupled Electron Transfer. *Chemical Reviews* **114**, 3381-3465 (2014).
2. Ron, I., Pecht, I., Sheves, M. and Cahen, D. Proteins as Solid-State Electronic Conductors. *Accounts of Chemical Research* **43**, 945-953 (2010).
3. Ing, N.L., El-Naggar, M.Y. and Hochbaum, A.I. Going the Distance: Long-Range Conductivity in Protein and Peptide Bioelectronic Materials. *The Journal of Physical Chemistry B* **122**, 10403-10423 (2018).
4. Bostick, C.D., Mukhopadhyay, S., Pecht, I., Sheves, M., Cahen, D. and Lederman, D. Protein bioelectronics: a review of what we do and do not know. *Reports on Progress in Physics* **81**, 026601 (2018).
5. Kjeldsen, K.U., Schreiber, L., Thorup, C.A., Boesen, T., Bjerg, J.T., Yang, T., Dueholm, M.S., Larsen, S., Risgaard-Petersen, N. and Nierychlo, M. On the evolution and physiology of cable bacteria. *Proceedings of the National Academy of Sciences* **116**, 19116-19125 (2019).
6. Levar, C.E., Rollefson, J.B. and Bond, D.R. Energetic and Molecular Constraints on the Mechanism of Environmental Fe(III) Reduction by Geobacter in *Microbial Metal Respiration: From Geochemistry to Potential Applications*, 29-48. Springer Berlin Heidelberg (2012).
7. Lovley, D.R. Dissimilatory Fe(III) and Mn(IV) reduction. *Microbiol Rev* **55**, 259-87 (1991).
8. Holmes, D.E., Finneran, K.T., O'Neil, R.A. and Lovley, D.R. Enrichment of members of the family Geobacteraceae associated with stimulation of dissimilatory metal reduction in uranium-contaminated aquifer sediments. *Appl Environ Microbiol* **68**, 2300-6 (2002).
9. Lovley, D.R., Ueki, T., Zhang, T., Malvankar, N.S., Shrestha, P.M., Flanagan, K.A., Aklujkar, M., Butler, J.E., Giloteaux, L., Rotaru, A.-E., Holmes, D.E., Franks, A.E., Orellana, R., Risso, C. and Nevin, K.P. Geobacter: The Microbe

Electric's Physiology, Ecology, and Practical Applications in *Advances in Microbial Physiology*, 1-100. Academic Press (2011).

10. Childers, S.E., Ciuffo, S. and Lovley, D.R. *Geobacter metallireducens* accesses insoluble Fe(III) oxide by chemotaxis. *Nature* **416**, 767-769 (2002).
11. Methé, B.A., Nelson, K.E., Eisen, J.A., Paulsen, I.T., Nelson, W., Heidelberg, J.F., Wu, D., Wu, M., Ward, N., Beanan, M.J., Dodson, R.J., Madupu, R., Brinkac, L.M., Daugherty, S.C., DeBoy, R.T., Durkin, A.S., Gwinn, M., Kolonay, J.F., Sullivan, S.A., Haft, D.H., Selengut, J., Davidsen, T.M., Zafar, N., White, O., Tran, B., Romero, C., Forberger, H.A., Weidman, J., Khouri, H., Feldblyum, T.V., Utterback, T.R., Van Aken, S.E., Lovley, D.R. and Fraser, C.M. Genome of *Geobacter sulfurreducens*: Metal Reduction in Subsurface Environments. *Science* **302**, 1967-1969 (2003).
12. Coppi, M.V., Leang, C., Sandler, S.J. and Lovley, D.R. Development of a genetic system for *Geobacter sulfurreducens*. *Applied and Environmental Microbiology* **67**, 3180-3187 (2001).
13. Caccavo, F., Jr., Lonergan, D.J., Lovley, D.R., Davis, M., Stolz, J.F. and McInerney, M.J. *Geobacter sulfurreducens* sp. nov., a hydrogen- and acetate-oxidizing dissimilatory metal-reducing microorganism. *Appl Environ Microbiol* **60**, 3752-9 (1994).
14. Ueki, T. and Stams Alfons, J.M. Cytochromes in Extracellular Electron Transfer in *Geobacter*. *Applied and Environmental Microbiology* **87**, e03109-20 (2021).
15. Bond, D.R. and Lovley, D.R. Electricity production by *Geobacter sulfurreducens* attached to electrodes. *Appl Environ Microbiol* **69**, 1548-55 (2003).
16. Leang, C., Malvankar, N.S., Franks, A.E., Nevin, K.P. and Lovley, D.R. Engineering *Geobacter sulfurreducens* to produce a highly cohesive conductive matrix with enhanced capacity for current production. *Energy & Environmental Science* **6**, 1901-1908 (2013).
17. Reguera, G., McCarthy, K.D., Mehta, T., Nicoll, J.S., Tuominen, M.T. and Lovley, D.R. Extracellular electron transfer via microbial nanowires. *Nature* **435**, 1098-1101 (2005).

18. Wang, F., Gu, Y., O'Brien J. Patrick, Yi, S.M., Yalcin, S.E., Srikanth Vishok, Shen, C., Vu, D., Ing, N.L., Hochbaum, A.I., Egelman, E. and Malvankar, N. Structure of microbial nanowires reveals stacked hemes that transport electrons over micrometers. *Cell* **177**, 361-369 (2019).
19. Yalcin, S.E., O'Brien, J.P., Gu, Y., Reiss, K., Yi, S.M., Jain, R., Srikanth, V., Dahl, P.J., Huynh, W., Vu, D., Acharya, A., Chaudhuri, S., Varga, T., Batista, V.S. and Malvankar, N.S. Electric field stimulates production of highly conductive microbial OmcZ nanowires. *Nature Chemical Biology* (2020).
20. Gu, Y., Srikanth, V., Salazar-Morales, A.I., Jain, R., O'Brien, J.P., Yi, S.M., Soni, R.K., Samatey, F.A., Yalcin, S.E. and Malvankar, N.S. Structure of *Geobacter* pili reveals secretory rather than nanowire behaviour. *Nature* **597**, 430-434 (2021).
21. Wang, F., Mustafa, K., Suciu, V., Joshi, K., Chan, C.H., Choi, S., Su, Z., Si, D., Hochbaum, A.I., Egelman, E.H. and Bond, D.R. Cryo-EM structure of an extracellular *Geobacter* OmcE cytochrome filament reveals tetrahaem packing. *Nature Microbiology* **7**, 1291-1300 (2022).
22. Gu, Y., Guberman-Pfeffer, M.J., Srikanth, V., Shen, C., Griska, F., Gupta, K., Londer, Y., Samatey, F.A., Batista, V.S. and Malvankar, N.S. Architecture of the *Geobacter* biofilm-associated cytochrome OmcZ nanowires reveals a mechanism for extreme electron conductivity and self-assembly. (*in review*) (2022).
23. Mehta, T., Coppi, M.V., Childers, S.E. and Lovley, D.R. Outer membrane c-type cytochromes required for Fe(III) and Mn(IV) oxide reduction in *Geobacter sulfurreducens*. *Appl Environ Microbiol* **71**, 8634-41 (2005).
24. Nevin, K.P., Kim, B.C., Glaven, R.H., Johnson, J.P., Woodard, T.L., Methé, B.A., DiDonato Jr, R.J., Covalla, S.F., Franks, A.E., Liu, A. and Lovley, D.R. Anode biofilm transcriptomics reveals outer surface components essential for high density current production in *Geobacter sulfurreducens* fuel cells. *PLoS ONE* **4**, e5628 (2009).
25. Eisenberg, D.S. and Sawaya, M.R. Structural Studies of Amyloid Proteins at the Molecular Level. *Annual Review of Biochemistry* **86**, 69-95 (2017).
26. Liu, X., Gao, H., Ward, J.E., Liu, X., Yin, B., Fu, T., Chen, J., Lovley, D.R. and Yao, J. Power generation from ambient humidity using protein nanowires. *Nature* **578**, 550-554 (2020).

27. Sekar, N., Jain, R., Yan, Y. and Ramasamy, R.P. Enhanced photo-bioelectrochemical energy conversion by genetically engineered cyanobacteria. *Biotechnology and Bioengineering* **113**, 675-679 (2016).
28. Bajracharya, S., Sharma, M., Mohanakrishna, G., Dominguez Benneton, X., Strik, D.P.B.T.B., Sarma, P.M. and Pant, D. An overview on emerging bioelectrochemical systems (BESs): Technology for sustainable electricity, waste remediation, resource recovery, chemical production and beyond. *Renewable Energy* **98**, 153-170 (2016).
29. Duraj-Thatte, A.M., Manjula-Basavanna, A., Courchesne, N.-M.D., Cannici, G.I., Sánchez-Ferrer, A., Frank, B.P., van't Hag, L., Cotts, S.K., Fairbrother, D.H., Mezzenga, R. and Joshi, N.S. Water-processable, biodegradable and coatable aquaplastic from engineered biofilms. *Nature Chemical Biology* **17**, 732-738 (2021).
30. Liu, X., Ueki, T., Gao, H., Woodard, T.L., Nevin, K.P., Fu, T., Fu, S., Sun, L., Lovley, D.R. and Yao, J. Microbial biofilms for electricity generation from water evaporation and power to wearables. *Nature Communications* **13**, 4369 (2022).
31. Shipps, C., Kelly, H.R., Dahl, P.J., Yi, S.M., Vu, D., Boyer, D., Glynn, C., Sawaya, M.R., Eisenberg, D., Batista, V.S. and Malvankar, N.S. Intrinsic electronic conductivity of individual atomically resolved amyloid crystals reveals micrometer-long hole hopping via tyrosines. *Proceedings of the National Academy of Sciences* **118**, e2014139118 (2021).
32. Dempsey, J.L. and Hartings, M.R. Hop to It. *Biochemistry* **56**, 5623-5624 (2017).
33. Shih, C., Museth, A.K., Abrahamsson, M., Blanco-Rodriguez, A.M., Di Bilio, A.J., Sudhamsu, J., Crane, B.R., Ronayne, K.L., Towrie, M., Vlček, A., Richards, J.H., Winkler, J.R. and Gray, H.B. Tryptophan-accelerated electron flow through proteins. *Science* **320**, 1760-1762 (2008).
34. Gray, H.B. and Winkler, J.R. Hole hopping through tyrosine/tryptophan chains protects proteins from oxidative damage. *Proceedings of the National Academy of Sciences, USA* **112**, 10920 (2015).
35. Polizzi, N.F., Migliore, A., Therien, M.J. and Beratan, D.N. Defusing redox bombs? *Proceedings of the National Academy of Sciences, USA* **112**, 10821 (2015).

36. Bjerg, J.T., Boschker, H.T., Larsen, S., Berry, D., Schmid, M., Millo, D., Tataru, P., Meysman, F.J., Wagner, M. and Nielsen, L.P. Long-distance electron transport in individual, living cable bacteria. *Proceedings of the National Academy of Sciences* **115**, 5786-5791 (2018).
37. Meysman, F.J., Cornelissen, R., Trashin, S., Bonn , R., Martinez, S.H., van der Veen, J., Blom, C.J., Karman, C., Hou, J.-L. and Eachambadi, R.T. A highly conductive fibre network enables centimetre-scale electron transport in multicellular cable bacteria. *Nature communications* **10**, 1-8 (2019).
38. Malvankar, N.S., Vargas, M., Nevin, K.P., Franks, A.E., Leang, C., Kim, B.-C., Inoue, K., Mester, T., Covalla, S.F., Johnson, J.P., Rotello, V.M., Tuominen, M.T. and Lovley, D.R. Tunable metallic-like conductivity in microbial nanowire networks. *Nature Nanotechnology* **6**, 573 (2011).
39. Ueki, T., Walker, D.J., Woodard, T.L., Nevin, K.P., Nonnenmann, S.S. and Lovley, D.R. An *Escherichia coli* chassis for production of electrically conductive protein nanowires. *ACS Synthetic Biology* **9**, 647-654 (2020).
40. Zhang, Y., Austin, R., Kraeft, J., Cox, E. and Ong, N. Insulating behavior of  $\lambda$ -DNA on the micron scale. *Physical Review Letters* **89**, 198102 (2002).
41. Livshits, G.I., Stern, A., Rotem, D., Borovok, N., Eidelstein, G., Migliore, A., Penzo, E., Wind, S.J., Di Felice, R., Skourtis, S.S., Cuevas, J.C., Gurevich, L., Kotlyar, A.B. and Porath, D. Long-range charge transport in single G-quadruplex DNA molecules. *Nature Nanotechnology* **9**, 1040-1046 (2014).
42. Scheibel, T., Parthasarathy, R., Sawicki, G., Lin, X.-M., Jaeger, H. and Lindquist, S.L. Conducting Nanowires Built by Controlled Self-Assembly of Amyloid Fibers and Selective Metal Deposition. *Proceedings of the National Academy of Sciences, USA* **100**, 4527-4532 (2003).
43. Meier, C., Lifincev, I. and Welland, M.E. Conducting Core–Shell Nanowires by Amyloid Nanofiber Templated Polymerization. *Biomacromolecules* **16**, 558-563 (2015).
44. Bachtold, A., Henny, M., Terrier, C., Strunk, C., Sch nenberger, C., Salvetat, J.-P., Bonard, J.-M. and Forr , L. Contacting carbon nanotubes selectively with low-ohmic contacts for four-probe electric measurements. *Applied Physics Letters* **73**, 274-276 (1998).

45. Millett, F. and Durham, B. Design of Photoactive Ruthenium Complexes To Study Interprotein Electron Transfer. *Biochemistry* **41**, 11315-11324 (2002).
46. Toseland, C.P. Fluorescent labeling and modification of proteins. *Journal of Chemical Biology* **6**, 85-95 (2013).
47. Perron-Savard, P., De Crescenzo, G. and Moual, H. Dimerization and DNA binding of the *Salmonella enterica* PhoP response regulator are phosphorylation independent. *Microbiology* **151**, 3979-87 (2006).
48. Sawaya, M.R., Rodriguez, J., Cascio, D., Collazo, M.J., Shi, D., Reyes, F.E., Hattne, J., Gonen, T. and Eisenberg, D.S. Ab initio structure determination from prion nanocrystals at atomic resolution by MicroED. *Proceedings of the National Academy of Sciences, USA* **113**, 11232 (2016).
49. Sievers, S.A., Karanicolas, J., Chang, H.W., Zhao, A., Jiang, L., Zirafi, O., Stevens, J.T., Münch, J., Baker, D. and Eisenberg, D. Structure-based design of non-natural amino-acid inhibitors of amyloid fibril formation. *Nature* **475**, 96 (2011).
50. Zhang, B., Song, W., Pang, P., Lai, H., Chen, Q., Zhang, P. and Lindsay, S. Role of contacts in long-range protein conductance. *Proceedings of the National Academy of Sciences, USA* **116**, 5886 (2019).
51. Hipps, K.W. It's All About Contacts. *Science* **294**, 536 (2001).
52. Wang, Q., Jones, A.A.D., Gralnick, J.A., Lin, L. and Buie, C.R. Microfluidic dielectrophoresis illuminates the relationship between microbial cell envelope polarizability and electrochemical activity. *Science Advances* **5**, eaat5664 (2019).
53. Zhang, B. and Lindsay, S. Electronic Decay Length in a Protein Molecule. *Nano Letters* **19**, 4017-4022 (2019).
54. Zhang, B., Song, W., Brown, J., Nemanich, R. and Lindsay, S. Electronic conductance resonance in non-redox-active proteins. *Journal of the American Chemical Society* **142**, 6432-6438 (2020).
55. Ho Choi, S., Kim, B. and Frisbie, C.D. Electrical resistance of long conjugated molecular wires. *Science* **320**, 1482-1486 (2008).

56. Amdursky, N., Marchak, D., Sepunaru, L., Pecht, I., Sheves, M. and Cahen, D. Electronic Transport via Proteins. *Advanced Materials* **26**, 7142-7161 (2014).
57. Lindsay, S. Ubiquitous electron transport in non-electron transfer proteins. *Life* **10**, (2020).
58. Fink, H.-W. and Schönenberger, C. Electrical conduction through DNA molecules. *Nature* **398**, 407-410 (1999).
59. Nelson, R., Sawaya, M.R., Balbirnie, M., Madsen, A.Ø., Riek, C., Grothe, R. and Eisenberg, D. Structure of the cross- $\beta$  spine of amyloid-like fibrils. *Nature* **435**, 773-778 (2005).
60. Castillo, J., Tanzi, S., Dimaki, M. and Svendsen, W. Manipulation of self-assembly amyloid peptide nanotubes by dielectrophoresis. *ELECTROPHORESIS* **29**, 5026-5032 (2009).
61. Creasey, R.C.G., Shingaya, Y. and Nakayama, T. Improved electrical conductance through self-assembly of bioinspired peptides into nanoscale fibers. *Materials Chemistry and Physics* **158**, 52-59 (2015).
62. del Mercato, L.L., Pompa, P.P., Maruccio, G., Torre, A.D., Sabella, S., Tamburro, A.M., Cingolani, R. and Rinaldi, R. Charge transport and intrinsic fluorescence in amyloid-like fibrils. *Proceedings of the National Academy of Sciences* **104**, 18019-18024 (2007).
63. Domigan, L.J., Healy, J.P., Meade, S.J., Blaikie, R.J. and Gerrard, J.A. Controlling the dimensions of amyloid fibrils: Toward homogenous components for bionanotechnology. *Biopolymers* **97**, 123-133 (2012).
64. Lee, J., Choe, I.R., Kim, Y.-O., Namgung, S.D., Jin, K., Ahn, H.-Y., Sung, T., Kwon, J.-Y., Lee, Y.-S. and Nam, K.T. Proton Conduction in a Tyrosine-Rich Peptide/Manganese Oxide Hybrid Nanofilm. *Advanced Functional Materials* **27**, 1702185 (2017).
65. Amdursky, N., Głowacki, E.D. and Meredith, P. Macroscale Biomolecular Electronics and Ionics. *Advanced Materials* **31**, 1802221 (2019).

66. Silberbush, O., Amit, M., Roy, S. and Ashkenasy, N. Significant enhancement of proton transport in bioinspired peptide fibrils by single acidic or basic amino acid mutation. *Advanced Functional Materials* **27**, 1604624 (2017).
67. Janiak, C. A critical account on  $\pi$ - $\pi$  stacking in metal complexes with aromatic nitrogen-containing ligands. *Journal of the Chemical Society, Dalton Transactions* 3885-3896 (2000).
68. Ru, X., Zhang, P. and Beratan, D.N. Assessing Possible Mechanisms of Micrometer Scale Electron Transfer in Heme Free *Geobacter Sulfurreducens* Pili. *The Journal of Physical Chemistry B* (2019).
69. Amdursky, N., Ferber, D., Bortolotti, C.A., Dolgikh, D.A., Chertkova, R.V., Pecht, I., Sheves, M. and Cahen, D. Solid-state electron transport via cytochrome *c* depends on electronic coupling to electrodes and across the protein. *Proceedings of the National Academy of Sciences, USA* **111**, 5556 (2014).
70. Amit, M., Yuran, S., Gazit, E., Reches, M. and Ashkenasy, N. Tailor-Made Functional Peptide Self-Assembling Nanostructures. *Advanced Materials* **30**, 1707083 (2018).
71. Hammarström, L. and Styring, S. Proton-coupled electron transfer of tyrosines in Photosystem II and model systems for artificial photosynthesis: the role of a redox-active link between catalyst and photosensitizer. *Energy & Environmental Science* **4**, 2379-2388 (2011).
72. Goyal, P. and Hammes-Schiffer, S. Role of active site conformational changes in photocycle activation of the AppA BLUF photoreceptor. *Proceedings of the National Academy of Sciences, USA* **114**, 1480 (2017).
73. Sayfutyarova, E.R., Goings, J.J. and Hammes-Schiffer, S. Electron-Coupled Double Proton Transfer in the Slr1694 BLUF Photoreceptor: A Multireference Electronic Structure Study. *The Journal of Physical Chemistry B* **123**, 439-447 (2019).
74. Xu, Y., Bao, P., Song, K. and Shi, Q. Theoretical study of proton coupled electron transfer reaction in the light state of the AppA BLUF photoreceptor. *Journal of Computational Chemistry* **40**, 1005-1014 (2019).

75. Lesnichin, S.B., Shenderovich, I.G., Muljati, T., Silverman, D. and Limbach, H.-H. Intrinsic Proton-Donating Power of Zinc-Bound Water in a Carbonic Anhydrase Active Site Model Estimated by NMR. *Journal of the American Chemical Society* **133**, 11331-11338 (2011).
76. Perrin, C.L. and Nielson, J.B. "Strong" hydrogen bonds in chemistry and biology. *Annual Review of Physical Chemistry* **48**, 511-544 (1997).
77. Brennan, B.J., Regan, K.P., Durrell, A.C., Schmuttenmaer, C.A. and Brudvig, G.W. Solvent Dependence of Lateral Charge Transfer in a Porphyrin Monolayer. *ACS Energy Letters* **2**, 168-173 (2017).
78. Yortanlı, M. and Mete, E. Common surface structures of graphene and Au(111): The effect of rotational angle on adsorption and electronic properties. *The Journal of Chemical Physics* **151**, 214701 (2019).
79. Petrov, E.G., Shevchenko, Y.V., Teslenko, V.I. and May, V. Nonadiabatic donor-acceptor electron transfer mediated by a molecular bridge: A unified theoretical description of the superexchange and hopping mechanism. *The Journal of Chemical Physics* **115**, 7107-7122 (2001).
80. Blumberger, J. Recent advances in the theory and molecular simulation of biological electron transfer reactions. *Chemical reviews* **115**, 11191-11238 (2015).
81. Polizzi, N.F., Skourtis, S.S. and Beratan, D.N. Physical constraints on charge transport through bacterial nanowires. *Faraday Discussions* **155**, 43-61 (2012).
82. Nitzan, A. Electron transmission through molecules and molecular interfaces. *Annual Review of Physical Chemistry* **52**, 681-750 (2001).
83. Tezcan, F.A., Crane, B.R., Winkler, J.R. and Gray, H.B. Electron tunneling in protein crystals. *Proceedings of the National Academy of Sciences of the United States of America* **98**, 5002-5006 (2001).
84. Huang, J., Zarzycki, J., Gunner, M.R., Parson, W.W., Kern, J.F., Yano, J., Ducat, D.C. and Kramer, D.M. Mesoscopic to macroscopic electron transfer by hopping in a crystal network of cytochromes. *Journal of the American Chemical Society* **142**, 10459-10467 (2020).

85. Vilan, A. Analyzing Molecular Current-Voltage Characteristics with the Simmons Tunneling Model: Scaling and Linearization. *The Journal of Physical Chemistry C* **111**, 4431-4444 (2007).
86. Kumar, M., Ing, N.L., Narang, V., Wijerathne, N.K., Hochbaum, A.I. and Ulijn, R.V. Amino-acid-encoded biocatalytic self-assembly enables the formation of transient conducting nanostructures. *Nature Chemistry* **10**, 696-703 (2018).
87. Kalyoncu, E., Ahan, R.E., Olmez, T.T. and Safak Seker, U.O. Genetically encoded conductive protein nanofibers secreted by engineered cells. *RSC Advances* **7**, 32543-32551 (2017).
88. Tao, K., Makam, P., Aizen, R. and Gazit, E. Self-assembling peptide semiconductors. *Science* **358**, eaam9756 (2017).
89. Dorval Courchesne, N.-M., DeBenedictis, E.P., Tresback, J., Kim, J.J., Duraj-Thatte, A., Zanuy, D., Keten, S. and Joshi, N.S. Biomimetic engineering of conductive curli protein films. *Nanotechnology* **29**, 454002 (2018).
90. Tsutsui, M., Ohshiro, T., Matsubara, K., Furuhashi, M., Taniguchi, M. and Kawai, T. Atomically controlled fabrications of subnanometer scale electrode gaps. *Journal of Applied Physics* **108**, 064312 (2010).
91. Subramanian, P., Pirbadian, S., El-Naggar, M.Y. and Jensen, G.J. Ultrastructure of *Shewanella oneidensis* MR-1 nanowires revealed by electron cryotomography. *Proceedings of the National Academy of Sciences* **115**, E3246-E3255 (2018).
92. Byun, H.S., Pirbadian, S., Nakano, A., Shi, L. and El-Naggar, M.Y. Kinetic Monte Carlo simulations and molecular conductance measurements of the bacterial decaheme cytochrome MtrF. *ChemElectroChem* **1**, 1932-1939 (2014).
93. Olthuis, W., Streekstra, W. and Bergveld, P. Theoretical and experimental determination of cell constants of planar-interdigitated electrolyte conductivity sensors. *Sensors and Actuators B: Chemical* **24**, 252-256 (1995).
94. Zacharoff, L.A., Morrone, D.J. and Bond, D.R. *Geobacter sulfurreducens* Extracellular Multiheme Cytochrome PgcA Facilitates Respiration to Fe(III) Oxides But Not Electrodes. *Frontiers in Microbiology* **8**, (2017).

95. Leang, C., Coppi, M.V. and Lovley, D.R. OmcB, a c-Type Polyheme Cytochrome, Involved in Fe(III) Reduction in *Geobacter sulfurreducens*. *Journal of Bacteriology* **185**, 2096-2103 (2003).
96. Aklujkar, M., Coppi, M.V., Leang, C., Kim, B.C., Chavan, M.A., Perpetua, L.A., Giloteaux, L., Liu, A. and Holmes, D.E. Proteins involved in electron transfer to Fe(III) and Mn(IV) oxides by *Geobacter sulfurreducens* and *Geobacter uraniireducens*. *Microbiology* **159**, 515-535 (2013).
97. Leang, C., Adams, L.A., Chin, K.J., Nevin, K.P., Methé, B.A., Webster, J., Sharma, M.L. and Lovley, D.R. Adaptation to Disruption of the Electron Transfer Pathway for Fe(III) Reduction in *Geobacter sulfurreducens*. *Journal of Bacteriology* **187**, 5918-5926 (2005).
98. Summers, Z.M., Fogarty, H.E., Leang, C., Franks, A.E., Malvankar, N.S. and Lovley, D.R. Direct Exchange of Electrons Within Aggregates of an Evolved Syntrophic Coculture of Anaerobic Bacteria. *Science* **330**, 1413-1415 (2010).
99. Leang, C., Qian, X., Mester, T. and Lovley, D.R. Alignment of the c-Type Cytochrome OmcS along Pili of *Geobacter sulfurreducens*. *Applied and Environmental Microbiology* **76**, 4080-4084 (2010).
100. Qian, X., Mester, T., Morgado, L., Arakawa, T., Sharma, M.L., Inoue, K., Joseph, C., Salgueiro, C.A., Maroney, M.J. and Lovley, D.R. Biochemical characterization of purified OmcS, a c-type cytochrome required for insoluble Fe (III) reduction in *Geobacter sulfurreducens*. *Biochimica et Biophysica Acta (BBA)-Bioenergetics* **1807**, 404-412 (2011).
101. Liu, Y., Fredrickson, J.K., Zachara, J.M. and Shi, L. Direct involvement of ombB, omaB, and omcB genes in extracellular reduction of Fe(III) by *Geobacter sulfurreducens* PCA. *Frontiers in Microbiology* **6**, (2015).
102. Marques, H.M., Cukrowski, I. and Vashi, P.R. Co-ordination of weak field ligands by N-acetylmicroperoxidase-8 (NAcMP8), a ferric haempeptide from cytochrome c, and the influence of the axial ligand on the reduction potential of complexes of NAcMP8. *Journal of the Chemical Society, Dalton Transactions* 1335-1342 (2000).
103. Battistuzzi, G., Borsari, M., Cowan, J.A., Ranieri, A. and Sola, M. Control of cytochrome c redox potential: axial ligation and protein environment effects. *Journal of the American Chemical Society* **124**, 5315-5324 (2002).

104. Wilson, G.S. Electrochemical studies of porphyrin redox reactions as cytochrome models. *Bioelectrochemistry and Bioenergetics* **1**, 172-179 (1974).
105. Pine Research Honeycomb Spectroelectrochemical Cell User Guide. (2019).
106. Inoue, K., Qian, X., Morgado, L., Kim, B.-C., Mester, T., Izallalen, M., Salgueiro Carlos, A. and Lovley Derek, R. Purification and Characterization of OmcZ, an Outer-Surface, Octaheme c-Type Cytochrome Essential for Optimal Current Production by *Geobacter sulfurreducens*. *Applied and Environmental Microbiology* **76**, 3999-4007 (2010).
107. Bard, A.J. and Faulkner, L.R. *Electrochemical Methods Fundamentals and Applications*. (2001).
108. Dantas, J., Morgado, L., Aklujkar, M., Bruix, M., Londer, Y., Schiffer, M., Pokkuluri, P.R. and Salgueiro, C. Rational engineering of *Geobacter sulfurreducens* electron transfer components: a foundation for building improved *Geobacter*-based bioelectrochemical technologies. *Frontiers in Microbiology* **6**, (2015).
109. Morgado, L. and Salgueiro, C.A. Elucidation of complex respiratory chains: a straightforward strategy to monitor electron transfer between cytochromes. *Metallomics* **14**, mfac012 (2022).
110. Fernandes, T.M., Morgado, L., Turner, D.L. and Salgueiro, C.A. Protein Engineering of Electron Transfer Components from Electroactive *Geobacter* Bacteria. *Antioxidants* **10**, (2021).
111. Dahl, P.J., Yi, S.M., Gu, Y., Acharya, A., Shipps, C., Neu, J., O'Brien, J.P., Morzan, U.N., Chaudhuri, S., Guberman-Pfeffer, M.J., Vu, D., Yalcin, S.E., Batista, V.S. and Malvankar, N. A 300-fold conductivity increase in microbial cytochrome nanowires due to temperature-induced restructuring of hydrogen bonding networks. *Science Advances* **8**, eabm7193 (2022).
112. Shi, L., Fredrickson, J.K. and Zachara, J.M. Genomic analyses of bacterial porin-cytochrome gene clusters. *Frontiers in Microbiology* **5**, (2014).
113. O'Brien, J.P. and Malvankar, N.S. A Simple and Low-Cost Procedure for Growing *Geobacter sulfurreducens* Cell Cultures and Biofilms in

- Bioelectrochemical Systems. *Current protocols in microbiology* **43**, A.4K.1-A.4K.27 (2016).
114. Ma, W., Ying, Y.-L., Qin, L.-X., Gu, Z., Zhou, H., Li, D.-W., Sutherland, T.C., Chen, H.-Y. and Long, Y.-T. Investigating electron-transfer processes using a biomimetic hybrid bilayer membrane system. *Nature Protocols* **8**, 439-450 (2013).
115. Moisy, F. EzyFit (<https://www.mathworks.com/matlabcentral/fileexchange/10176-ezyfit-2-44>). 2.44, (2016).
116. O'Haver, T. peakfit.m (<https://www.mathworks.com/matlabcentral/fileexchange/23611-peakfit-m>). 9.0.0.0, MATLAB Central File Exchange (2018).
117. Ueki, T. Cytochromes in Extracellular Electron Transfer in *Geobacter*. *Applied and Environmental Microbiology* **87**, e03109-20 (2021).
118. Inoue, K., Leang, C., Franks, A.E., Woodard, T.L., Nevin, K.P. and Lovley, D.R. Specific localization of the c-type cytochrome OmcZ at the anode surface in current-producing biofilms of *Geobacter sulfurreducens*. *Environmental Microbiology Reports* **3**, 211-217 (2011).
119. Chadwick, G.L., Jiménez Otero, F., Gralnick, J.A., Bond, D.R. and Orphan, V.J. NanoSIMS imaging reveals metabolic stratification within current-producing biofilms. *Proceedings of the National Academy of Sciences* **116**, 20716-20724 (2019).
120. Wang, Z., Hu, Y., Dong, Y., Shi, L. and Jiang, Y. Enhancing electrical outputs of the fuel cells with *Geobacter sulfurreducens* by overexpressing nanowire proteins. *Microbial Biotechnology* **n/a**, (2022).
121. Ye, Y., Liu, X., Nealon Kenneth, H., Rensing, C., Qin, S. and Zhou, S. Dissecting the Structural and Conductive Functions of Nanowires in *Geobacter sulfurreducens* Electroactive Biofilms. *mBio* **13**, e03822-21 (2022).
122. Richter, H., Nevin, K.P., Jia, H., Lowy, D.A., Lovley, D.R. and Tender, L.M. Cyclic voltammetry of biofilms of wild type and mutant *Geobacter sulfurreducens* on fuel cell anodes indicates possible roles of OmcB, OmcZ, type IV pili, and

- protons in extracellular electron transfer. *Energy & Environmental Science* **2**, 506-516 (2009).
123. Horwich, A.L., Low, K.B., Fenton, W.A., Hirshfield, I.N. and Furtak, K. Folding in vivo of bacterial cytoplasmic proteins: Role of GroEL. *Cell* **74**, 909-917 (1993).
  124. Ing, N.L., Nusca, T.D. and Hochbaum, A.I. Geobacter sulfurreducens pili support ohmic electronic conduction in aqueous solution. *Physical Chemistry Chemical Physics* **19**, 21791-21799 (2017).
  125. Yates, M.D., Golden, J.P., Roy, J., Strycharz-Glaven, S.M., Tsoi, S., Erickson, J.S., El-Naggar, M.Y., Calabrese Barton, S. and Tender, L.M. Thermally activated long range electron transport in living biofilms. *Physical Chemistry Chemical Physics* **17**, 32564-32570 (2015).
  126. Snider, R.M., Strycharz-Glaven, S.M., Tsoi, S.D., Erickson, J.S. and Tender, L.M. Long-range electron transport in <em>Geobacter sulfurreducens</em> biofilms is redox gradient-driven. *Proceedings of the National Academy of Sciences* **109**, 15467 (2012).
  127. Clark, M.M. and Reguera, G. Biology and biotechnology of microbial pilus nanowires. *Journal of Industrial Microbiology & Biotechnology* **47**, 897-907 (2020).
  128. Park, I. and Kim, B.-C. Homologous overexpression of omcZ, a gene for an outer surface c-type cytochrome of Geobacter sulfurreducens by single-step gene replacement. *Biotechnology Letters* **33**, 2043-2048 (2011).
  129. Hernández-Eligio, A., Huerta-Miranda, G.A., Martínez-Bahena, S., Castrejón-López, D., Miranda-Hernández, M. and Juárez, K. GSU1771 regulates extracellular electron transfer and electroactive biofilm formation in Geobacter sulfurreducens: Genetic and electrochemical characterization. *Bioelectrochemistry* **145**, 108101 (2022).
  130. Jiménez Otero, F., Chan Chi, H. and Bond Daniel, R. Identification of Different Putative Outer Membrane Electron Conduits Necessary for Fe(III) Citrate, Fe(III) Oxide, Mn(IV) Oxide, or Electrode Reduction by Geobacter sulfurreducens. *Journal of Bacteriology* **200**, e00347-18 (2018).

131. Stephen, C.S., LaBelle, E.V., Brantley, S.L. and Bond, D.R. Abundance of the Multiheme c-Type Cytochrome OmcB Increases in Outer Biofilm Layers of Electrode-Grown *Geobacter sulfurreducens*. *PLOS ONE* **9**, e104336 (2014).
132. Pettersen, E.F., Goddard, T.D., Huang, C.C., Meng, E.C., Couch, G.S., Croll, T.I., Morris, J.H. and Ferrin, T.E. UCSF ChimeraX: Structure visualization for researchers, educators, and developers. *Protein Sci* **30**, 70-82 (2021).
133. Neu, J., Shipps, C.C., Guberman-Pfeffer, M.J., Shen, C., Srikanth, V., Spies, J.A., Kirchhofer, N.D., Yalcin, S.E., Brudvig, G.W., Batista, V.S. and Malvankar, N.S. Microbial biofilms as living photoconductors due to ultrafast electron transfer in cytochrome OmcS nanowires. *Nature Communications* **13**, 5150 (2022).
134. Cestellos-Blanco, S., Zhang, H., Kim, J.M., Shen, Y.-x. and Yang, P. Photosynthetic semiconductor biohybrids for solar-driven biocatalysis. *Nature Catalysis* **3**, 245-255 (2020).
135. Huang, L., Liu, X., Zhang, Z., Ye, J., Rensing, C., Zhou, S. and Nealon, K.H. Light-driven carbon dioxide reduction to methane by *Methanosarcina barkeri* in an electric syntrophic coculture. *The ISME Journal* (2021).
136. Tokita, Y., Yamada, S., Luo, W., Goto, Y., Bouley-Ford, N., Nakajima, H. and Watanabe, Y. Protein photoconductors and photodiodes. *Angewandte Chemie International Edition* **50**, 11663-11666 (2011).
137. Nam, S., Kim, H., Degenaar, P., Ha, C.-S. and Kim, Y. Extremely slow photocurrent response from hemoprotein films in planar diode geometry. *Applied Physics Letters* **101**, 223701 (2012).
138. Negrerie, M., Cianetti, S., Vos, M.H., Martin, J.-L. and Kruglik, S.G. Ultrafast heme dynamics in ferrous versus ferric cytochrome *c* studied by time-resolved resonance Raman and transient absorption spectroscopy. *The Journal of Physical Chemistry B* **110**, 12766-12781 (2006).
139. Marzolf, D.R., McKenzie, A.M., O'Malley, M.C., Ponomarenko, N.S., Swaim, C.M., Brittain, T.J., Simmons, N.L., Pokkuluri, P.R., Mulfort, K.L., Tiede, D.M. and Kokhan, O. Mimicking natural photosynthesis: Designing ultrafast photosensitized electron transfer into multiheme cytochrome protein nanowires. *Nanomaterials* **10**, 2143 (2020).

140. Yalcin, S.E. and Malvankar, N.S. Seeing is believing: Novel imaging methods help identify structure and function of *Geobacter* nanowires in electricity-producing biofilms in Roadmap on emerging concepts in the physical biology of bacterial biofilms: from surface sensing to community formation *Physical Biology* **18**, 051501 (2021).
141. Malvankar, N.S., Tuominen, M.T. and Lovley, D.R. Biofilm conductivity is a decisive variable for high-current-density microbial fuel cells. *Energy & Environmental Science* **5**, 5790-5797 (2012).
142. Malvankar, N.S., Mester, T., Tuominen, M.T. and Lovley, D.R. From the Cover: Supercapacitors based on *c*-type cytochromes using conductive nanostructured networks of living bacteria. *ChemPhysChem* **13**, 463 - 468 (2012).
143. Yalcin, S.E. and Malvankar, N. The blind men and the filament: Understanding structures and functions of microbial nanowires *Current Opinion in Chemical Biology* **59**, 193-201 (2020).
144. Lovley, D.R., Ueki, T., Zhang, T., Malvankar, N.S. and al., e. *Geobacter: The Microbe Electric's Physiology, Ecology, and Practical Applications*. (2011).
145. Malvankar, N.S., Yalcin, S.E., Tuominen, M.T. and Lovley, D.R. Visualization of charge propagation along individual pili proteins using ambient electrostatic force microscopy. *Nature Nanotechnology* **9**, 1012-7 (2014).
146. Boesen, T., Nielsen, L.P. and Schramm, A. Pili for nanowires. *Nature Microbiology* **6**, 1347-1348 (2021).
147. Malvankar, N.S., Lou, J., Nevin, K., Franks, A.E., Tuominen, M.T. and Lovley, D.R. Electrical conductivity in a mixed-species biofilm. *Applied and Environmental Microbiology* **78**, 5967-5971 (2012).
148. Malvankar, N.S., Lovley, D.R., Beyenal, H. and Babauta, J. Electronic Conductivity in Living Biofilms: Physical Meaning, Mechanisms, and Measurement Methods in *Biofilms in Bioelectrochemical Systems*, 211-248. John Wiley & Sons, Inc (2015).
149. Zhang, B., Cheng, H.-Y. and Wang, A. Extracellular electron transfer through visible light induced excited-state outer membrane C-type cytochromes of *Geobacter sulfurreducens*. *Bioelectrochemistry* **138**, 107683 (2021).

150. Oda, Y., Larimer, F.W., Chain, P.S.G., Malfatti, S., Shin, M.V., Vergez, L.M., Hauser, L., Land, M.L., Braatsch, S., Beatty, J.T., Pelletier, D.A., Schaefer, A.L. and Harwood, C.S. Multiple genome sequences reveal adaptations of a phototrophic bacterium to sediment microenvironments. *Proceedings of the National Academy of Sciences* **105**, 18543-18548 (2008).
151. Melton, E.D., Schmidt, C. and Kappler, A. Microbial iron(II) oxidation in littoral freshwater lake sediment: The potential for competition between phototrophic vs. Nitrate-reducing iron(ii)-oxidizers. *Frontiers in Microbiology* **3**, (2012).
152. Malvankar, N.S., King, G.M. and Lovley, D.R. Centimeter-long electron transport in marine sediments via conductive minerals. *The ISME Journal* **9**, 527-531 (2014).
153. Rosenbaum, M., He, Z. and Angenent, L.T. Light energy to bioelectricity: photosynthetic microbial fuel cells. *Current Opinion in Biotechnology* **21**, 259-264 (2010).
154. Li, D.-B., Cheng, Y.-Y., Li, L.-L., Li, W.-W., Huang, Y.-X., Pei, D.-N., Tong, Z.-H., Mu, Y. and Yu, H.-Q. Light-driven microbial dissimilatory electron transfer to hematite. *Physical Chemistry Chemical Physics* **16**, 23003-23011 (2014).
155. Dong, F., Lee, Y.S., Gaffney, E.M., Liou, W. and Minteer, S.D. Engineering cyanobacterium with transmembrane electron transfer ability for bioelectrochemical nitrogen fixation. *ACS Catalysis* **11**, 13169-13179 (2021).
156. Meng, H., Zhang, W., Zhu, H., Yang, F., Zhang, Y., Zhou, J. and Li, Y. Over-expression of an electron transport protein OmcS provides sufficient NADH for d-lactate production in cyanobacterium. *Biotechnology for Biofuels* **14**, 109 (2021).
157. Shrestha, P.M., Rotaru, A.-E., Aklujkar, M., Liu, F., Shrestha, M., Summers, Z.M., Malvankar, N., Flores, D.C. and Lovley, D.R. Syntrophic growth with direct interspecies electron transfer as the primary mechanism for energy exchange. *Environmental Microbiology Reports* **5**, 904-910 (2013).
158. Morita, M., Malvankar, N.S., Franks, A.E., Summers, Z.M., Giloteaux, L., Rotaru, A.E., Rotaru, C. and Lovley, D.R. Potential for direct interspecies electron transfer in methanogenic wastewater digester aggregates. *mBio* **2**, e00159-11 (2011).

159. Shrestha, P.M., Malvankar, N.S., Werner, J.J., Franks, A.E., Elena-Rotaru, A., Shrestha, M., Liu, F., Nevin, K.P., Angenent, L.T. and Lovley, D.R. Correlation between microbial community and granule conductivity in anaerobic bioreactors for brewery wastewater treatment. *Bioresour Technol* **174**, 306-10 (2014).
160. Wagner, M. Microbiology: Conductive consortia. *Nature* **526**, 513-514 (2015).
161. van Wonderen, J.H., Adamczyk, K., Wu, X., Jiang, X., Piper, S.E., Hall, C.R., Edwards, M.J., Clarke, T.A., Zhang, H. and Jeuken, L.J. Nanosecond heme-to-heme electron transfer rates in a multiheme cytochrome nanowire reported by a spectrally unique His/Met-ligated heme. *Proceedings of the National Academy of Sciences* **118**, (2021).
162. Chen, Y., Yi, H.T., Wu, X., Haroldson, R., Gartstein, Y.N., Rodionov, Y.I., Tikhonov, K.S., Zakhidov, A., Zhu, X.Y. and Podzorov, V. Extended carrier lifetimes and diffusion in hybrid perovskites revealed by Hall effect and photoconductivity measurements. *Nature Communications* **7**, 12253 (2016).
163. Wang, F., Mei, J., Wang, Y., Zhang, L., Zhao, H. and Zhao, D. Fast Photoconductive Responses in Organometal Halide Perovskite Photodetectors. *ACS Applied Materials & Interfaces* **8**, 2840-2846 (2016).
164. Schwab, A.D., Smith, D.E., Bond-Watts, B., Johnston, D.E., Hone, J., Johnson, A.T., de Paula, J.C. and Smith, W.F. Photoconductivity of Self-Assembled Porphyrin Nanorods. *Nano Letters* **4**, 1261-1265 (2004).
165. Kamkar, D.A., Wang, M., Wudl, F. and Nguyen, T.-Q. Single nanowire OPV properties of a fullerene-capped P3HT dyad investigated using conductive and photoconductive AFM. *ACS nano* **6**, 1149-1157 (2012).
166. Martin, K.E., Wang, Z., Busani, T., Garcia, R.M., Chen, Z., Jiang, Y., Song, Y., Jacobsen, J.L., Vu, T.T. and Schore, N.E. Donor- acceptor biomorphs from the ionic self-assembly of porphyrins. *Journal of the American Chemical Society* **132**, 8194-8201 (2010).
167. Berera, R., van Grondelle, R. and Kennis, J.T. Ultrafast transient absorption spectroscopy: principles and application to photosynthetic systems. *Photosynthesis research* **101**, 105-118 (2009).

168. Gu, Y., Li, P., Sage, J.T. and Champion, P.M. Photoreduction of heme proteins: spectroscopic studies and cross-section measurements. *Journal of the American Chemical Society* **115**, 4993-5004 (1993).
169. Vorkink, W. and Cusanovich, M. Photoreduction of horse heart cytochrome c. *Photochemistry and photobiology* **19**, 205-215 (1974).
170. Rego, L.G. and Batista, V.S. Quantum dynamics simulations of interfacial electron transfer in sensitized TiO<sub>2</sub> semiconductors. *Journal of the American Chemical Society* **125**, 7989-7997 (2003).
171. Zerner, M., Gouterman, M. and Kobayashi, H. Porphyrins. *Theoretica chimica acta* **6**, 363-400 (1966).
172. Immeln, D., Weigel, A., Kottke, T. and Perez Lustres, J.L. Primary events in the blue light sensor plant cryptochrome: intraprotein electron and proton transfer revealed by femtosecond spectroscopy. *Journal of the American Chemical Society* **134**, 12536-12546 (2012).
173. Müller, P., Ignatz, E., Kiontke, S., Brettel, K. and Essen, L.-O. Sub-nanosecond tryptophan radical deprotonation mediated by a protein-bound water cluster in class II DNA photolyases. *Chemical Science* **9**, 1200-1212 (2018).
174. Lee, W.A., Calderwood, T.S. and Bruice, T.C. Stabilization of higher-valent states of iron porphyrin by hydroxide and methoxide ligands: electrochemical generation of iron(IV)-oxo porphyrins. *Proceedings of the National Academy of Sciences* **82**, 4301-4305 (1985).
175. Verma, M., Chaudhry, A.F. and Fahrni, C.J. Predicting the photoinduced electron transfer thermodynamics in polyfluorinated 1, 3, 5-triarylpyrazolines based on multiple linear free energy relationships. *Organic & biomolecular chemistry* **7**, 1536-1546 (2009).
176. Guberman-Pfeffer, M.J. and Malvankar, N.S. Making protons tag along with electrons. *Biochemical Journal* **478**, 4093-4097 (2021).
177. Zhong, Y., Wang, J. and Tian, Y. Binary ionic porphyrin self-assembly: Structures, and electronic and light-harvesting properties. *Mrs Bulletin* **44**, 183-188 (2019).

178. Onoda, A., Kakikura, Y., Uematsu, T., Kuwabata, S. and Hayashi, T. Photocurrent Generation from Hierarchical Zinc-Substituted Hemoprotein Assemblies Immobilized on a Gold Electrode. *Angewandte Chemie* **124**, 2682-2685 (2012).
179. Nakamaru, S., Scholz, F., Ford, W.E., Goto, Y. and von Wrochem, F. Photoswitchable Sn-Cyt c Solid-State Devices. *Advanced Materials* **29**, 1605924 (2017).
180. Shapiro, D., Mandava, G., Yalcin, S.E., Dahl, P.J., Shipps, C., Gu, Y., Vishok, S., Salazar-Morales, A.I., O'Brien, J.P., Vanderschuren, K., Vu, D., Batista, V.S., Malvankar, N. and Isaacs, F.J. Protein nanowires with tunable functionality and programmable self-assembly using sequence-controlled synthesis. *Nature Communications* **13**, 829 (2021).
181. Hoeh, M.A., Neu, J., Schmitt, K. and Rahm, M. Optical tuning of ultra-thin, silicon-based flexible metamaterial membranes in the terahertz regime. *Optical Materials Express* **5**, 408-415 (2015).
182. Ali, M.E., Sanyal, B. and Oppeneer, P.M. Electronic structure, spin-states, and spin-crossover reaction of heme-related Fe-porphyrins: a theoretical perspective. *The Journal of Physical Chemistry B* **116**, 5849-5859 (2012).
183. Stephens, P.J., Devlin, F.J., Chabalowski, C.F. and Frisch, M.J. Ab initio calculation of vibrational absorption and circular dichroism spectra using density functional force fields. *The Journal of physical chemistry* **98**, 11623-11627 (1994).
184. Hay, P.J. and Wadt, W.R. Ab initio effective core potentials for molecular calculations. Potentials for the transition metal atoms Sc to Hg. *The Journal of chemical physics* **82**, 270-283 (1985).
185. Ditchfield, R., Hehre, W.J. and Pople, J.A. Self-consistent molecular-orbital methods. IX. An extended Gaussian-type basis for molecular-orbital studies of organic molecules. *The Journal of Chemical Physics* **54**, 724-728 (1971).
186. Hehre, W.J., Ditchfield, R. and Pople, J.A. Self-consistent molecular orbital methods. XII. Further extensions of Gaussian-type basis sets for use in molecular orbital studies of organic molecules. *The Journal of Chemical Physics* **56**, 2257-2261 (1972).

187. Hariharan, P.C. and Pople, J.A. The influence of polarization functions on molecular orbital hydrogenation energies. *Theoretica chimica acta* **28**, 213-222 (1973).
188. Suo, B., Shen, K., Li, Z. and Liu, W. Performance of TD-DFT for excited states of open-shell transition metal compounds. *The Journal of Physical Chemistry A* **121**, 3929-3942 (2017).